UC Berkeley
UC Berkeley Electronic Theses and Dissertations

Title
Imaging Synaptic Scale Dopamine Disruption in Huntington's Disease Model Mice With Near Infrared Catecholamine Nanosensors

Permalink
https://escholarship.org/uc/item/6nf5s728

Author
Yang, Sarah Jiachi

Publication Date
2022

Peer reviewed|Thesis/dissertation

eScholarship.org Powered by the California Digital Library
University of California

Imaging Synaptic Scale Dopamine Disruption in Huntington's Disease Model Mice With Near-infrared Catecholamine Nanosensors

by

Sarah Jiachi Yang

A dissertation submitted in partial satisfaction of the

requirements for the degree of

Doctor of Philosophy

in

Chemical Engineering

in the

Graduate Division

of the

University of California, Berkeley

Committee in charge:

Professor Markita Landry, Co-Chair
Professor David Schaffer, Co-Chair
Professor Ehud Y. Isacoff

Fall 2022

. Imaging Synaptic Scale Dopamine Disruption in Huntington's Disease Model Mice With Near-infrared Catecholamine Nanosensors

Sarah Jiachi Yang

© Copyright 2022
All rights reserved

Abstract

Imaging Synaptic Scale Dopamine Disruption in Huntington's Disease Model Mice With Near-infrared Catecholamine Nanosensors

by

Sarah Jiachi Yang

Doctor of Philosophy in Chemical Engineering

University of California, Berkeley

Professor Markita P. Landry and Professor David V. Schaffer, Co-Chairs

Dopamine neuromodulation is a critical process that facilitates learning, motivation, and movement. Disruption of these processes has been implicated in several neurological and psychiatric disorders including Huntington's Disease (HD). While many treatments for physical and psychiatric HD symptoms target dopaminergic neuromodulation, the mechanism by which dopaminergic dysfunction occurs during HD is unknown. This is partly due to limited capability to visualize dopamine release at the spatiotemporal resolution of both neuromodulator release (ms) and dopaminergic boutons (µm). We have designed a synthetic, optical probe for catecholamines that utilizes near-infrared (nIR) fluorescent, polymer-functionalized single wall carbon nanotubes to report dopamine dynamics within striatal brain tissue. These nIR catecholamine sensors (nIRCats) show a strong response to dopamine within the near-infrared wavelengths ideal for imaging in optically scattering brain tissue. Furthermore, the chemically synthetic molecular recognition elements of nIRCats allow for expression-free imaging of dopamine in the presence of dopamine receptor pharmacology. These characteristics of nIRCat imaging make it a powerful tool uniquely suited for the study of dopamine release in diseased tissues.

In this dissertation I develop methods to utilize nIRCat imaging for the study of dopamine release within R6/2 Huntington's Disease Model mice (R6/2). Using nIRCat's high spatial resolution, I show that dopamine release in R6/2 HD mice decreases with progressive motor degeneration and that these decreases are primarily driven by a decrease in the number of dopamine hotspots combined with decreased release intensity. I adapt this analytical framework towards elucidating how dopamine release sensitivity to extracellular calcium concentration and D2-autoreceptor modulation is affected over the course of HD. In contrast to findings from spatially diffuse dopamine recordings, nIRCat imaging in *ex vivo* R6/2 HD slices indicates that calcium signaling within dopamine hotspots is altered late in disease and D2-autoreceptor signaling is altered early in disease. Lastly, I utilize nIRCat's ability to track individual dopamine hotspots over repeated stimulations and pharmacological washes to measure the release fidelity of dopamine hotspots in late disease. Compellingly, I demonstrate that antagonism of D2-autoreceptors using Sulpiride and direct blocking of Kv1.2 channels using 4-Aminopyradine (4-AP) increases the fidelity of dopamine hotspot activity in the

striatum of WT slices, but not in the striatum of late HD slices. Altogether, these findings — enabled by nIRCats — provide a deeper look into how dopamine release is disrupted and dysregulated during Huntington's Disease to alter the coverage of dopamine modulation across the dorsal striatum.

Dedicated to my parents who taught me how to
find order in the chaos and meaning in the small things

Acknowledgements

In the Trimetric Classic, Kong Rong is tasked with distributing a box of pears amongst his family. It is one of the few passages of Chinese literature I remember learning as a child, though the lines themselves have been lost in the corners of my memory. As I approach the task of acknowledging all those who have supported me in the completion of this dissertation, I cannot help but think of Kong Rong puzzling over how to begin handing pears to those around him. I am sincerely grateful to each of the individuals named below. It is because of their collective support, care, and efforts that I am where I am today.

I would like to first acknowledge my parents, Lili Kuo PhD and Patrick Yang PhD, who were the first in their families to go to college and braved challenge, unkindness, and freezing Minnesota winters to become the scientists they are today. They taught me to be curious about the world around me and instilled within me the desire to make the scientific world a space that is more welcoming and just. I would also like to acknowledge my sister, Ellen Yang, who grounds me in laughter and joy. Thank you for being the co-historian of my life as we've traveled through childhood, adulthood, and the strange grounds between. I cannot imagine sharing the journey with anyone else. Lastly, I would like to acknowledge my Aunt and Uncle, Yicheng Ho PhD and J.S. Kuo PhD, who invested early in my education in the form of alfredo pasta and summers in upstate New York. This isn't an accounting PhD, but hopefully it is the next best thing.

I want to acknowledge all of the educators who have supported me throughout my academic journey. Thank you Dave and Markita for taking a chance on an excited first-year student and letting me piece together my own "blue sky" research project. This dissertation would not have been possible without your support through its many unexpected and rewarding twists and turns. Thank you to the teachers who believed in me and then taught me to believe in my own potential. I would like to specifically thank Prof. Siri Suh whose class on the sociology of medicine irrevocably changed the way I view the role of scientific research, and my Intro Sociology TA Hester who refused to accept my belief that I could not be both an engineer and sociologist. You are the reasons I believe all disciplinary boundaries can and should be crossed.

Finally, I would like to thank the research communities I have been blessed to find myself a part of. Firstly, the Amgen Scholar's Program, which has been the source of a most beautiful and supportive academic and interpersonal community. Secondly, my undergraduate chemical engineering study group who showed me problem solving is more fun when done in a team and over totchos. Thank you to the undergraduate students who I have had the privilege to mentor, and my undergraduate research trainees Francesca Giordani and Ashvin Irrinki whose hard work made the research in this dissertation possible. Thank you to the custodians and staff of Barker Hall who kept me company and let me into my microscope room the many times I locked myself out after hours. Thank you to David Brown for driving me home after long nights of experiments and bringing me CLIF bars when I stayed late. Thank you to those who have answered my "dumb questions" with interest and excitement. Lastly, thank you to the animals without whom this work would not be possible.

Contents

List of Figures

Chapter 1

Dopamine Modulation in Neuronal Function and Neurodegeneration

1.1 The Role of Neuromodulators in Neuronal Communication

Of the many tissues and organs that make up the human body, perhaps none contributes most profoundly to our experience of life and the world around as as the brain. Composed of nearly 86 billion neurons and weighing approximately 3 lbs, our brains allow us to move through the world, learn new things, and encode memories of our experiences. At the most fundamental level, brain function is achieved through the communication between neurons. Within a single neuron, information is conveyed through electrical signals, produced by the movement of ions across the neuronal membrane. Conversely, information between neurons is conveyed through the release of signaling molecules known as neurotransmitters over a tight region of extracellular space known as the synapse (Fig.1.1a). Binding of neurotransmitters by ion channel receptors on the post-synaptic neuron initiates conformational changes within the channel to allow ion flow. Depending on the neurotransmitter identity, the resulting ion flow may drive the postsynaptic neuron towards depolarization or hyperpolarization. The most common excitatory and inhibitory neurotransmitters in the human body are glutamate and gamma-aminobutryic acid (GABA) respectively.

The extent to which neurotransmitter release is able to depolarize or hyperpolarize a neuron is determined in part by factors such as the number of available ion channel receptors and the amount of neurotransmitter released in response to an action potential. Altogether, these factors tune the strength of a established synaptic connection within the brain. The action of a subset of signaling molecules known as neuromodulators can modulate the strength of synaptic connections through activation of pathways that alter factors such as ion channel expression, production, and activity. In contrast to neurotransmitters, neuromodulators do not signal through ion channels. Rather, they exert their influence through G-protein coupled receptors (GPCRs) that initiate intracellular second messenger cascades (Fig.1.1b). Furthermore, neuromodulators frequently signal outside the context of traditional synapses, diffusing throughout the extracellular space of the brain to modulate multiple synpases at once. This difference in signaling results in unique challenges in studying neuromodulator release, which are discussed in Chapter2. Notably, neurotransmitters can also signal through GPCRs, resulting in analagous challenges in the study of neurotransmitter function through these pathways. Of the known neuromodulators, dopamine has been the subject of most extensive study due to its role in shaping synaptic plasticity and implication in learning and movement. In the following sections we provide an overview of how the dopamine signaling within the brain supports communication within the brain during health and the implications of disrupted dopamine signaling during the neurodegeneration.

1.2 Dopaminergic Neuromodulation in the Striatum

Dopamine plays a critical role in healthy brain function by orchestrating complex signaling processes ranging from learning to motor control. Perturbations in dopamine signaling have been implicated in a number of neurodegenerative and psychiatric disorders, including Parkison's disease, Huntington's disease and Schizophrenia[12]. However, despite the central role of dopamine in brain health and disease, the mechanisms by which dopamine and other neuromodulators affect neurochemical brain function and malfunction are not well understood. Dopamine transmission is distinct from classical neurotransmission in its ability to shape the excitability of multiple neighboring neurons by diffusing beyond the synaptic cleft through a process known as volume transmission[13]. Understanding how this spread occurs spatially and temporally requires sensors capable of imaging dopamine at spatiotemporal scales (micrometers and milliseconds) commensurate with dopaminergic modulation. Optical sensors are particularly suited for the study of dopamine release as they provide improved spatial resolution over standard methods using large probes and are able to simultaneously visualize events from a large number of spatial locations[14].

The densest staining for dopaminergic neuron terminals in the striatum, a brain region that has been implicated to play roles in voluntary movement, learning, and motivation. A brief summary of striatal anatomy is provided in Section 1.2.1. Within the striatum, dopamine neurons exhibit two principle patterns of electrical activity: tonic firing and phasic firing. During Tonic firing, dopamine neurons fire regularly spaced spikes at 2–5 Hz. At the density of dopamine axons within the striatum, tonic firing allows the maintenance of a basal dopamine concentration of approximately 10-30 nM[15]. In contrast, phasic firing results from high-frequency bursts of 2-6 action potentials that temporarily increase dopamine release to levels that cannot be quickly cleared by dopamine uptake[13]. This period of heightened dopamine release and overflow into striatal regions surrounding the immediate release site is hypothesized to play a critical role in conveying information about reward to facilitate learning or action selection[16]. As such, understanding the dynamics of dopamine release in the striatum is critical to understanding how neural activity in the striatum gives rise to behavior and how disruption of these dynamics contributes to disease. In the sections below we provide an overview of the role striatal dopamine signaling plays in voluntary movement and action selection. However, we note that the striatum is a functionally heterogenous brain region and striatal dopamine release is well documented to play key roles in encoding reward prediction and facilitation of learning. The close spatial coupling of these functions of movement, reward, and learning suggests that dopamine signaling described here for movement may find applications or play a role in facilitating these neighboring functions.

1.2.1 The Anatomy of the Striatum

The striatum is a large anatomical region located deep within the center of the brain that serves as the principal input module to a group of subcortical nuclei known as the Basal

Ganglia. Traditionally implicated in the processing of voluntary movement, the anatomy and structure of the striatum and basal ganglia have been broadly conserved in vertebrate evolution over the course of 560 million years[17]. The striatum is further divided into three regions, the caudate, putamen, and the ventral striatum. The caudate and putamen are frequently collectively referred to as a dorsal striatum (Fig.1.1c). Information arrives in the striatum in the form of neuronal projections from the cortex, midbrain, and thalamus. Classical models for voluntary movement specifically implicate striatal innervation from excitatory glutamatergic projections from the cortex, excitatory glutamatergic projections from the thalamus, and neuromodulatory action from dopaminergic projects from the substantia nigra pars compacta (Fig.1.1c).

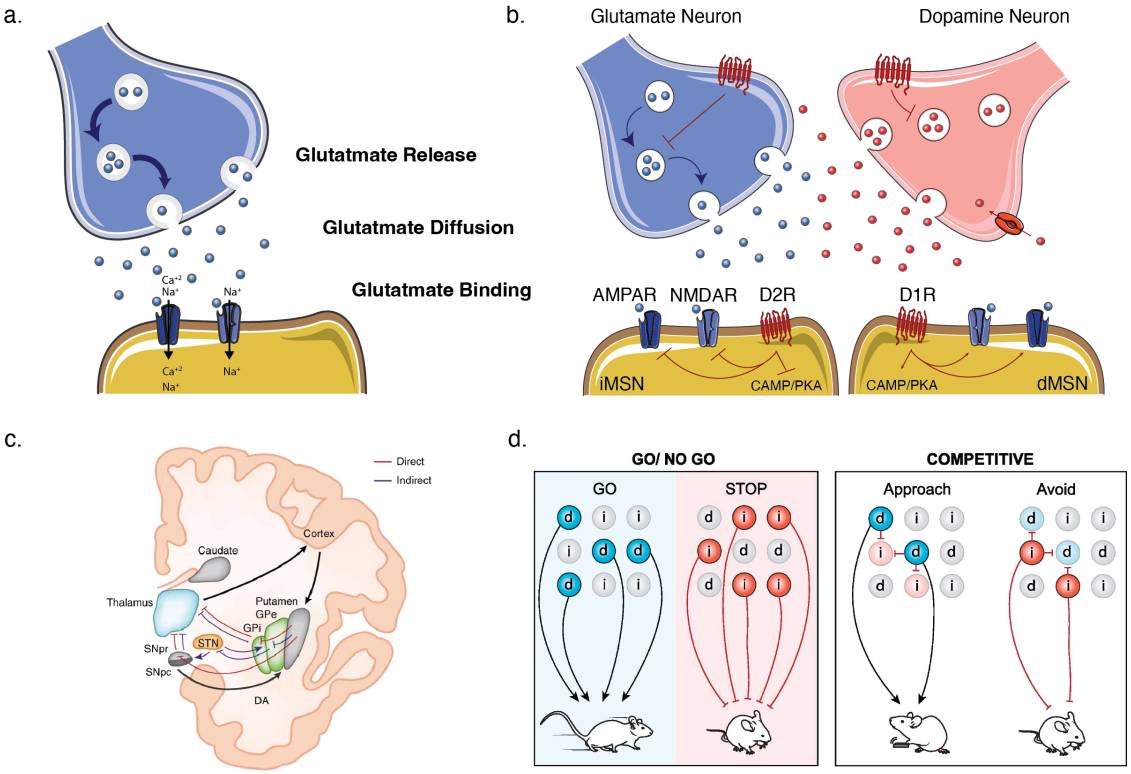

Figure 1.1: Dopamine neuromodulation facilitates striatal signaling for voluntary motion A. Glutamate release from presynaptic neurons (blue) diffuse across the synaptic cleft to bind ion channel receptors located on postsynaptic neurons (yellow). This binding initiates flow of calcium and sodium ions through NMDA receptors and sodium ions through AMPA receptors, depolarizing the postsynaptic neuron. B. Dopamine release binds to D1 receptors on direct pathway MSNs and and D2 receptors on indirect pathways MSNs. Binding of dopamine by these GPCR receptors initiates insertion or removal of NMDAR and AMPAR receptors as well as activation or inhibition of cAMP and PKA pathways. C. Diagram of direct and indirect pathways within the basal ganglia. The red and blue lines represent the direct and indirect pathways within the basal ganglia respectively. (Reproduced with permission from Calabresi et al.[1]). D. Schematic illustrating how dMSNs and iMSNs interact within the go/no go model and competitive model of striatal signaling (reproduced with permission from Bariselli et al.[2]).

Afferent information arriving into the striatum is integrated and processed by the neurons within the striatum and sent to downstream regions of the basal ganglia pathways via efferent projections. The predominant neurons in the striatum are GABAergic medium spiny neurons (MSN), which comprise 90-95% of striatal neurons[18]. Striatal MSNs are further divided into two subpopulations based on their dopamine receptor expression and efferent projection pathway. Direct pathway MSNs express D1 dopamine receptors (D1R) and project to the substantia nigra pars reticulata while indirect pathway MSNs express D2 dopamine receptors (D2R) and project to the external segment of the globus pallidus (Fig.1.1c). Activity of direct and indirect pathway MSNs can be modulated by dopamine release from dopamine axons in the striatum projecting from the substantia nigra pars compacta through mechanisms summarized in Section 1.2.2. In addition to MSNs, the striatum also contains cholinergic interneurons and fast spiking interneurons. Though comparatively small in number relative to MSNs, interneuron activity has been increasingly shown to play a significant role in locally shaping dopamine release and MSN activity[19;20].

Subregions within the striatum have been shown to play different roles in shaping behavioral output, with neuronal activity the Nucleus Accumbens Core (NAc) in the ventral striatum encoding the motivational value of expected goals and neuronal activity in the Dorsal Lateral Striatum (DLS) encoding associations between outcomes, external stimuli, and action[21]. Similarly, neuronal activity in the Dorsal Medial Striatum (DMS) is primarily driven by goal directed behaviors while activity in the Dorsal Lateral Striatum (DLS) is primarily driven by stimulus driven behaviors[22]. Selective lesioning of neurons striatal regions have shown that different regions of the striatum can compensate for regional losses in signaling by using different functional mechanisms of brain signaling to execute the same behaviors[21]. As such, despite their geographic distinctions, striatal subregions likely work cooperatively to shape the behaviors of decision making, action selection, and learning.

1.2.2 The Role of Dopamine in Voluntary Motion

The organization of striatal MSN into two populations expressing different dopamine receptors results in the formation of two neuronal projection pathways that are deferentially modulated by dopamine release. Direct pathway MSNs (dMSNs) and indirect pathway MSNs (iMSNs) express D1R and D2R receptors respectively. Dopamine binding to D1R receptors initiates adenylyl cyclase stimulating G proteins, initiating cellular pathways that drive increase expression and insertion of NMDAR and AMPAR receptors that increase dMSN response to glutamatergic input (Fig.1.1b). Conversely, dopamine binding to D2R receptors inhibit adenylyl cyclase stimulating G proteins, inhibiting cellular pathways and resulting in decreased expression and insertion of NMDAR and AMPAR receptors within iMSNs. As such, dopamine release within the striatum has the ability shift the balance of signaling between direct and indirect pathway neurons.

Signaling through direct and indirect pathway MSNs is classically understood in the context of movement. Initial theories hypothesized that the pathways operated in a "go/no

go" fashion, with high dopamine tone shifting pathway balance to direct pathway neurons that promote movement. The go/no go model of striatal processing also accounts for why dopamine depletion during Parkison's Disease results in bradykinesia and stimulants that induce dopamine release increase movement[2] (Fig.1.1d). Specific activation of iMSNs and dMSNs using optogenetics confirm that artificial activation of these pathways does induce locomotor behavior consistent with expectations from the go/no go model[23]. However, cell specific recordings of dMSNs and iMSNs during natural action selection have complicated this simplicity of this model by showing both dMSNs and iMSNs are both activated during action initiation[24;25]. Striatal action selection may instead occur in a "competitive" fashion, where both iMSNs and dMSNs are activated by a given input and compete to either promote or inhibit movement via the strength of their outputs (Fig.1.1d). In this competitive model, dopamine modulation of dMSN and iMSN firing strength in response to a given input serves as critical method to confer advantage towards either the direct or indirect pathways.

Disruption of striatal signaling has been implicated in Parkison's disease, Huntington's disease and Schizophrenia, diseases that exhibit combinations of motor, behavioral, and cognitive symptoms. In many cases, therapies for the treatment of these disorders target the dopaminergic signaling system. In the following sections we provide an overview of how striatal signaling and dopamine release is disrupted in the neurodegenerative disease Huntington's Disease.

1.3 Degeneration and Dysfunction of Neuronal Signaling During Huntington's Disease

Huntington's Disease (HD) is a rare genetic, neurodegenerative disorder caused by aberrant expansion of the CAG (glutamine) repeat region of the Huntingtin Gene (HTT). It is estimated that there are presently 41,000 symptomatic HD patients living in the United States (HD Society of America). While the prevalence of Huntington's Disease is comparatively rare in Europe and the United States, Huntington's Disease shows increased prevalence within specific countries including Egypt, Norway, Ireland, and Italy[26]. Huntington's Disease is inherited in an autosomal dominant manner, and the children of HD patients have a 50% probability of inheriting the disorder. Patients with HD characteristically present with motor dysfunction as well as cognitive and psychiatric disorders beginning at early adulthood (ages 20-30)[27]. Initial motor dysfunction is characterized by chorea, non-voluntary dance-like movements, and gradually transitions into bradykinesia late in disease. Patients with HD also present with a cognitive symptoms – often detectable up to decade before the onset and diagnosis of motor abnormalities— including changes in concentration, memory, and cognitive flexibility[3;26]. Recently, studies have also indicated that HD may also drive psychiatric changes including increased likelihood for depression, anxiety, and social disinhibition[28].

The Huntington's Disease associated gene Huntingtin (HTT) was the first disease-associated gene to be mapped to a human chromosome[29]. The huntingtin gene contains a polymorphic

CAG region that codes for a polyglutamine (polyQ) stretch that varies from 9 to 37 glutamine repeats in healthy individuals[3]. Natural variance in polyQ length within this range does not result in disease. However, inheritance of a Huntingtin gene with over 37 CAG repeats or aberrant mutation of the CAG region over 37 CAG repeats results in the production of disease causing huntingtin protein, referred to as mutant huntingtin protein[26] (Fig.1.2a). The length of CAG repeat expansion is inversely correlated with age of disease onset, with patients bearing expansions in the range of 40-50 CAG repeats showing early-manifesting juvenile Huntington's Disease that progressed directly to bradykinesia[30]. In the following sections I provide an overview of hypothesized molecular mechanisms for the neurodegenerative action of mutant huntingtin protein as well as an overview on how molecular disturbance gives rise to abnormal synaptic function. I also summarize the growing body of evidence of how aberrant dopamine signaling and modulation in HD may exacerbate these processes and explore how the insights from these studies have informed current treatments for HD and guide the design of novel gene and cell replacement therapies.

1.3.1 Molecular Origins of Huntington's Disease

HD has been traditionally conceptualized as a gain of function disease due to its autosomal dominant inheritance patterns. However, recent research has suggested that the full span of HD related disorders are likely the combined result of deleterious actions from mutant huntingtin protein and loss of normal huntingtin protein function[3;26]. While the presence of mutant huntingtin protein is strongly associated with the development of Huntington's Disease, the precise mechanism of disease action remains poorly understood. This is in part due to huntingtin's multiple HEAT repeat domains which act as a scaffold for protein complexes and are hypothesized to allow huntigntin to adopt multiple protein conformations depending on its intramolecular interactions with a binding target (Fig.1.2b). Studies on purified huntingtin protein using negative stain electron microscopy have observed up to 100 structurally distinguishable protein conformations[31]. Huntingtin can undergo proteolysis at PEST (proline (P), glutamic acid (E), aspartic acid (D), serine (S), and threonine (T)) domains, which in healthy individuals may serve as a control mechanism to inactivate specific functions of huntingtin or achieved developmental apoptosis[3;32].

Huntingtin's flexible protein structure translates into an ability to engage multiple binding partners as a scaffolding protein and contribute to multiple biological pathways. To date, WT huntigntin has been shown to associate with over 350 biding partners with functions ranging from endocytosis, cellular trafficking, protein turnover, and gene transcription[3]. Notable functions huntingtin has been shown to play a role in are regulating the axonal transport of organelles and vesicles from the soma to terminals, scaffolding NMDAR receptors in concert with post synaptic density protein 95 at synaptic terminals, and transcription of brain-derived neurotrophic factor (BDNF) (Fig.1.2b)[33;34;35]. Complete knockout of huntingtin is embryonically lethal and reduced expression of HTT during embryo development result in abnormalities in striatal and cortical formation[30]. In contrast, overexpression of healthy, non-mutant huntingtin protein has been shown to protect neurons from glutamate

excitotoxicity[36;37]. Altogether, these growing insights into the many roles huntingtin plays in healthy neuronal function suggest that loss of healthy huntingtin function may contribute to the physical and cognitive changes observed in HD patients. This loss of function is further exacerbated by new toxic functions exhibited by mutant huntingtin. In particular, patients with HD show increased activity of proteases which act at preoteolytic sites on mutant huntingtin and generate small, n terminal fragments that have been shown to accumulate in nuclei and drive cell death[38]. As a result, HD most likely manifests through a complex combination of mutant huntingtin protein's lost healthy function and gained toxic functions.

Non-mutant huntingtin is water soluble and ubiquitously expressed throughout the brain[26]. However, mutant huntingtin forms large insoluble protein aggregates primarily in striatal medium spiny neurons (MSNs), the principle cell type in the Striatum, and drives their selective and early death during HD[39;40;41]. The mechanism underlying selective MSN degeneration, even while spatially adjacent cholinergic interneurons in the striatum remain unaffected remains an open question in the field. MSNs do not endogenously show increased expression of huntingtin, suggesting that their vulnerability during HD is not simply due to increased levels of mutant huntingtin expression[39;40;41]. Furthermore, though aggregate formation is associated with neuronal degeneration, aggregates may serve as a cell-protection response to deleterious actions by mutant huntingtin rather than disease-causing units[42;43].

The specificity of mutant huntingtin's effect may be partially the result of huntingtin's role in BDNF transcription and transport. BDNF is primarily produced in cortical neurons and is released onto striatal MSNs as a trophic factor. Loss of BDNF trophic support for MSNs due to molecular interference from mutant huntingtin via molecular sequestration into aggregates or decreased binding may drive the specific death of MSNs (Fig.1.2b)[26]. The BDNF hypothesis uncovers a deeper layer of how mutant huntingtin may exacerbate HD disease development by through aberrant synaptic signaling to downstream neurons. Healthy huntingtin protein is known to interact with postsynaptic density protein 95 (PSD95), a critical scaffolding protein for the regulation of NMDA receptors. Increased number of extrasynaptic NMDARs may drive sustained Ca^{+2} influx into MSNs and initiate cell death cascades[44]. Electrophysiological studies have indicated that NMDA receptor dysfunction may drive observed changes in MSN long-term potentiation (LTP) and long-term depression (LTD), processes critical to learning[45;46]. Mutant huntingtin has also been implicated in disrupted presynaptic release, possibly through the presynaptic scaffolding protein Bassoon which also contains an expanted CAG PolyQ region[47]. As such, striatal degeneration and behavioral changes that manifest during HD likely arise through combined cell autonomous effects and synaptic dysfunction[4]. This increasingly complex understanding of HD disease development motivates the expansion of HD research focuses beyond the primary site of neurodegeneration – striatal MSNs – and into adjacent circuitry within the midbrain.

1.3.2 Synaptic disruption in Huntington's Disease

While study of the molecular actions of mutant huntingtin protein provide insights into the origins of Huntington's Disease, understanding how these actions result in synaptic disruption has been pivotal in understanding HD symptomology and disease development. In contrast to other neurodegenerative diseases, HD patients show relatively delayed onset

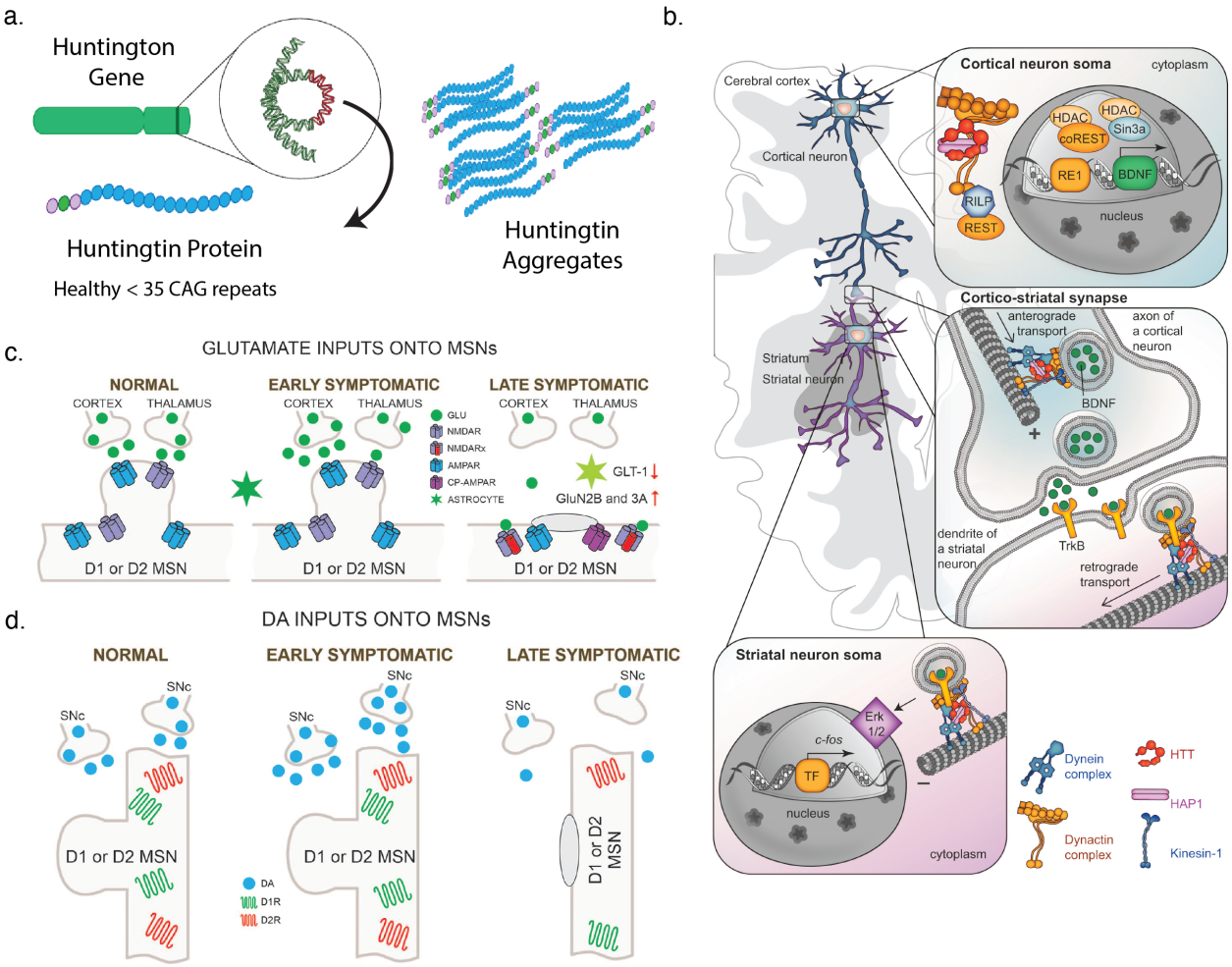

Figure 1.2: Huntington's Disease originates from genetic mutation and manifests through molecular and synaptic dysfunction A. Mutations in the Huntington gene results in expression of mutated huntingtin protein that form large huntingtin aggregates within neurons. B. Schematic overview of the multiple molecular roles of healthy huntingtin protein in scaffolding BDNF transcription, vesicular transport, and signaling within MSNs. (Reproduced with permission from Sandou and Humbert[3]). C. Glutamate release onto MSNs from the cortex and thalamus increases in early symptomatic HD and decreases in late symptomatic HD. These changes in release are accompanied by changes in glutamate receptor expression (Reproduced with permission from Cepeda and Levine[4]). D. Dopamine release onto MSNs from the cortex and thalamus increases in early symptomatic HD and decreases in late symptomatic HD. These changes in release are accompanied by changes in MSN morphology and dopamine receptor expression (Reproduced with permission from Cepeda and Levine[4]).

of characteristic motor symptoms between ages 30-50 despite generating mutant huntingtin protein from embryonic development. This late onset and eventual dysfunction is likely the result of synaptic compensation within the patient brain[48]. In the absence of effective huntingtin lowering therapies, treatment via therapeutics that can intervene at the level of synaptic disruption provides pivotal support to HD patients[49]. Furthermore, widespread delivery of mutant huntingtin lowering therapies to all huntingtin expressing cells within the brain remains technologically infeasible. As such, understanding the key locations of synaptic disruption during disease is pivotal for developing effective delivery strategies for therapeutic constructs in order to reach clinical efficacy.

Exploration of synaptic dysfunction during HD has been largely enabled by the availability of genetic mouse models of HD. Electrophysiology experiments conducted in *ex vivo* brain slices combined with animal behavior studies provide critical insights into how altered signaling between neurons manifests disease. Studies in multiple animal models for HD have implicated aberrant corticostriatal signaling as a driver of MSN degeneration and motor symptomology in HD. (Fig.1.2c)[4]. Cortical projections to the Striatum release excitatory glutamatergic inputs onto MSNs and provide critical trophic support in the form of BDNF. Initial studies in fast-degenerating R6/2 HD model mice have shown that cortical neurons projecting to the striatum show a progressive decrease in excitatory post synaptic potentials (EPSPs) that coincides and becomes more diminished with decreasing motor ability[50]. R6/2 mice were also noted to show an increase in large spontaneous depolarizations from cortical neurons, which correspond to large glutamatergic release events[50]. Studies in slow degenerating YAC128 mice show that EPSPs in YAC128 HD mice are elevated early in disease progression and diminished after onset of decreased motor ability[51]. Measurement of the number of functional corticostriatal afferents in YAC128 mice via FM1-43 dyes suggest that HD YAC128 mice have similar numbers of active glutamatergic terminals to WT mice at 1 month, but show increased average vesicular release compared to WT mice[51]. In contrast, late disease HD YAC128 at 7 months show a decreased number of active glutamatergic terminals, suggesting that cortical signaling to the striatum is decreased late in disease (Fig.1.2c). Interestingly studies that have directly imaged glutamate release into the extracellular striatal space using intensity based glutamate-sensing fluorescent reporter (iGluSnFR) expressed in the MSNs of YAC128 mice show no significant difference in glutamate release or clearance between HD and WT animals[52;53]. As such, full understanding of corticostriatal signaling changes during HD disease progression will likely required integrated insights from multiple presynaptic release and glutamate sensors.

Changes in corticostriatal glutamate release is also shaped by postsynaptic mechanisms. Decreased EPSP size in corticostriatal neurons is paired with observed increased membrane input resistance and capacitance in MSNs, which is postulated to be primarily driven by the loss of dendritic spines and somatic area[50]. Notably, while mutant huntingtin ultimately drives the degeneration of both direct pathway D1 MSNs as well as indirect pathway D2 MSNs, early neurodegeneration has been noted to selectively affect D1 MSNs (Fig.1.2d)[54;55]. This difference is not due to differences in mhtt expression of between direct and indirect MSNs[56]. Given the pivotal role of balanced direct and indirect pathway activation for voluntary movement, the differential degeneration pattern of direct pathway D1 MSNs and indirect

pathway D2 MSNs presents an exciting locus for investigation of the origins of HD associated motor symptoms. However, detailed explorations into this area how been hampered by the quality of current animal models which have been shown to recapitulate the late dyskinetic qualities of HD symptomology, but struggle to capture early choreic events[4]. Nevertheless, animal models can provide mechanistic insights into molecular events that otherwise cannot be studied in detail within human HD patients. Increased D1 MSN excitability driven by the reduction of inwardly rectifying potassium currents has been observed to occur preceding major motor symptoms in multiple genetic murine models[57]. These findings suggest that synaptic dysfunction within HD patients likely begins far before the onset of motor symptoms at 30-40 years of age, and is "held in check" for some period of time via compensatory mechanisms within the brain.

Discoveries in the timing of synaptic dysfunction in HD have motivated explorations of HD brain function preceding symptom development. Recent work has highlighted critical changes in prenatal and perinatal brain development driven by the loss of healthy huntingtin function or the presence of mutant huntingtin[58]. HD murine models show impaired cortical development in the form of neural migration, dendrite maturation, and axon growth early in life far before symptoms manifest[58]. These anatomical changes are influenced and driven by changes in synaptic activity within the HD brain, particularly during developmental "critical periods" when synaptic inputs from the cortex into the Striatum work in tandem to shape the anatomical and electrophysiological characteristics of medium spiny neurons. Work has shown that mutant huntingtin expression in mice decreases the mean frequencies of miniature post synaptic currents (mEPSC) and spontaneous post synaptic currents (sEPSC) during the critical period 1-6 days after they are born when neurons actively migrate to their final locations within the post-natal brain but normalizes to WT levels by 7-10 days after birth[58]. This pattern of early depletion followed by later normalization is observed in the cortical neuron GluA1 AMPA receptor expression and dendritic arbor size of HD neurons. Furthermore, these synaptic and anatomic changes manifest in motor deficits observed in mice as young as 1-3 days after birth[58]. Intriguingly, similar decreases in mEPSC and sEPSC frequency and arbor size were observed in healthy huntingtin depleted mice with the exception that huntingtin depleted mice do not show later recovery after these critical periods[58]. These findings suggest a mediating role for healthy huntingtin protein during HD disease progression and indicate that early changes in HD synaptic activity is characterized by decreased glutamatergic transmission from the cortex to the striatum in the days after mouse birth, leading to decreased dendritic arbors and motor deficits. This is confirmed by findings that show HD mice treated with the positive AMPA modulator CX516 over the course of the first postnatal week show restoration of dendritic arbor sizes and delayed onset of motor symptoms despite the treatment's containment to the one-week critical period. The implications of this early postnatal development research in HD have opened a renewed interest in how altered synaptic activity in the brain outside of glutamate during critical periods of development may give rise to neurodegeneration of compensatory action within the brain. Therapeutically, these findings advocate for the development of therapies that not only seek to lower mutant huntingtin but also directly address synaptic aberrations and are deployed during critical periods of development.

1.3.3 Dopamine disruption in Huntington's Disease

Disruptions in neuromodulator signaling comprise a third dimension of Huntington's Disease related neurodegeneration alongside molecular and synaptic disruptions. Dopamine's role as a major neuromodulator governing movement and learning in the Striatum and implication in other neurodegenerative motor disorders such as Parkinson's Disease has made motivated its close examination as a driver of Huntington's Disease. As noted in Section 1.2 Healthy striatal function relies on dopamine release from neurons projecting from the Substantia Nigra pars compacta (SNc) to shape glutamate release from cortical neurons onto direct and indirect pathway MSNs via dopamine D1 Receptors (D1R) and dopamine D2 Receptors (D2Rs)[2]. Decreases in dopamine tone and release, as in the case of Parkinson's Disease, results in impaired motor function[59]. Bi-phasic changes in dopamine release has been noted in both human HD patients and HD animal models, with elevated dopamine release coinciding with choreic motor phenotypes and decreased dopamine release coinciding with bradykinesia (Fig.1.2d)[60;61;62;63]. A detailed overview of these dopamine studies in murine models of HD and their findings is discussed in Chapter 3. In human HD patients, dopamine disruption plays a principal role in HD pathophysiology. Excess release of dopamine onto MSNs in the striatum is hypothesized to be the primary driver of choreic movements, and treatment for chorea is presently achieved through broad depletion of monoamines–including dopamine–using the drug tetrabenzine (TBZ)[63].

Dopamine's ability to signal in a spatially diffuse manner and shape local neurotransmitter release motivates the study of HD related changes in dopaminergic and glutamatergic signaling in tandem. Studies in HD model mice suggest that early in disease HD animals show similar expression of D-1 receptors on direct-pathway MSNs but a decreased sensitivity to the D1-antagonist SKF81297[64]. This decreased sensitivity can be corrected through administration of tetrabenazine (TBZ) which acts through depleting dopamine stores. These results are observed during concurrent time periods when glutamatergic release from the cortex to the striatum is elevated[64]. However, it remains unclear whether aberrant dopaminergic signaling serves as a driver of altered glutamatergic signaling or as a compensatory mechanism that post-synaptically shapes the excitability of direct and indirect medium spiny neurons in response to glutamate. Dopamine may also play a role in elucidating why D1 MSNs are preferentially affected early Huntington's disease while D2 MSNs appear relatively spared[64]. As disease progresses, dopaminergic neurons may themselves become compromised through cell-autonomous and synaptic mechanisms, resulting in loss of this compensatory force. Clarity in this complex dynamic between dopamine and glutamate during Huntington's Disease requires tools that enable the visualization of both processes simultaneously.

While general trends in dopamine levels have been reported for HD, comparatively little is known about how dopaminergic signaling changes at the level of release sites. Recent findings have shown that some portion of striatal dopamine release arises from defined axonal sites equipped with fast-release synaptic machinery[65;66;67]. Simulations of dopamine release have also shown the importance of dopaminergic coverage across the striatum for effective activation of D1-Receptors (D1R) and D2-Rreceptors (D2R) on MSNs[68;69]. Challenges in measuring dopamine release at this level of spatial resolution has historically been in part

due to lack of tools for high spatio-temporal imaging. We discuss these challenges in detail in Chapter 2. Complete understanding of how dopamine shapes neurodegeneration in Huntington's disease requires an integrated understanding of how the molecular and synaptic drivers of HD impact dopaminergic signaling. This requires the development of new tools capable of examining dopamine across its broad ranges of spatial and temporal action.

1.3.4 Novel therapeutics for Huntington's Disease

Though there is no present cure for HD, treatments aimed towards symptom management primarily target dopaminergic, glutamate or GABA signaling[70]. Patients are commonly prescribed tetrabenazine and deuteetrabenazine to manage choreic symptoms and may receieve L-Dopa treatment during late Parkison-like stages of disease. Pioneering work in mice expressing mutant huntingtin under the control of a Tetracycline promotor showed that removal of mutant huntingtin is sufficient to reduce the number of Hutington's aggregates and reverse motor deficits in mice even after significant disease progression As such, the majority of novel therapies presently in development seek to decrease the amount of mutant huntingtin protein in patients[71;72;73;74]. Therapies are also in development to differentiate medium spiny neurons for transplant into the patient Striatum as a cell replacement therapy[71;72;73;74;75;76;77]. However, to date, these therapeutics have yet to demonstrate efficacy in clinical trials[78;79]. These efforts are largely directed towards the cortex and striatum, areas of noted degeneration in HD but distal to the location of dopaminergic cell bodies in the substantia nigra pars compacta.

Recent work showing that well-timed delivery of small molecule agonists or antagonists during critical periods of development have renewed interest in the critical role of therapeutic delivery timing. Presently, HD patients begin to receive treatment during the onset of motor symptoms. However, new insights into disruptions in brain development during critical periods long before motor symptoms may call for earlier interventions and more precise diagnostic tools to determine appropriate timing of therapy.

Chapter 2

Near-infrared Catecholamine Nanosensors for Non-genetically Encoded, High Spatiotemporal Dopamine Imaging[ii]

[ii]This section is produced in part with permission from the following works: Yang, S. J.*, Del Bonis-O'Donnell, J.T.*, et al. "Near-infrared catecholamine nanosensors for high spatiotemporal dopamine imaging." *Nature Protocols* (2021), 16, 3026–3048.; Beyene, A.G.*, Yang, S.J.*, Landry, M.P., "Tools and Trends for Probing Brain Neurochemistry." *Journal of Vacuum Science and Technology A* (2019), 37(4): 040802.; Yang, D., Yang, S. J., Bonis-O'Donnell, J. T. D., Pinals, R. L., and Landry, M. P. "Mitigation of Carbon Nanotube Neurosensor Induced Transcriptomic and Morphological Changes in Mouse Microglia with Surface Passivation". *ACS Nano*, 14(10), pp 13794–13805 (2020); Yang, S. J.*, Beyene, A.*, and Landry, M. P., "Tools and Trends for Probing Brain Chemistry". *Journal of Vacuum Science and Technology A* 37(4): 040802, (2018)

2.1 Imaging and Sensing the Brain

The human brain contains on the order of 100 billion neurons, a number that rivals the number of stars in the Milky Way. These neurons form on the order of 10^{15} connections called synapses with one another, forming a dense communication network that forms the backbone of human thought and consciousness. Understanding how the brain functions requires both an understanding how each individual neuron connects to the other neurons within the brain (structure and connectivity) as well as an understanding of the strength of each connection (neurotransmission). Recent work has made great strides towards mapping the structure and connectivity of the brain to form a connectome map of the brain. To date, full connectomes have been generated for the *D. melanogaster* (fly) brain and *C. elegans* (worm) brain. These model organisms have relatively low total neuron numbers, enabling connectome mapping using transmission electron microscopy on serial, ultrathin sections of the brain[80]. Present developments in connectome mapping have sought to increase spacial resolution through improved microscopy methods such as focused ion beam scanning electron microscopy (FIB-SEM) or enable faster acquisition of large samples through gas cluster ion beam scanning electron microscopy (GCIB-SEM)[81;82]. Development of a precise connectome for large brains, such as those of rodents or a human will requires development on both these technical fronteirs.

While the mapping of brain connectomes have provided a powerful resource for understanding systems-circuit neuroscience, knowledge of brain structure and connectivity is not sufficient for understanding how the brain operates. As such, techniques aimed at mapping the brain connectome must be complemented by sensing tools capable of reporting on the brain as it functions. In this chapter, I provide a brief review of present techniques available for sensing brain activity and contextualize the development of the near-infrared catecholamine nanosensor (nIRCat) new non-genetically encoded imaging tool for dopamine release.

2.1.1 Recording Electrical Activity in Neurons

Foundational work in giant squid axons established that information is conveyed from one end of a neuron to another through electrical impulses generated by ion movement through sodium and potassium channels[83]. These findings laid the groundwork for the development of electrophysiology, a family of experimental techniques that presently represent the gold-standard for investigating and understanding neuronal signaling. During electrophysiology, electrodes are introduced to neurons to record electrical signals resulting from ion movement across the neuronal membranes Electrophysiology is often conducted in *ex vivo* acute brain slices to allow easy access of neurons. However, *in vivo* electrophysiology is also possible through surgical introduction of electrodes into living animals[84;85;86]. Variations of electrophysiolgy such as patch-clamp physiology or the introduction of channel blockers and toxins allow elucidation of how neuronal electrical activity is shaped by specific channels or ions. These techniques can then be used to investigate how the electrical characteristics of varying

cell types change as animals undergo learning paradigms, experience environmental inputs, or undergo disease states.

The direct physical contact between electrode and neuron required for electrophysiological recording allows for extremely high signal-to-noise recordings of electrical activity[14]. However, this requirement for direct contact results in the need for labor intensive recordings from single cells that make electrophysiology a low-throughput technique. Furthermore, electrophysiology measures electric qualities such as the current or voltage of a neuron and thus is unable to directly assay the release of chemical neurotransmitters and track the flow of information from one neuron to another. This is a notable caveat given studies that suggest only a fraction of action potentials arriving at terminal boutons initiate neurotransmitter release, and the shaping of these release probabilities plays a critical role in encoding the strength of individual synapses[87]. It is possible to track neurotransmitter release by monitoring the electrical activity of the post-synaptic cell while stimulating pre-synaptically. The resulting post synaptic depolarizations currents can be correlated to the binding of released neurotransmitter. However, this method is unable to fully able to track the signaling patterns of molecules where a single release event may result in broad diffusion to multiple post-synaptic targets. Further challenges are faced when trying to study neuromodulators such as dopamine, which signal through G-protein coupled receptors (GPCRs) rather than ion channels, and whose binding does not directly result in a electrical event. This renders dopamine release and signaling invisible to the eye of electrophysiology.

Optical reporters for neuronal electrical activity such as voltage sensitive dyes and genetically encoded voltage indicators have been developed as a method to monitor electrical activity within multiple neurons within the brain without requiring direct contact of physical electrodes[88;89;90;91]. While these methods allow for more powerful exploration of electrical signaling within neurons, they do not address the fundamental barriers in studying chemical signaling between neurons through the lens of electrical signaling. Optical sensors have been developed to visualize processes closer to neurotransmitter release such as calcium influx (calcium dyes, genetically encoded calcium indicators) and pH changes during vesicle fusion (pHluorins)[92;93;94;95]. These techniques have enabled powerful discovery within neuroscience which are elaborated in Chapter 4 . However, these methods remain unable to directly visualize or monitor the release of neurotransmitters or other chemical signaling molecules.

2.1.2 Recording Dopamine Signaling Between Neurons

Neurons communicate through an array of over 100 signaling molecules that include neurotransmitters, neuromodulators, neuropeptides, and hormones. The neurotransmitters glutamate and GABA serve as the brain's primary excitatory and inhibitory molecules, and their release can be studied via a robust toolbox of protein-based sensors. These include the intensity-based glutamate sensing fluorescent reporter (iGluSnFR) and the intensity-based GABA sensing fluorescent reporter (iGABASnFR) which fuse circularly prermuted green fluorescent protein into the glutamate binding periplasmic protein GltI from *E.Coli* and the

GABA binding protein Pf622 from *Pseudomonas fluorescens* respecitvely[96;97]. A comparable toolbox for imaging neuromodulators such as dopamine and serotonin has only recently been formed and remains an active area of development. I provide an overview of the array of dopamine sensing methods currently available for imaging in animal systems below, separating genetically encoded and non-genetically encoded tools.

2.1.3 Genetically Encoded Tools to Study Dopamine Release

One of the first genetically encoded tools for sensing dopamine release was the Dopamine Cell-based neurotransmitter fluorescent engineered reporter (CNiFER)[5]. Rather than building a sensor around a conformation-changing-protein, CNiFERs are clonal HEK293 cells specially engineered to express the dopamine D2 receptor that increases intracellular calcium upon binding (Fig.2.1a). This increase in intracellular Ca2+ is subsequently detected by a genetically encoded FRET Ca2+ sensor TN-XXL which operates via cyan and yellow fluorescent protein fluorophores. CNiFER response tests in vitro indicate that the sensor provides a phasic response within 20-40s of bolus neurotransmitter delivery, followed by a tonic plateau that stabilizes after 300s. The phasic response has been shown to be independent of external calcium concentration, while the tonic response is eliminated in calcium-free media[5]. The effective concentration for 50 response level (EC50) of the phasic response is reported at 2.5 nM for D2-CNiFER. At the time of design, this placed CNiFER's optimal sensor sensitivity within the natural concentration range of dopamine identified via orthogonal methods such as microdialysis and FSCV. Notably, D2-CNiFER shows a 30 fold increase in sensitivity for dopamine over norepinepherine, which historically has shown strong cross-reactivity with dopamine sensors due to the two molecules' structural similarities. The CNiFER system's use of natural receptors allows it to leverage the natural binding and dissociation kinetics of neurotransmitter receptors. However, its temporal resolution is reliant on the activation of the inositol triphosphate (IP3) signaling pathway, resulting in a 2s delay in signal after stimulus delivery[5]. CNiFER cells work robustly *in vivo*, but must be generated externally and stereotaxically implanted into animals. As a result, CNiFER cells do not offer the cell-type selectivity typically associated with a genetically encoded sensors. More profoundly, the large size of CNiFER cells cannot resolve single synapse neurotransmission events and thus is limited to the study of dopamine volume transmission.

Recently, G-Protein Coupled Receptor Based Probes (dLight, GRAB-DA) have been developed for dopamine[98;99]. Similar to the design principles established in iGluSnFR, these GPCR-based dopamine sensors are developed by inserting circularly permutated GFP into the sequences of the D1 or D2 dopamine receptors to allow direct coupling of structural changes incurred by analyte-binding to fluorescence modulation of inserted cGFP (Fig.2.1b). The dLight probe has variants constructed by inserting the cGFP module sequence into the third intracellular loop (IL3) of the human dopamine D1, D2 and D4 receptors. GRABDA is constructed from insertion of cEGFP into the IL3 of the human dopamine D2 receptor. Both platforms offer sensor families with varying binding kinetics to match the biological phenomena to be studied. Similar to iGluSnFR, both dLight and GRABDA trangenes can each be

delivered via AAV for expression in the brain. This allows for cell-type specific expression of these sensors. Both dLight and GRABDA have demonstrated robust performance in *ex vivo* brain slice and *in vivo* within mice, flies, and zebrafish[98;99]. The broad range of application within dopamine release found by dLight and GRAB-DA in the first years following their release has underscored the importance and utility of a temporally an spatially precise dopamine sensing tool. However, open challenges remain within the dopamine sensing field. The genetically encoded nature of dLight and GRAB-DA limits their applications to studies conducted within genetically tractable organisms. This precludes their use in non-model organisms. In addition, dLight and GRAB-DA's utilization of endogenous dopamine receptors makes them optically responsive to a significant proportion of dopamine receptor pharmacology and prone to buffering endogenous dopamine release. As a result, dLight and GRAB-DA cannot readily be used to study the effect of therapeutically-relevant agents on neuronal signaling and brain signaling.

2.1.4 Non-genetically Encoded Tools to Study Dopamine Release

Non-genetically encoded tools for the study of dopamine release laid the groundwork for dopamine research before the development of genetically-encoded dopamine sensors and remain a powerful complements to their genetically-encoded counterparts within the toolbox of dopamine sensors. One of the earliest methods for studying dopamine release was microdialysis, a technique in which samples from the interstitial space of brain tissue are recovered by dialysis and characterized using established analytical approaches such as liquid chromatography, capillary electrophoresis, mass spectrometry and electrochemistry (Fig.2.1c). Microdialysis requires the insertion of a dialysis probe into the brain of the animal of interest. Once inserted, the probe is perfused with a solution (blank perfusate) whose ionic balance resembles that of the extracellular fluid. During this time, neurotransmitters, hormones, and metabolites diffuse along their concentration gradient from the extracellular space into the continuoulsy flowing perfusate. The perfusate can be collected for later analysis or directly fed to a mass spectrometer for real-time analysis of its contents. Due to its utilization of powerful analytical instruments, microdialysis is able to provide highly selective and reliable identification of a wide range of molecules. Indeed, microdialysis is a heavily utilized tool to study molecules with no other sensing systems available. However, despite its versatility, microdialysis also exhibits several drawbacks. Most notably, microdialysis offers poor temporal resolution, with the fastest sample times exceeding one minute. As such, microdialysis is able to capture trends in basal levels of molecule release, but not fast-release events correlating to electrical activity. Furthermore, the spatial resolution of microdialysis is limited by the size of the probe. Most microdialysis probes have lengths on the order of millimeters and widths on the scale of several hundreds of micrometers, affording only sampling of analytes from volumes that span hundreds of micrometers from the probe. The limited spatial information provided by microdialysis and other device-based techniques is a primary disadvantage compared to smaller sensors, such as molecular fluorescent probes, which provide more detailed readouts across space. Recovering samples using dialysis from

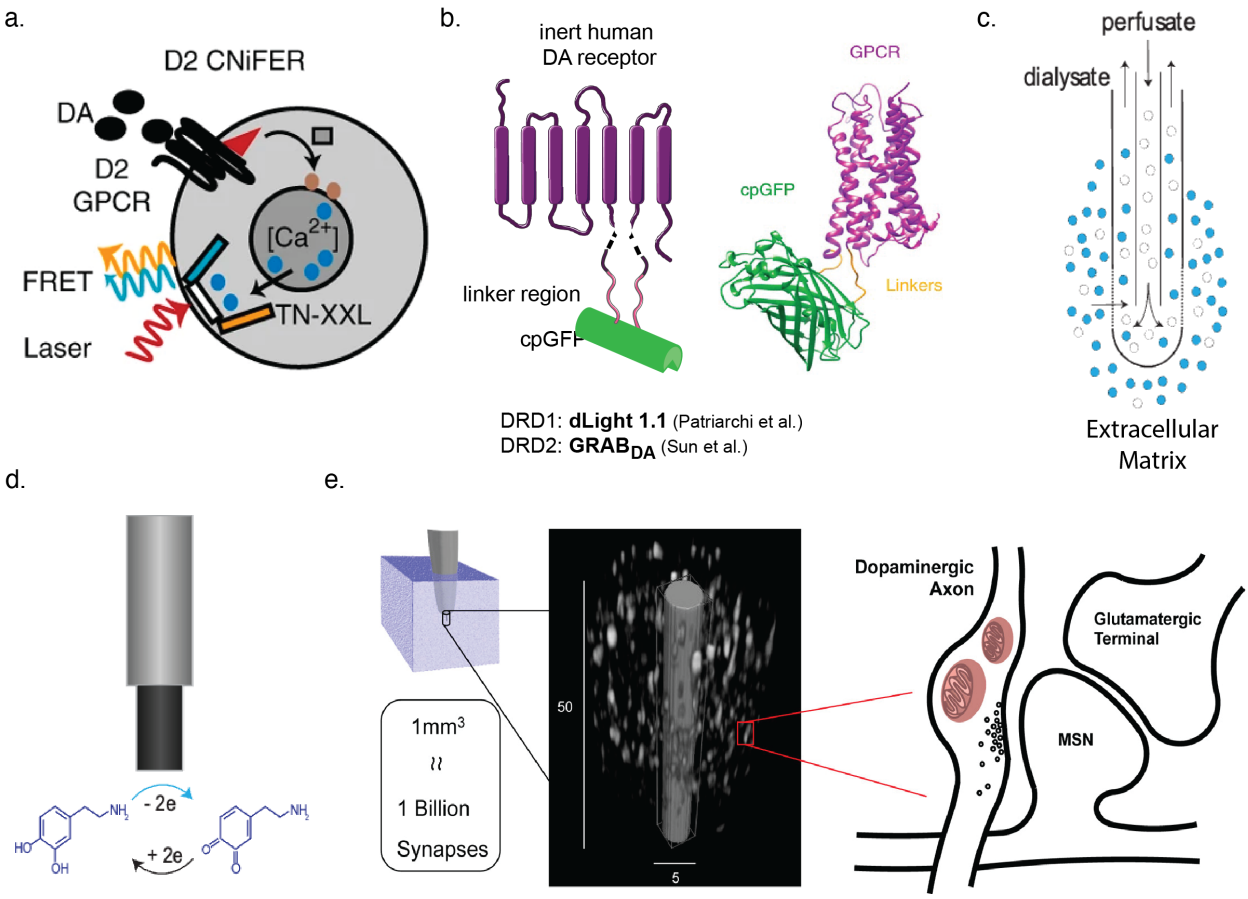

Figure 2.1: Tools and sensor for the measurement of dopamine release A. Diagram of a CNiFER cell expressing D2 receptors for the measurement of dopamine release. Binding of free dopamine drives the release of intracellular calcium to activate the FRET TN-XXL sensor (Reproduced with permission from Muller et al.[5]. B. Diagram of sensor design of genetically encoded dLight and GRAB-DA nanosensors. Left diagram is a labeled cartoon and right image shows the corresponding protein structure (Reproduced with permission from Beyene Delevich et al.[6]). C. Diagram of a microdialysis probe. White circles represent molecules of perfusate and blue circles represent target analyte . D. Diagram of dopamine oxidation at the tip of a Fast Scan Cyclic Voltammetry (FSCV) Probe. E. Three dimensional model of a FSCV probe within a 1mm^3 square of striatal brain tissue. Within a small volume of brain tissue, a single FSCV probe averages release from on the order of 1 billion dopamine synapses. (Reproduced with permission from Sames et al.[7])

the extracellular space could lead to analyte depletion from the tissue surrounding the probe. This phenomenon can lead to altered neurochemical dynamics in the tissue surrounding the probe. Zero-net-flux microdialysis, in which the perfusate is prepared with a pre-determined concentration of analyte to minimize or eliminate analyte concentration gradients can be used to minimize impacts of analyte depletion in tissue surrounding the probe thought it does not completely eliminate the risks of analyte depletion.

Voltammetry and amperometry are electrochemical methods that are widely used for quanti-

fying the neurochemistry of specific redox active molecules, such as dopamine, norepinephrine, and serotonin. These methods serve as the gold-standard for sensing fast dopamine dynamics due to their ability to measure millisecond-scale transients in analyte concentration. During voltammatery and amperometry, microelectrodes are introduced into the brain and voltage is applied to the microelectrode tip to oxidize analytes within the surrounding brain milieu (Fig.2.1d). The current generated by the oxidation of the analytes can be quantitatively measured to determine the analyte concentration. The specific use of a rapid potential sweep at the microelectrode tip to identify brain analyte concentrations is often referred to as fast scan cyclic voltammetry (FSCV). Measurement of catecholamines such as dopamine and norepinepherine are particularly well suited for study using FSCV due to their electroactive nature. Many neurotransmitters, including glutamate and acetylcholine, are not inherently electroactive and thus are not readily measured by FSCV. This allows for specific measurement of catecholamines using FSCV even in the presence of other analytes in the brain milieu. Though FSCV microelectrodes share a similar probe geometry to microdialysis probes, FSCV provides significantly improve spatial resolution over microdialysis due to its ability to utilize thin electrodes. Carbon fiber electrodes for FSCV can be constructed at the scale of single-digit micrometer width scales, resulting in improved spatial resolutions of more than an order of magnitude compared to microdialysis. This imparts spatial advantages while studying catecholamine release in *ex vivo* brain slices and results in less damage to the surrounding brain during surgical implantation for *in vivo* measurements. However, despite its comparative improvement in spatial resolution over microdialysis probes, FSCV measurements remain an order of magnitude larger than the size of a synaptic release site and are only able to sense dopamine release occurign within the immediate vicinity of the probe surface (Fig.2.1e). As such, FSCV best suited for measuring ensemble averaged activity arising from stimulation of hundreds of dopaminergic neuronal terminals (sites of neurotransmitter release) in regions of dense catecholamine ennervation and release such as the striatum and nucleus accumbens. In contrast FSCV measurement is not a robust tool for measurement of dopamine release in areas of the brains with sparse catecholamine terminal distribution such as the neocortex. Despite these caveats, FSCV remains an important non-genetically encoded complement to the genetically encoded dopamine sensors dLight and GRAB-DA as a tool that can take quantitative measurements of dopamine release with no expression time and is compatible with dopamine receptor pharmacology.

Improved spatial resolution of dopamine release can be found through use of fluorescent false neurotransmitters (FFNs) and FM dyes (named after their inventor Fei Mao)[100;101]. Both FFNs and FM dyes adopt similar strategies towards visualizing single neurotransmitter release events, seeking to be packaged into the neuron's endogenous vesicles while emitting a fluorescent output that can be monitored to report release events. FFNs are fluorescent molecules synthesized with chemical moieties that can be recognized by a target vesicular transporter. In the case of FFN for dopamine FFN511 an ethylamine side chain is covalently linked to a fluorescent coumarin core enables recognition and uptake through the vesicular dopamine transporter VMAT2[100]. In contrast. FM dyes are synthesized with lipophilic moieties that partition into the plasma membranes and other hydrophobic domains in the cytoplasm. When trapped in hydrophobic domains, such as the inside of a synaptic vesicle, FM-dyes demonstrate an increase fluorescence by two orders of magnitude. As such, changes

in fluorescent intensity can be monitored during FM dye experiments as a reporter of vesicle exocytosis. Because FFNs and FM dyes are incorporated at the level of vesicular release, their use allows for visualization of dopamine release at the level of single release sites. This allows for investigation of fundamental parameters of dopamine release such as probability of release and mobilization of vesicular pools over successive stimulation. However, FFNs and FM dyes exhibit two notable caveats: lack of direct neurotransmitter sensing and minimal use in vivo. FFNs and FM dyes seek to recreate dopamine release profiles rather than directly sensing release of endogenous dopamine already packaged within neurons. As such, tracking of FFNs and FM dyes are able to provide limited information on the biological dynamics of dopamine release such as the spatial extent of their diffusion, reuptake dynamics, or response to pharmacology or disease state. Furthermore, the intensive procedures reuqired for loading of FFNs and FM dyes into neurons has resulted in their use primarily in acute brain slices or neuronal cell cultures. As such, demonstrated use of FFNs and FM dyes *in vivo* to report on dopamine release dynamics has yet to be demonstrated.

2.1.5 Imaging Dopamine Release Using Single Walled Carbon Nanotube Sensors

Within this landscape of tools for dopamine sensing, we have developed a new non-genetically encoded, near-IR (nIR) catecholamine nanosensor (nIRCat) capable of identifying 2-µm dopamine release hotspots in dorsal striatal brain slices. In the sections below I provide an overview of the single walled carbon nanotube (SWNT) sensors and the engineering optimizations that make nIRCat a uniquley powerful sensor suited for imaging catecholamine release in the brain. I also discuss the development of an optimized protocol for nIRCat imaging in *ex vivo* brains slices and breifly discuss the adaptation of this protocol for passivated SWNT sensors.

2.1.6 Single Walled Carbon Nanotube Sensors

NIRCat is a single walled carbon nanotube (SWNT) based sensor that utilizes the SWNTs' native ability to fluoresce in the near-infrared (NIR) via exciton recombination along the 1-dimensional nanoparticle. The NIR I window (650 nm - 950 nm) is well documented to provide optical advantages for imaging non-invasively deep within the brain due to its position at a local minimum in the tissue absorption spectrum where there is decreased absorbance of NIR wavelengths by hemoglobin and water (Fig.2.2a). This allows for deeper imaging within the brain without the need for invasive procedures such as skull thinning or generation of a cranial window[102]. An additional transparency window, referred to the NIR II region (1000 nm – 1350 nm), has also been identified experimentally and computationally to give even greater optical tissue penetration depth than the NIR I region.

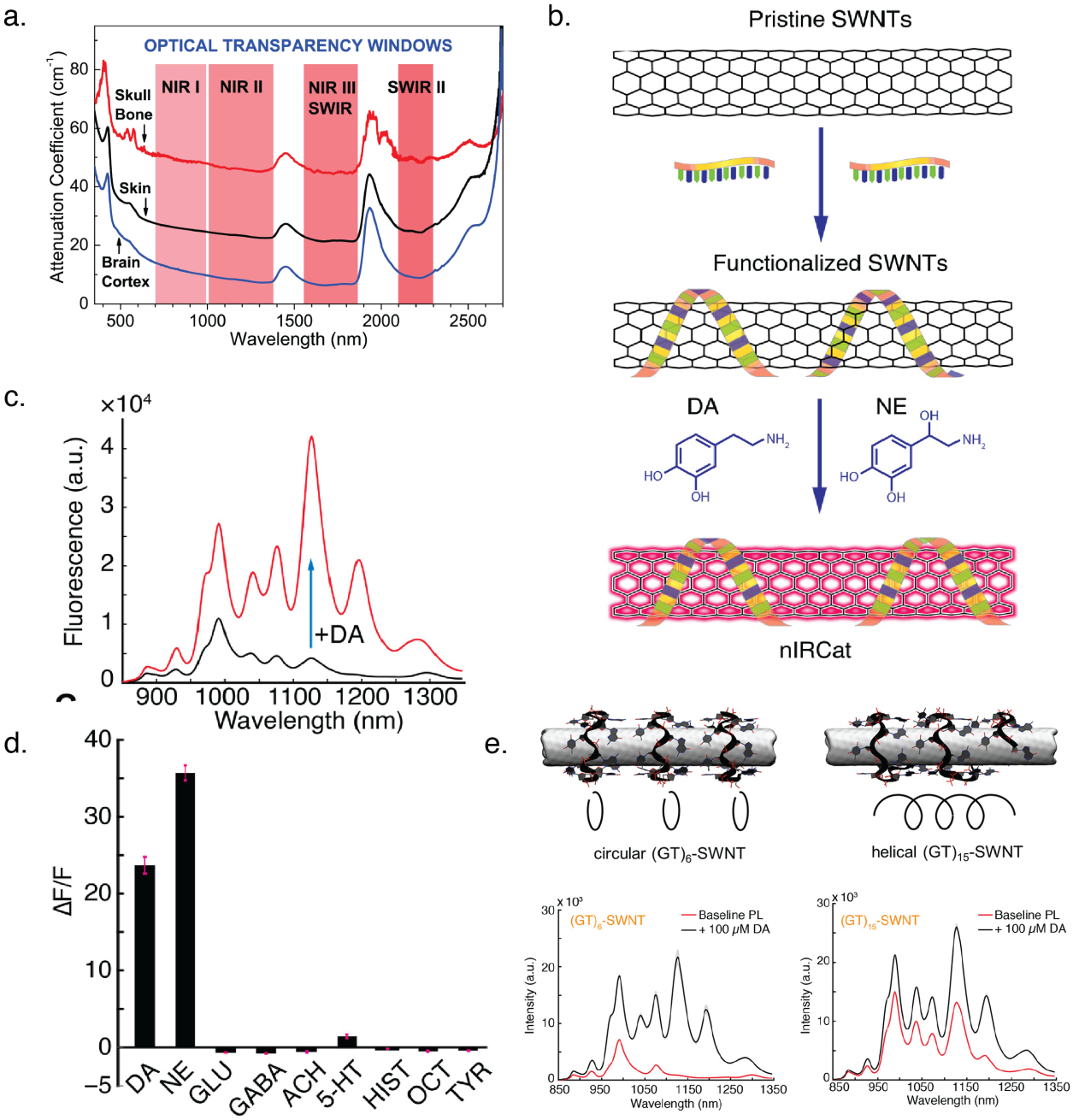

Figure 2.2: Imaging catecholamine neuromodulators using the single walled carbon nanotube nearinfrared catecholamine nanosensors (nIRCat) A. Plot of four optical transparency windows for biological imaging across the near-infrared wavelengths. The transparency windows are located in the folling range: 700 to 1000 nm (NIR-I), 1000 to 1350 nm (NIR-II), 1550 to 1870 nm (NIR-III or SWIR) and 2100 to 2300 nm (SWIR-II) (Reproduced with permission from Golovynskyi et al.[8]). B. Diagram of how nIRCat nanosensors are synthesized from pristine single walled carbon nanotubes and $(GT)_6$ (Reproduced with permission from Beyene et al.[9]). C. nIRCat nanosensors show a robust turn-on optical response in the near-infrared wavelengths upon dopamine binding (Reprinted (adapted) with permission from Beyene et al. Copyright 2022 American Chemical Society)[9]). (Continued on next page)

Figure 2.2: D. nIRCat nanosensor show specific response to the catecholamines dopamine and norepinephrine over other common neurotransmitters and signaling molecules (Reproduced with permission from Beyene et al.[9]) E. Structures predicted from computational modeling of ss-DNA–SWNT nanosensor complexes for $(GT)_(15)$ and $(GT)_(6)$ nanosensors. The ring formation predicted for $(GT)_(6)$ SWNT sensors is hypothesized to drive a quenched sensor baseline that results in a larger turn-on response (Reproduced with permission from Beyene et al.[103])

Given these favorable optical properties, creation of near-infrared fluorophores has been of great interest. Both synthetic and fluorescent protein fluorophores have been generated for near-infrared wavelengths[104]. Of these, the SWNTs have emerged as an attractive platform due to their NIR bandgap which confers a non-photobleaching NIR fluorescence that does not attenuate even after 10 hrs[105]. of continuous excitation. This allows for samples to be observed repeatedly over extended time courses to probe long-term phenomena.

SWNTs can be adapted into sensors through the introduction of a molecular recognition moeity that is able to modulate the SWNT fluorescence upon target binding. This can be achieved through Corona Phase Molecular Recognition (CoPhMoRe) where SWNTs are functionalized with a bio-mimetic polymer to form a corona phase at the nanotube surface[106]. This dynamic corona can interact and rearrange in response to the presence of specific molecular targets, driving modulations in SWNT fluorescence (Fig.2.2b). Prior to the development of nIRCat, the most extensively studied SWNT-based sensor was the $(GT)_{15}$ dopamine nanosensor constructed from the absorption of a 15 repeat guanine and tyrosine DNA oligonucleotide sequence onto the SWNT surface[107]. $(GT)_{15}$ shows and 80% increase in fluorescence upon wash on of 100 µM dopamine *in vitro*. During dopaminergic neurons burst firing dopamine concentration peaks at 1µM, which would drive only a $\Delta F/F = 0.3$ from a $(GT)_{15}$ dopamine sensor. In response to this need, the high fluorescence modulating $(GT)_6$ dopamine sensor was developed with a fluorescence response $\Delta F/(F)_0$ of 2400% in the presence of 100 µM dopamine and $\Delta F/(F)_0$ of 3500% in the presence of 100 µM norepinepherine (Fig.2.2c)[103]. The sensor shows stronger binding for dopamine than norepinepherine with K_d values of 10 µM and 35 µM resectively[9]. Notably, $(GT)_6$ shows a strong selectivity for the catecholamines dopamine and norepinepherine while showing little binding or fluorescence response for competing signaling molecules also present in the brain milieu such as glutamate, acetylcholine, and GABA (Fig.2.2d)[9].

The exact binding mechanism of dopamine on $(GT)_6$ leading to fluorescence modulation has not been experimentally elucidated. However, insights from quantum mechanical molecular dynamics simulations have provided hints at how this dynamic process may occur[103]. After nanosensor synthesis $(GT)_{15}$ and $(GT)_6$ DNA oligonulceotides can both adopt helical conformations on the SWNT surface to expose the hydrophilic DNA backbone to the aqueous solvent. In the presence of dopamine, the catechol group within the dopamine molecules is hypothesized to interact with SWNT lattice through π-π stacking, displacing the wrapped DNA oligonucleotides and increasing the SWNT fluorescence intensity[103]. Recent simulations have indicated that the short length of $(GT)_6$ DNA also allows for the dense adsorption of multiple oligonucleotides on the SWNT surface in a ring arrangement

(Fig.2.2e). This dense assembly of $(GT)_6$ oligos effectively serves as a dopant on the surface of semi-conducting SWNT, polarizing the SWNT and forming a superlattice from the perspective of 1-dimensionally confined excitons. As a result, the $(GT)_6$ "dopant" promotes non-radiative transitions and suppresses radiative relaxation. In this way the baseline fluorescent of $(GT)_6$-SWT constructs is lower than that of $(GT)_{15}$-SWNT constructs, allowing for stronger turn-on response in the presence of dopamine (Fig.2.2e).

2.1.7 The Near-infrared catecholamine sensor (nIRCat)

$(GT)_6$-SWNT constructs are capable of imaging dopamine release in *ex vivo* brain slices and have been name nIRCat (near-infrared catecholamine sensors). Amongst tools currently available for directly imaging dopamine modulation, nIRCat is unique in its high spatiotemporal resolution, compatibility with pharmacology, and ability to be deployed in non-model organisms. The rapid fluorescence response of nIRCat nanosensors combined with their nanoscale size permits dopamine imaging in the brain extracellular space at spatiotemporal resolutions finer than microdialysis, and at higher spatial resolution than fast scan cyclic voltammetry. In contrast to fluorescent protein-based dopamine sensors, the synthetic nature of nIRCat dramatically improves the dopamine probe's photostability as it is inherently non-photobleaching and thus indefinitely photostable. nIRCat's near-infrared fluorescence can be readily multiplexed with other optical tools such as calcium or voltage indicators, whose fluorescence resides in the non-overlapping visible wavelength spectrum. Furthermore, labeling living brain tissue with nIRCat is rapid and straightforward, requiring only passive incubation followed by washing and thus circumventing genetic manipulation. This passive labeling approach 1) avoids the necessity to work with genetically-tractable organisms, 2) avoids the use of AAV vectors to deliver the probe, and 3) bypasses the expression time required between probe administration and imaging. These features may be uniquely advantageous for researchers studying the role of dopamine in disease progression, allowing early-age and multiple time points to be sampled without the need to introduce additional genetic manipulation to a disease model. Finally, because the binding paradigm of dopamine to nIRCat is distinct from that of the native dopamine receptor, nIRCat does not optically respond to numerous dopamine receptor agonists and antagonists. This pharmacological compatibility of nIRCat enables direct visual investigation of therapeutically-relevant agents and their effects on dopamine modulation in the vicinity of its release sites. It should be noted that nIRCat presently has only been validated in *ex vivo* brain slices and remains to be implemented *in vivo*. Furthermore, nIRCat is not able to distinguish between dopamine and norepinephrine release. As a result nIRCat can only be used as a sensor for dopamine release in regions of the brain where dopamine is released in the absence of major norepinephrinergic innervation. Notably, nIRCat may be an attractive tool to use in organisms lacking norepinephrine signaling such as drosophila melanogaster, in which octopamine – known not to interfere with nIRCat fluorescence – replaces norepinephrine. However, care must be taken in implementing nIRCat for imaging mouse brain regions such as the cortex where multiple catecholamine signals may be present.

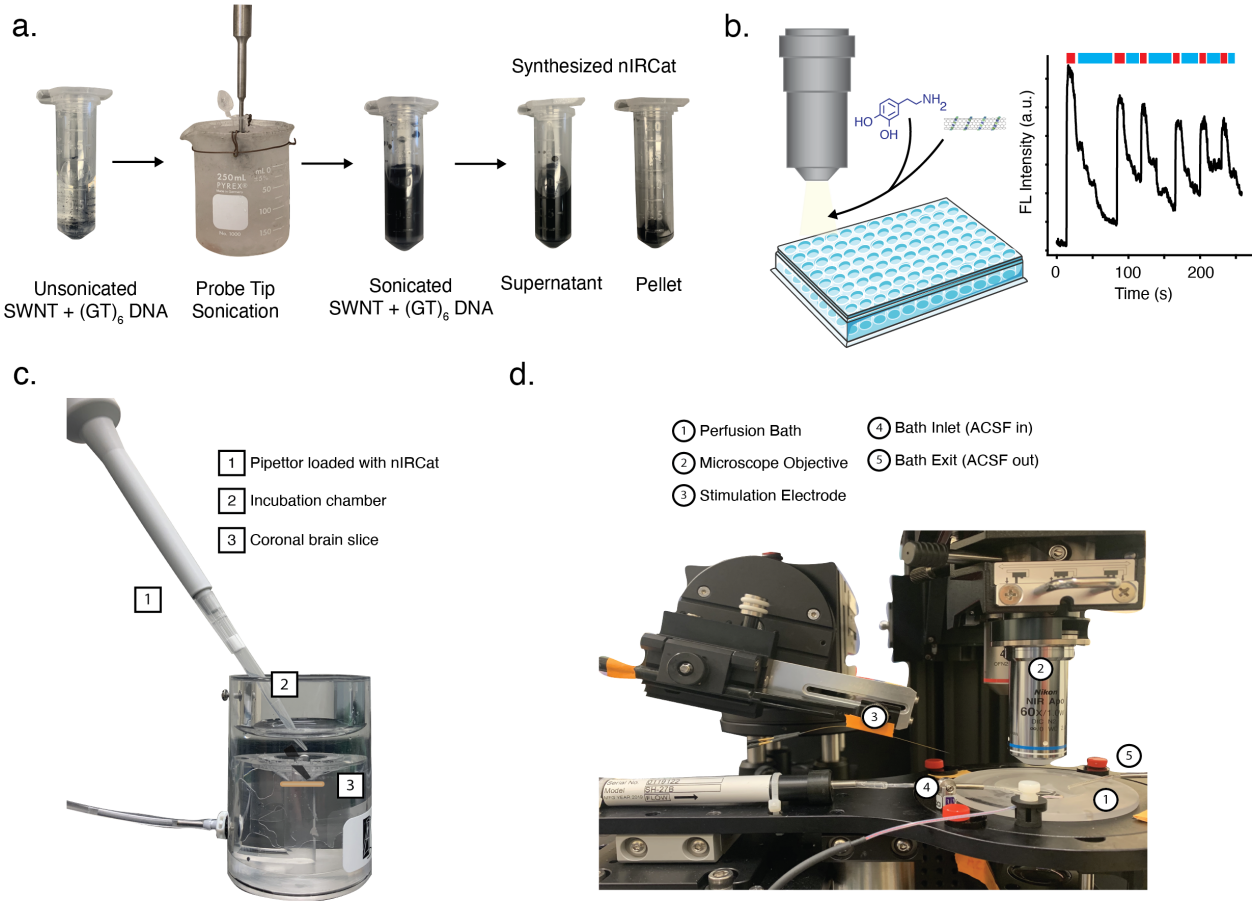

Figure 2.3: Protocol for imaging dopamine release using nIRCat nanosensors A. Pictorial flow chart of nIRCat nanosensor synthesis process from SWNT and $(GT)_6$ mixing through sonication and cetrifugation B. Schematic for *in vitro* testing of nIRCat dopamine response C. Diagram of *ex vivo* brain slice nIRCat labeling process for dopamine imaging. D. Diagram of microscope stage for imaging of dopamine release in *ex vivo* brain slice using nIRCat nanosensors. Stimulated release can be achieved through electrical stimulation with electrodes or optogenetically through the microscope objective (All images Reproduced with permission from Yang et al.[10])

2.1.7.1 Protocol Development for nIRCat imaging in live brain slice

Since nIRCat's initial implementation, I have generated an optimized protocol for dopamine imaging in the dorsal striatum of *ex vivo* brain slices. In this section, I summarize best practices and considerations for onducting nIRCat imaging with a focus on methods to integrate nIRCat imaging with existing biological tools and methods from electrophysiology. These methods have been used image electrically or optogenetically stimulated dopamine release in living brain slices from standard mouse models mice (Charles River and Jackson Labs C57BL/6 mice), disease model mice, and non-model organisms such as wild mice. I have also conducted validated this protocol in mice as young as 32 days and as old as 92 days, as well as in both male and female mice. In contrast to genetically-encoded dopamine sensors, nIR-

Cat is compatible with dopamine pharmacology, enabling the study of how therapeutically-relevant dopamine receptor agonists and antagonists shape dopamine modulation across the basal ganglia. To date we have validated the use of nIRCat imaging to investigate wash on of the drugs Nomifensine, Sulpiride, Quinpirole, DHβE, and 4-aminopyridine.

2.1.7.2 nIRCat Synthesis and Characterization

Synthesis of nIRCats occurs through dispersal of single walled carbon nanotubes (SWNT) with single-stranded DNA oligonucleotides composed of six guanine and thymine repeats (GT6) (Fig.2.3a). This dispersal process is achieved through bath and probe tip sonication, which allows the (GT)6 polymers to non-covalently adhere to the surface of the SWNT via π-π stacking interactions to form the nIRCat nanosensor. The resulting individually dispersed semi-conducting SWNTs exhibit intrinsic nIR fluorescence emission with peak wavelengths ranging from 900-1500 nm depending on the chirality of the carbon lattice, a phenomenon absent from metallic nanotubes, nanotube bundles, and multi-walled carbon nanotubes. As such, effective sonication of the initial GT6 and SWNT mixture is integral to successful synthesis of the nIRCat nanosensor (Fig.2.3a). SWNT can be introduced to the synthesis reaction as either hydrated SWNT cake or as a SWNT-water slurry. While both methods can be used to generate robust nIRCat nanosensor, it is recommended to use a SWNT-water slurry mixture when preparing large sensor preparations for biological imaging experiments to reduce variability between syntheses. Sensors produced in bulk should also be synthesized in small batches in individual eppendorf tubes and then pooled, as preparation in larger volumes reduces the efficacy of sonication. Centrifugation and recovery of the supernatant is also a key step that allows the successfully synthesized nIRCat nanosensor to be separated from the remaining, non-suspended SWNT (Fig.2.3a). Failure to separate unsuspended and functionalized SWNT from the nIRCat synthesis may result in increased baseline fluorescence and diminish the strength of the sensor $\Delta F/F$. Individual optimization around sonication time and starting SWNT to GT6 ratio may be required to achieve efficient nIRCat nanosensor synthesis in individual lab conditions and for indivdual preparations of SWNT suspensions. As such, characterization of synthesized nIRCat nanosensor for robust response to dopamine *in vitro* is prior to sensor pooling and finalization for biological imaging.

The adsorption of GT6 to the SWNT surface both aids the dispersal of the SWNT in aqueous solution and confers a catecholamine-selective increase in fluorescence to the nIRCat nanosensor. Robust performance of nIRCat nanosensor in acute brain slices requires thorough in vitro solution phase characterization to confirm a strong, catecholamine-specific fluorescence response and a fast, reversible fluorescence that changes with dopamine release and reuptake. Newly synthesized nanosensor should be comfirmed to show a large increase in fluorescence when dopamine is added exogenously to a wellplate containing the nanosensor. Nanosensor response should be tested for multiple dopamine concentrations ranging from 1 nM to 1 mM to ensure that the nanosensor shows a dynamic response to biologically-relevant dopamine concentrations. Similarly, nanosensor reversibility should be tested by immobilizing the nanosensor in a microchannel and ensuring the nanosensor increases and

decreases in fluorescence as dopamine is washed into and out of the channel (Fig.2.3b). It should be noted that before introducing a new drug wash experiment, all drugs should be tested alongside nIRCat nanosensor in in vitro solution phase experiments to ensure that the drug does to affect the nanosensor fluorescence response or reversibility.

2.1.7.3 Imaging Dopamine Release in Acute Brain Slice

Introducing nIRCat nanosensor into acute brain slices is a straightforward procedure that requires the acute brain slice to be passively incubated in artificial cerebrospinal fluid containing 2 mg/L of nIRCat nanosensor for 15 minutes (Fig.2.3c). These incubation parameters have been determined experientially to produce well-labeled acute brain slices for imaging, but may be adjusted to better serve individual experimental setups, particularly if the thickness or permeability of the prepared brain slices has been altered.

To specifically image dopamine dynamics without additional signal from other catecholamines, users should aim to imagine in the dorsal striatum, which is densely innervated by dopaminergic neurons from the substantia nigra pars compacta and lacks innervation from norepinephrine-releasing neurons. Dopamine release can be triggered by either electrical stimulation of brain tissue or by shining blue light on acute brain slices expressing channelrhodopsin (Fig.2.3c). The most appropriate dopamine release method will vary based on the desired experimental design. While optogenetic release of dopamine allows for controlled, dopamine-specific release from specific cell types, it also requires that mice are injected with channelrhodopsin AAV roughly 3-4 weeks before imaging takes place. Conversely, electrical stimulation elicits general neuromodulator and neurotransmitter release, but can be mobilized in both unmanipulated and genetically-manipulated brain tissue. While in the dorsal striatum, dopamine release can be successfully driven by a single 1 ms pulse or a train of pulses. Users should note that electrical stimulation often results in the formation of bubbles at the electrode surface. At high stimulation strengths, these bubbles may deform the tissue, resulting in movement artifacts during data acquisition. To reduce these disturbances, it is suggested that users consider using lower-impedance electrodes (e.g. platinum over tungsten), perform experiments with shorter stimulation pulses, or position the stimulator carefully into the tissue to prevent motion. Some motion artifacts such as progressive x-y drift can also be corrected through data processing procedures. However, as much care as possible should be taken to experimentally minimize the extent of drift during data acquisition.

Imaging using dopamine pharmacology can be readily accomplished once acute brain slices have been generated and the pharmacological drug has been confirmed *in vitro* to not interfere with nIRCat response. Depending on the mechanism of drug or toxin action, the pharmacological agent can be introduced to the acute brain slice via incubation in parallel to the nIRCat labeling or through continuous wash on during labeling. During continuous wash on experiments, acute brain slices should sit under continuous wash on of the pharmacological agent for a determined incubation time before commencing post drug-wash imaging. For drug wash experiments seeking to track changes in dopamine hotspots intensity and activity, it is particularly critical to ensure that the same imaging field of view is main-

tained before and after drug wash to allow effective tracking of single dopamine hotspots over successive conditions.

2.1.7.4 Adapting nIRCat Imaging Protocols for Passivated nIRCat Nanosensors

The small size of nanoscale tools for biological research often correlates to increase biocompatibility and decrease invasiveness in comparison to their micro- or macroscale counterparts. However, increasing evidence suggests that the biological impact of these nanotechnologies on the local brain microenvironment is not negligible–particularly at long time scales on the order of days[11]. While inside protein-rich brain extracellular space, SWNT nanosensors can adsorb nonspecific complement protein or interact with with macrophages via toll-like receptors 2 and 4, activating the complement pathways and release of cytokines respectively and driving an inflammatory response. Recent work studying the impart of (GT)6-SWNT nIRCat nanosensor on SIM-A9 microglial cell morphology, has shown that exposure to (GT)6-SWNTs at 5 µg/mL can drive dramatic changes in cell morphology over the course of 4 hrs[11]. Notably, most *ex vivo* acute slice research is completed within 4 hours before aberrant microglia morphologies form. However, minimization of inflammation response to (GT)6-SWNTs is a paramount challenge in the development of nIRCat nanosensor for long-term *in vivo* imaging.

In this light, a passivated (GT)6-SWNT nanosensor with a polyethylene glycol (PEG) conjugated phospholipid was developed to improve nanosensor biocompatibility while maintaining dopamine sensing function. Unlike covalent modification of the pristine carbon lattice surface, noncovalent passivation of (GT)6-SWNT surface with PEG2000-PE preserves the intrinsic SWCNT nIR fluorescence and the (GT)6-SWNT molecular recognition for dopamine. In a collaboration with the development of this sensor, I adapted the optimized nIRCat imaging protocol to perform *ex vivo* dopamine images in brain slices with PEG2000-PE passivated (GT)6-SWNT. During this comparative study of (GT)6-SWNT nIRCat nansenseors and PEG2000-PE passivated (GT)6-SWNT, both sensors were introduced into acute coronal brain slices by incubating fresh, 300 µm thick coronal brain slices in artificial cerebral spinal fluid (ACSF) containing 2 µg/mL of dopamine nanosensor (Fig.2.4a). The nanosensor-labeled slices were then washed with ACSF and imaged in a continuously perfused ACSF bath. Ielectrically stimulated dopamine release from dopamine-containing axons within the dorsal lateral striatum and simultaneously imaged SWCNT nIR fluorescence response to changes in extracellular dopamine concentration. As expected, slices labeled with (GT)6SWCNTs showed low nIR fluorescence signal prior to stimulation, followed by an increase in fluorescence response immediately after 0.3 mA electrical stimulation, and an eventual return to the low intensity baseline approximately 5s after stimulation (Fig.2.4b). Brain slices labeled with PEG2000-PE/ (GT)6-SWCNTs showed a similar nIR fluorescence response to 0.3 mA electrical stimulation (Figure 6c), suggesting both the native dopamine probe and the PEG2000-PE-passivated probe enable imaging of dopamine release and reuptake kinetics in striatal brain tissue. I next characterized the nanosensor performance

by testing its response to evoked dopamine release from striatal tissue. As described previously by Beyene et al., we programmatically identified spatial regions of interest (ROI) within the imaged brain tissue in which statistically significant increases in SWCNT fluorescence were recorded upon electrical stimulation (0.3 mA) of dopamine release. These ROI represent spatial subregions where dopamine release and reuptake modulation occur during electrical stimulation. Fluorescence time traces from ROIs were normalized to baseline fluorescence (ΔF/F0) and averaged across four brain slices per SWCNT treatment and three stimulation recordings per slice. Average ΔF/F0 of time traces from both (GT)6SWCNT and PEG2000-PE/(GT)6-SWCNT labeled slices show that both nanosensors demonstrate a robust fluorescence response to dopamine released in living brain slices followed by a rapid return to baseline as dopamine is cleared from the extracellular space (Figure 6d).For the same 0.3mA stimulation intensity, PEG2000-PE/(GT)6-SWCNTs exhibited a peak ΔF/F0 of 0.032 ± 0.002 compared to 0.021 ± 0.003 for unmodified (GT)6-SWCNTs (Figure 6e). This increased peak ΔF/F0 indicates improved dopamine responsivity by PEG2000PE/(GT)6-SWCNTs compared to the unpassivated counterpart. PEG-phospholipid modified SWCNTs also improved ROI identification. In acute brain slices labeled with PEG2000PE/(GT)6-SWCNTs, 158 ± 37 ROI were identified versus 81 ± 15 ROI in (GT)6-SWCNT labeled slices (Fig.2.4c). The higher ROI number may indicate improved extracellular access to dopaminergic terminals within the brain tissue, or increased sensitivity of passivated nanosensors for dopamine. Conversely, PEG2000-PE/(GT)6-SWCNTs show significantly higher decay constants, indicating a slower return to baseline fluorescence (Fig.2.4g). It is not known whether this effect is due to altered nanosensor kinetics arising from PEG-phospholipid modification or if it arises from the higher nanosensor sensitivity and increased peak nanosensor ΔF/F0. As an additional control, stimulation at higher intensity (0.5 mA) revealed similar trends for the above metrics. However, the increase in peak ΔF/F0 and ROI number from PEG2000-PE passivation was diminished. This may indicate saturation of the sensors from increased dopamine release at the higher electrical stimulation intensity. Nevertheless, the passivated PEG2000-PE/(GT)6-SWNT dopamine nanosensor displays higher sensitivity over (GT)6-SWNT, particularly at lower dopamine concentrations, suggesting dopamine nanosensors and other SWNT-based neurotechnologies may benefit from this passivation approach. As such, we show that this *ex vivo* acute brain slice protocol not only facilitates robust imaging of dopamine for (GT)6-SWNT but also for other SWNT nanosensor constructs. To date, this imaging protocol has also been adapted to image seratonin in *ex vivo* brain slices and oxytocin in the dorsal raphe nucleus. This versatility has underscored that the methods developed for optimized nIRCat probe synthesis and implementation are fundamentally generic for other carbon-nanotube based neuromodulator nanosensors. As such, the methods developed in this work will be of broad-scale utility to researchers wishing to image other neurochemicals as this toolkit expands. Lastly, the synthetic nature of nIRCat and other nanosensors of its class can be applied to any prepared live tissue without genetic manipulation, including brain tissue from different mouse lines or non-model organisms. These adaptations of nIRCat for use in other organisms could enable neuromodulation research in organisms previously unexplored by the neurobiology research community.

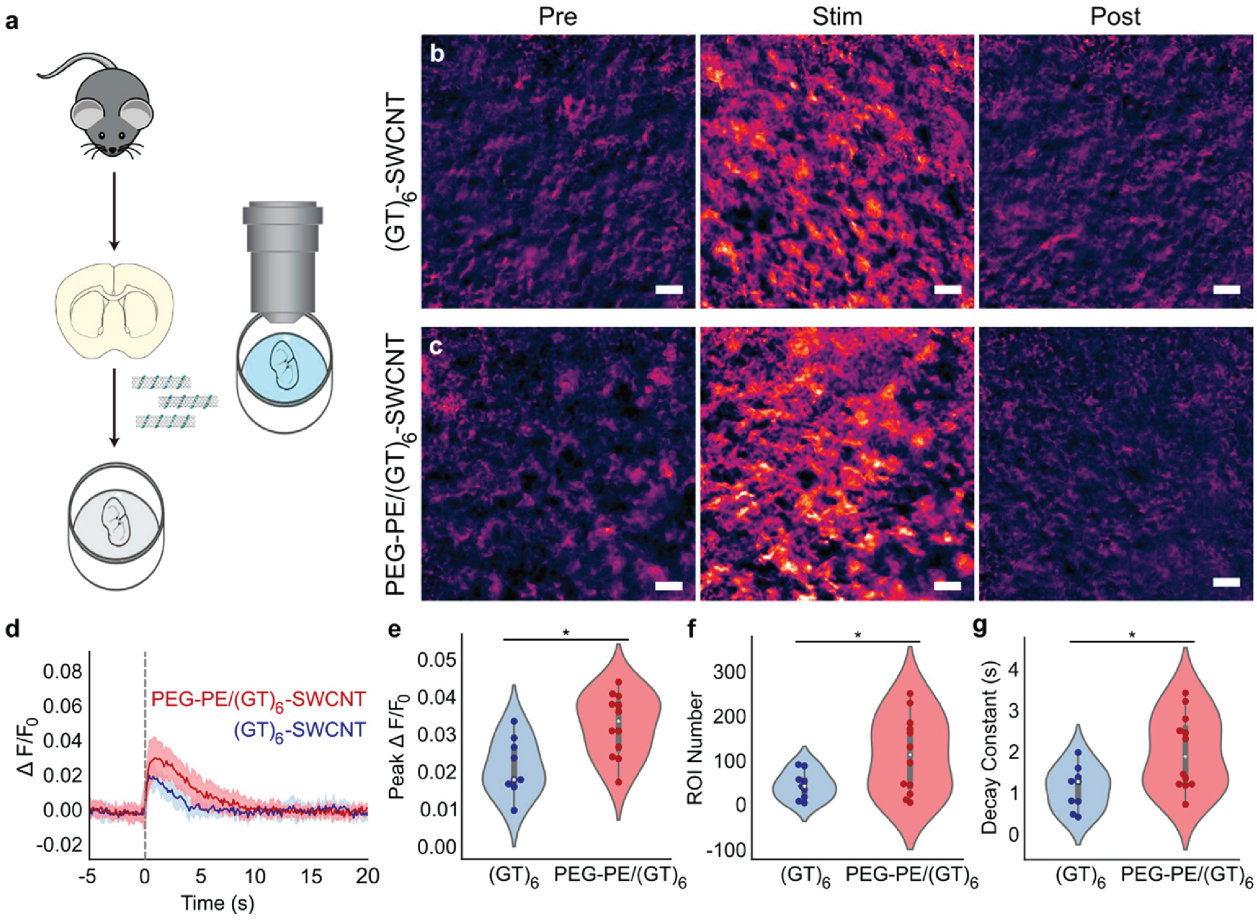

Figure 2.4: Imaging of dopamine release and reuptake dynamics in *ex vivo* brain slices using PEG2000-PE passivated (GT)6-SWCNT (a) Schematic of acute mouse brain slice preparation and incubation with SWCNT nanosensors before dopamine release and reuptake imaging. (b,c) Representative images showing normalized nIR fluorescence signal (ΔF/F0) of (b) (GT)6-SWCNT and (c) PEG2000-PE/(GT)6-SWCNT in striatum of mouse brain before stimulation, at peak ΔF/F0 shortly after 0.3 mA single-pulse stimulation, and after SWCNT nanosensor signal returned to baseline. Scale bars are 10 µm. (d) Fluorescence response time trace of identified regions of interest (ROI) in brain slices labeled with (GT)6-SWCNT (blue) and PEG2000-PE/(GT)6-SWCNT during electrically evoked dopamine release. Dashed line indicates time of 0.3 mA single-pulse electrical stimulation. Solid lines represent mean traces and shaded regions represent one standard deviation around the mean for 3–4 mice, 1 brain slice per mouse, and 3 recordings per slice ((GT)6, N = 9; PEG–PE/(GT)6, N = 12). (e–g) Violin plots showing the distribution of metrics from each mean nanosensor fluorescence trace for (e) peak ΔF/F0 signal, (f) number of identified regions of interest (ROIs), and (g) decay constant from fitting mean nanosensor ΔF/F0 time trace a first-order decay function. Dark points represent measurements calculated from a single stimulation recording. White dots represent the mean. The gray bar spans the spread of the data while the bold portion of the bar spans from the first to third quartiles. The shaded regions represent the probability density of the data across the range of the metric measured. *p ¡ 0.05. (All images reproduced with permission from Yang, Yang et al.[11])

Chapter 3

Characterizing Changes in Dopamine Release in R6/2 Huntington's Disease Model Mice with nIRCat Imaging [iii]

[iii]This section is produced in part with permission from the following work: Yang, S. J., et al. "Synaptic scale dopamine disruption in Huntington's Disease model mice imaged with near-infrared catecholamine nanosensors."

3.1 Abstract

Disease-related changes in dopamine signaling have been well documented in human Huntington's Disease (HD) patients. Patients show elevated levels of dopamine early in disease followed by decreasing levels late in disease. This biphasic dynamic is hypothesized the drive coincident motor changes in patients from hyper-active chorea to hypo-active bradykinesia. Understanding the origin for changes in dopamine release during HD has been largely facilitated by the development of trangenic murine models for HD. In this chapter I contextualize the role of HD animal models within HD research and provide a brief review of insights into dopamine release over the course of HD neurodegeneration gained from dopamine sensing work in R6/2 mice using microdialysis and fast scan cyclic voltammetry methods. I demonstrate how nIRCat dopamine imaging in the dorsal striatum can be used to bring new spatial insights into how HD neurodegeneration manifests through examination of three timepoints: immediately at the onset of motor degeneration (p32-35, 4 wks), mid-degeneration (p64-66, 9 wk), and late in disease (p87-93, 12 wk). I compare these findings to animal performance on a rotarod motor degeneration behavioral assay conducted in parallel to nIRCat imaging and find that decreases in dopamine release mirror decreases in animal motor fitness. Furthermore, I utilize nIRCat's improved spatial resolution to show that compromised dopamine late in disease at 12 weeks is driven by both decreases in the number of active dopamine-releasing hot spots and decreases in the strength of dopamine release from individual hotspots in R6/2 HD mice during strong electrical stimulation at 0.3 mA. In contrast, altered dopamine release during weak electrical stimulation at 0.1 mA is driven by decreases in dopamine hotspot number in R6/2 HD mice, suggesting that disruptions in dopamine release in late HD are most pronounced during events requiring high levels of dopamine release. Lastly, I "spatially average" the dopamine release recorded by nIRCat imaging by multiplying the average number of dopamine hotspots by the mean peak $\Delta F/F$ and show that the dopamine release measured by nIRCat imaging is comparable to the levels measured previously in R6/2 HD mice using spatially diffuse methods of dopamine detection.

3.2 Introduction

The development of accurate animal models for Huntington's Disease (HD) has played a critical role in our understanding of the molecular and synaptic events that underlie HD driven neurodegeneration. In particular, murine models have played a large role in HD research due to their genetic tractbility and widespread availability. Early models of HD utilized selective neurotoxins such as kainic acid, quinolinic acid and 3-nitropropionic acid to produce striatal lesions reminiscent to the striatal damage characteristic of late HD [108;109;110]. While these models supported research into the repercussions of major striatal disruption, they were unable to accurately model the progressive course of disease. The identification of the huntingtin gene and development of transgenic models for HD beginning with the R6/1 and R6/2 mouse models significantly accelerated the field's understanding of both

the molecular and synaptic disruptions that occur during the course of HD. The R6/1 and R6/2 family of transgenic mice were generate through introduction of a human huntingtin construct containing the human huntingtin promotor, exon 1 of the huntingtin gene containing 130 CAG repeats, and 262 bp of intro 1 of the huntingtin gene[111]. These genes were randomly integrated into the mouse genome within the genes and expressed ubiquitously throughout the animal. The integration location for the R6/2 mouseline has been shown to be within the mouse gene Gm12695 whose function is presently unknown[112]. Though this transgene is only a fragment of the full huntingtin gene, it is sufficient to generate many of the characteristic motor symptoms associated with HD in the mouse models. The R6/1 mouse model contains a single transgene fragment of 115 CAG repeats while the R6/2 mouse model expresses an extended fragment of 150 CAG repeats that likely originated as a triple integration that no functions as a single copy integration due to deletions[111]. Both R6/1 and R6/2 animals continue to produce healthy huntingtin at WT levels, with additional expression of the mutant huntintin transgene expression are around 31% and 75% of the endogenous huntingtin respectively. Modeling HD using a transgenic mouseline represented a significant improvement in the animal model construct validity over toxin-based models. Continued development of transgenic model in mice has yielded new murine models including the YAC HD mouse models, which contain a full length human huntingtin gene rather than a fragment, and murine knock-in models, which position the full length mutant huntingtin gene within the appropriate location within the mouse genome[113;114;115]. These improvements in the molecular validity of transgenic HD mouselines have been particularly important for the use of mouse lines as *in vivo* validation methods for HD gene therapies which rely on accurate recapitulation of gene regulation and expression dynamics.

Throughout these developments, the R6/2 mouse model had remained a heavily used animal model due to it's fast-degeneration profile reminiscent of juvenile-onset HD. As discussed in Chapter 1 Section 1.3.3, changes in dopamine release have been implicated in Huntington's Disease progression and the development of aberrant motor symptoms. Studies in R6/2 have provided an important experimental complement to clinical studies in elucidating the nature of striatal dopamine disruption during HD by enabling connection between animal behavior and dopamine signaling. Studies utilizing microdialysis and fast scan cyclic voltammetry (FSCV) in R6/2 mice showed that basal dopamine levels and evoked dopamine release in R6/2 HD animals is progressively decreased over the course of disease, coincident with the manifestation of decreased locomotion and increased ataxia. At 6 weeks of age R6/2 HD animals show diminished locomoter response to cocaine in comparison to their WT counterparts, and by 10 weeks R6/2 HD animals show no behavioral response to cocaine enhanced dopamine release[116]. This change appears to be primarily the result of change in dopamine release dynamics, with dopamine re-uptake processes comparable between R6/2 HD mice and their WT counterparts[62;116;117]. Dopamine content within striatal neurons is decreased over the course of disease, with decreased tyrosine hydroxylase (TH) activity in both the striatum and the substantia nigra[118;119]. However, decreases in dopamine content are not large enough to fully account for the observed decreases in basal and evoked dopamine release, suggesting that dopamine release mechanisms are impaired during HD. These changes might involve decreased ability to mobilize vesicles from reserve pool vesicles. Subsequent

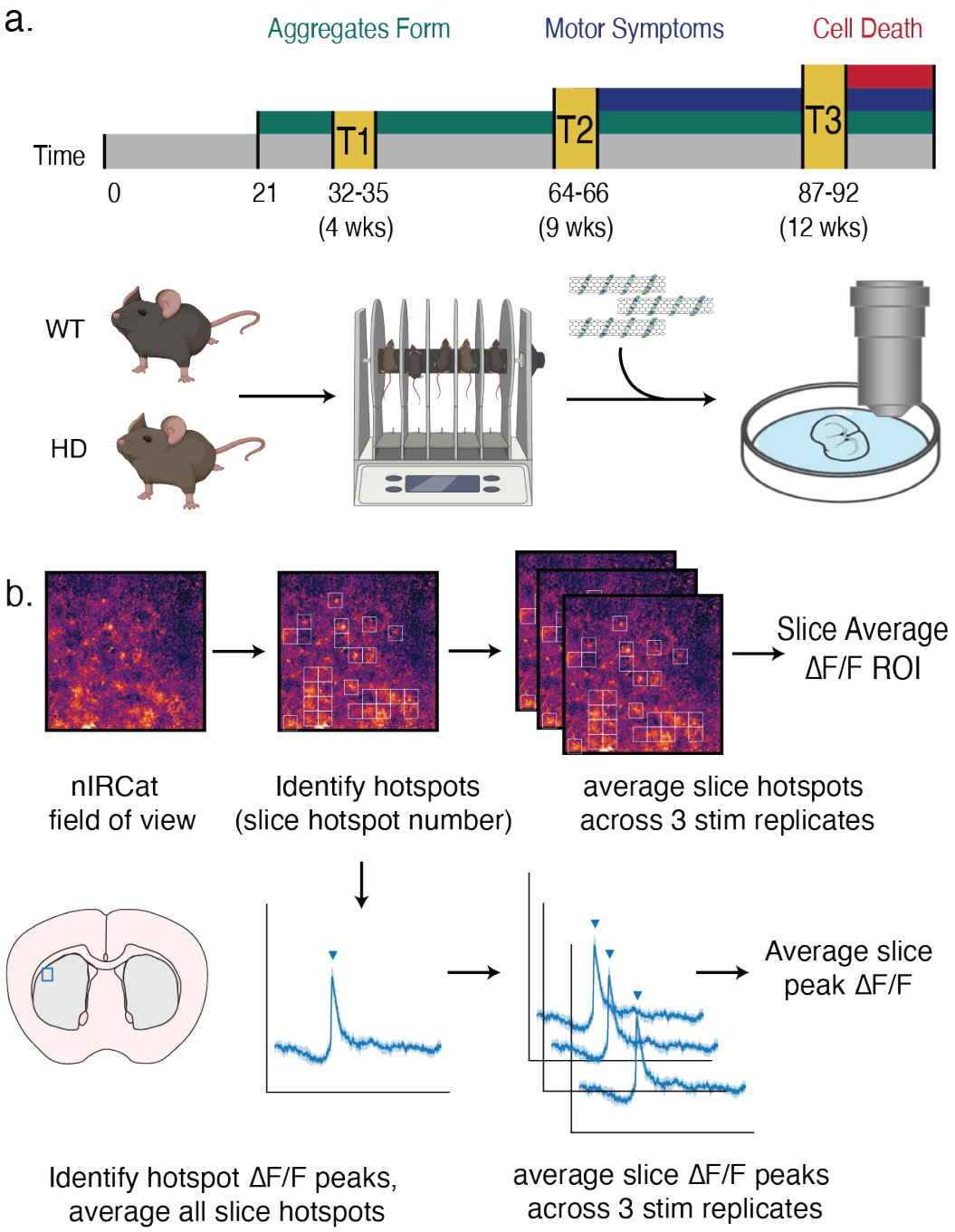

Figure 3.1: Experimental Overview of nIRCat imaging in R6/2 HD Mice A. Graphical overview of experimental design whereby 4 week, 9 week, and 12 week WT and R6/2 HD mice undergo weekly rotarod phenotypic assessment of motor ability followed by nIRCat dopamine imaging at the final timepoint. B. Graphical overview of data analysis to examine the number of putative dopamine release sites active after stimulation, termed dopamine hotspots, and the average amount of dopamine released from each site, termed average peak dopamine $\Delta F/F$

work utilizing amperometry and iontophoresis in R6/2 mice confirmed that measured changes in dopamine release were not due to changes striatal volume due to neurodegeneration

FSCV and microdialysis have revealed bulk trends in dopamine release during HD, implicating disruptions in dopamine release to locomotor changes. However, these bulk measurements are not spatially resolved enough to visualize how molecular changes arising from mutant huntingtin. For example, decreases in dopamine release could be driven by decreases in the number of dopamine hotspots, decreases in the average release from individual dopamine hotspots, or a combined effect feom decreased dopamine hotspot number and performance. Bridging this the divide between molecular and systems neuroscience and answering these questions requires the ability to visualize dopamine signaling at the level of release sites. Previous studies have examined vesicular dopamine release in R6/2 mice through the isolation and culture of R6/2 HD adrenal chromaffin cells to examine vesicle content size and number. These methods are not able to accurately recapitulate the dynamics of dopamine release from neuron terminals in the context of local circuitry[60]. As such, we image dopamine release in *ex vivo* R6/2 striatal brain slices to visualize how the number and performance of dopamine hotspots changes with disease progressive. The bulk of dopamine Huntington's Disease literature has examined dopamine release in the dorsal lateral striatum, a region associated with circuitry related to voluntary movement[117]. As such, we selected this region of the striatum to study changes in dopamine release within R6/2 mice over progressive disease development. We performed nIRCat dopamine imaging in HD mice and their WT littermates at three time points: immediately at the onset of motor degeneration (p32-35, 4 wks), mid-degeneration (p64-66, 9 wk), and late in disease (p87-93, 12 wk) (Fig. 3.1a). In parallel, the extent of motor degeneration was assessed by weekly rotarod tests. Using a time-series data analysis software previously developed for detection and analysis of nIRCat imaging data, I recorded the average number of active dopamine hotspots in each brain slice across three stimulation replicates and the average peak $\Delta F/F$ of the active dopamine hotspots in each slice (Fig.3.1b)[10]. These metrics putatively correspond to the number of dopamine releasing sites within the brain tissues and the average size of dopamine release from each release site.

3.3 Results and Discussion

3.3.1 Locomotor Changes in R6/2 Mice

We first sought to characterize the motor degeneration of R6/2 HD mice in our hands through standard behavioral assays and metrics utilized in murine Huntington's Disease research. To assay motor fitness, animals were placed on an elevated, slowly accelerating, rotating treadmill known as the rotarod and allowed to run until they fall. Time spent on the rotarod before failure is quantified as latency to fall, with animals displaying higher motor coordination demonstrating higher latency to fall. Consistent with findings from previous studies, WT mice showed consistent, robust performance on the rotarod across timepoints

from 4 to 12 weeks. In contrast R6/2 HD mice showed decreased latency to fall compared to their WT counterparts as early as 4 weeks and progressively decreased rotarod performance with disease progression through 9 and 12 weeks (Fig.(3.2a). Notably, we assay the motor fitness of animals as young as 4 weeks and show that even at this early time point R6/2 HD animals show deficits in motor fitness. This may suggest that HD related degeneration in R6/2 mice may manifest early in life when the nervous system is still actively in development.

3.3.2 Changes in R6/2 Dopamine Release 0.3 mA

Work from Beyene et al. has previously shown that nIRCat dopamine imaging in the dorsal striatum of acute slices reveals approximately 2µm-wide regions dopamine release hotspots, identified by sharp changes in $\Delta F/F$ fluorescence[9]. Recent studies using similar dopamine nanosensors within 2-D films have shown that these dopamine hotspots emerge from tyrosine hydroxylase (TH) positive axonal varicosities and co-localize with the pre-synaptic scaffolding protein Bassoon[120;121]. As such, we identified the average number of dopamine hotspots active within a slice during stimulation (slice average hotspot number) as well as the peak amount of dopamine released from the average hotspot within the slice (slice average peak $\Delta F/F$) as key metrics in characterizing dopamine release dynamics.

We first examined nIRCat imaged dopamine release in R6/2 HD and WT mice at 4 weeks, 9 weeks, and 12 weeks in response to a single 0.3 mA, 1 ms electrical pulse. WT mice showed consistent, robust performance on the rotarod across the 4 through 12 week time points. This was mirrored by WT dopamine release profiles, with WT slices showing similar numbers of dopamine hotspots through 4 to 12 weeks (Fig.3.2b). In contrast, R6/2 HD mice show show a significantly decreased number of dopamine hotspots at 12 weeks when disease progression is most severe disease in comparison to the WT counterparts. These results suggest that the number of active dopamine release sites in response to electrical stimulation may be decreased late in HD.

We next examined the trends in mean peak dopamine $\Delta F/F$ and similarly found that the average strength of dopamine release at an active dopamine hotspot was significantly decreased in R6/2 HD slices at the most severe disease time point at 12 weeks in comparison to their WT counterparts (Fig.3.2c). This suggests that late in disease dopamine release from individual dopamine hotspots is also affected, contributing to overall decreases in dopamine tone and response. These observed decreases in dopamine hotspot number and dopamine hotspot performance within R6/2 HD mice from 4 to 12 weeks are consistent with established dopamine trends from R6/2 dopamine literature which show through parallel methods of microdialysis and FSCV that dopamine release capacity decreases with disease progression[60;62;116;117]. Notably, nIRCat's increased spatial resolution allows new insights into the way dopamine release is compromised. These results indicate that decreased dopamine tone and release in the late R6/2 HD disease state is driven by a combination of both dopamine hotspot loss and dopamine hotspot dysfunction. Interestingly, at 4 weeks and 9 weeks there

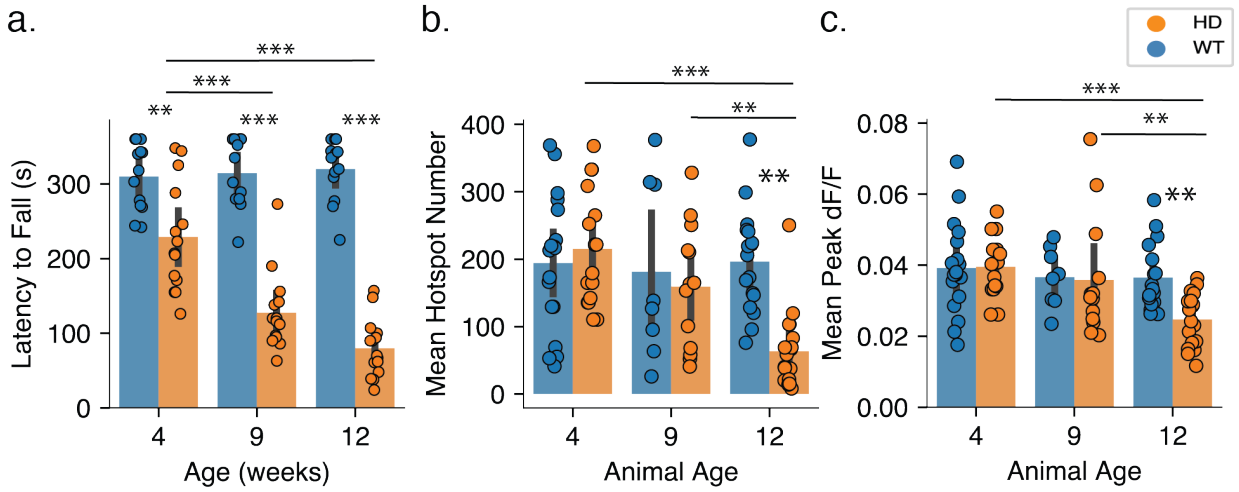

Figure 3.2: R6/2 HD mice show progressive decrease in number of dopamine hotspots over disease progression but not a change in individual dopamine ΔF/F hotspot response a. R6/2 HD mice show progressive decrease in latency to fall during an accelerating rotarod behavioral task (WT N = 13 animals, HD N = 14 animals; ANOVA: disease state, p =¡ 0.0005 age, p =¡ 0.0005 ; interaction, p =¡ 0.0005; pairwise t-test: *** p =¡ 0.0005 4 wk HD/ 12 wk HD, *** p =¡ 9 wk HD/12 wk HD, ns p = 0.8105 and p = 0.7531 4 wk WT/ 12 wk WT and 9 wk WT/ 12 wk WT; ** p = 0.0020 4 wk HD/4 wk WT; *** p ¡ 0.0005 9 wk HD/9 wk WT; *** p ¡ 0.0005 12 wk HD/12 wk WT) b. R6/2 HD mice show progressively decreasing numbers of dopamine hotspots from 4 weeks through 9 and 12 weeks while WT mice show no changes in dopamine hotspot number with age. (4 weeks WT N = 18 animals, HD N = 18 animals; 9 weeks WT N = 10 animals, HD N = 13 animals; 12 weeks WT N = 18 animals, HD N = 18 animals; ANOVA: disease state, p = 0.0101; animal age, p = 0.0034 ; interaction, p = 0.0018; pairwise t-test: *** p ¡ 0.0005 12wk/HD compared to 4wk/HD, ** p =0.0037 12wk/HD compared to 9wk/HD, * p ¡ 0.0005 12wk/HD compared to 12wk/WT). c. R6/2 HD mice show no change in average peak ΔF/F at 4 and 9 weeks but show significant decrease late in disease at 12 weeks. (ANOVA: disease state, p = 0.0469; animal age, p = 0.0047 ; interaction, p = 0.0530; pairwise t-test: *** p ¡ 0.0005 12wk/HD compared to 4wk/HD, *** p ¡ 0.0005 12wk/HD compared to 12wk/WT).

is no significant difference in the number of dopamine hotspots between R6/2 HD slices and their WT counterparts despite recorded difference between rotarod performance. These findings suggest that changes in motor ability seen at 4 and 9 weeks are not primarily driven by decreases in dopamine release. Rather, motor deficits may arise from downstream dopamine signaling or altered signaling from other synapses such as glutamatergic inputs from the cortex.

3.3.3 Changes in R6/2 Dopamine Release 0.1 mA

The amount of dopamine released upon stimulation is correlated to the strength of stimulation. Previous studies have shown that dopamine release deficits in R6/2 HD mice are

most pronounced a high stimulation strengths[60]. We sought to see if lower stimulation intensity at 0.1 mA would resolve the difference in dopamine release observed during 0.3 mA stimulation. R6/2 HD slices showed decreased number of active dopamine hotspots at the severe disease time point at 12 weeks in comparison to their WT counterparts despite decreased stimulation intensity (Fig.3.3a). However, in contrast to the data collected for 0.3 mA stimulation intensity, the mean peak $\Delta F/F$ of dopamine hotspots active in R6/2 HD slices in response to 0.1 mA stimulation were equivalent to those measured for the WT counterparts (Fig.3.3b). These findings suggest that HD driven changes in the dopamine release machinery of dopamine hotspots may only be apparent during events that require large dopamine release. In contrast, differences in the ability of R6/2 HD slices to activate dopamine hotspots late in disease may be apparent during all dopamine release events.

3.4 Conclusions

In this work we investigate spatial changes in dopamine release over the course of disease in R6/2 Huntington's Disease model mice using nIRCat nanosensors. The synaptic-scale spatial resolution of these dopamine sensors enables identification of dopamine hotspots that are activated by electrical stimulation via tungsten electrode and sensitive to stimulation intensity. In this work we introduce and apply an analytical framework for the intepretation of nIRCat imaging data within a biological context to elucidate dopamine release dynamics. These analyses show that progressive decreases in R6/2 HD dopamine release are driven by both decreases in dopamine hotspot number and individual release site performance.

Disrupted dopamine transmission during Huntington's Disease has been well documented in both HD patients and many genetic mouse models. In particular, the R6/2 mouse model has been noted to exhibit progressive decreases in dopamine release and basal tone using bulk dopamine measurement tools such as FSCV and microdialysis[60;61;62;116;117]. Herein with nIRCat, we find that 12 week old HD mice release only 23% of WT dopamine levels, in alignment with levels previously reported in existing R6/2 dopamine literature (Fig.3.4)[62;116]. Notably, our spatial insights from nIRCat imaging allow this late disease state to be interrogated at the level of release sites, revealing that decreases in overall dopamine release are primarily driven by a decrease in the number of dopamine hotspots rather than decreased individual hotspot performance. These differences may be particularly pronounced during events requiring large amounts of dopamine release, as R6/2 HD and WT slices show similar peak $\Delta F/F$ when stimulated at lower intensities. The persistent deficit in active dopamine hotspot number in R6/2 HD mice at both high and low stimulation intensities late in disease suggests that the number of dopamine hotspots capable of dopamine release may be compromised. This may occur through mechanisms that interfere with the dopamine release machinery at dopamine release sites, functionally silencing the hotspots, or through physical degeneration of the axonal arbors.

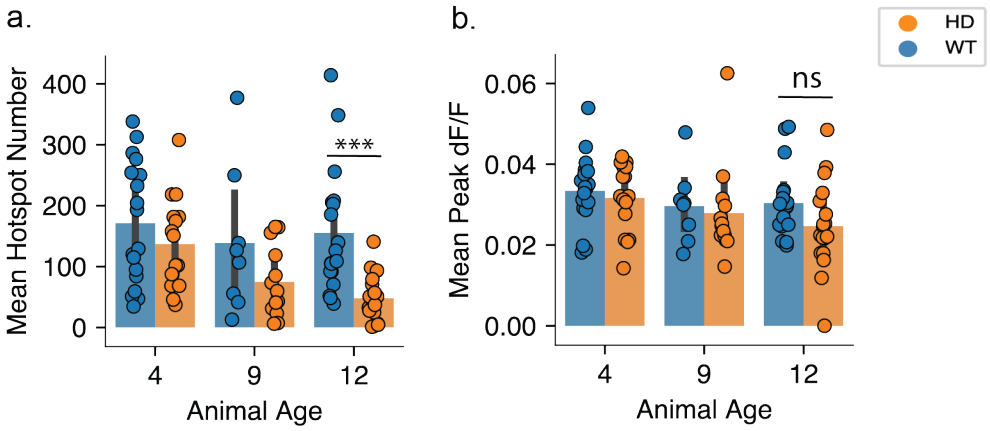

Figure 3.3: R6/2 HD mice show comparable individual dopamine ΔF/F hotspot response to their WT counterparts at low stimulation intensity and decreased dopamine hotspot number late in disease A, R6/2 HD brain slices show progressively decreasing numbers of dopamine hotspots from 4 weeks through 9 and 12 weeks when stimulated at 0.1 mA while WT mice show no changes in dopamine hotspot number with age. (4 weeks WT N = 18 animals, HD N = 18 animals; 9 weeks WT N = 10 animals, HD N = 13 animals; 12 weeks WT N = 18 animals, HD N = 18 animals; ANOVA: disease state, p = 0.106; animal age, p = 0.1013 ; interaction, p = 0.6419; pairwise t-test: ns p = 0.0921 12wk/HD compared to 12wk/WT, ns p = 0.1969 9wk/HD compared to 9wk/WT, ns p =0.2627 4wk/HD compared to 4wk/WT). B, R6/2 HD brain slices show no change in average peak dopamine ΔF/F at 4 and 9 weeks when stimulated at 0.1 mA but show significant decrease late in disease at 12 weeks. (4 weeks WT N = 18 animals, HD N = 18 animals; 9 weeks WT N = 10 animals, HD N = 13 animals; 12 weeks WT N = 18 animals, HD N = 18 animals; ANOVA: disease state, p ¡= 0.0005; animal age, p = 0.0309 ; interaction, p = 0.1982; pairwise t-test: *** p ¡ 0.0005 12wk/HD compared to 12wk/WT, ns p = 0.1969 9wk/HD compared to 9wk/WT, ns p =0.2627 4wk/HD compared to 4wk/WT).

Computational modeling of phasic and tonic dopamine release has indicated that activation of D1-receptors and D2-receptors is complex and reliant on "spheres of influence" rising from each dopamine releasing terminal[68;122]. Our findings indicate that the sphere of influence of dopamine terminals in late HD is undermined not only through decreased dopamine release at individual hotspots, but also by decreased coverage across the dorsal lateral striatum due to loss of active hotspots. This decrease in dopamine coverage in the form of number of spheres and size of spheres across the dorsal lateral striatum may underlie the altered dopamine signaling to dopamine receptors on direct pathway D1-MSNs, pathway D2-MSNs, and glutamatergic cortico-striatal glutamate terminals[51;52;63;123;124]Lastly, we demonstrated in this work that nIRCat's expression-free labeling system allows investigation of dopamine release profiles in animals as young as 4 weeks of age. Previous work studying dopamine release in R6/2 HD mice studied change in locomotor activity and dopamine release beginning at 6 weeks of age. To our knowledge, this work represents the earliest measured timepoint of R6/2 dopamine release at 4 weeks. Expression-free labeling allows access to not only younger age points but also degenerated brain tissue, which may show altered expression of genetically-encoded tools that impairs direct comparison between HD and WT conditions.

a.

DA Detection Method	R6/2 HD DA release (% of WT DA release)		
	4 wk	9 wk	12 wk
nIRCat Imaging (Hotspot Number x peak ΔF/F)	~100%	~84%	~23%
Fast Scan Cyclic Voltammetry†		~60%	~26%
Microdialysis††		~43%	~23%

b.

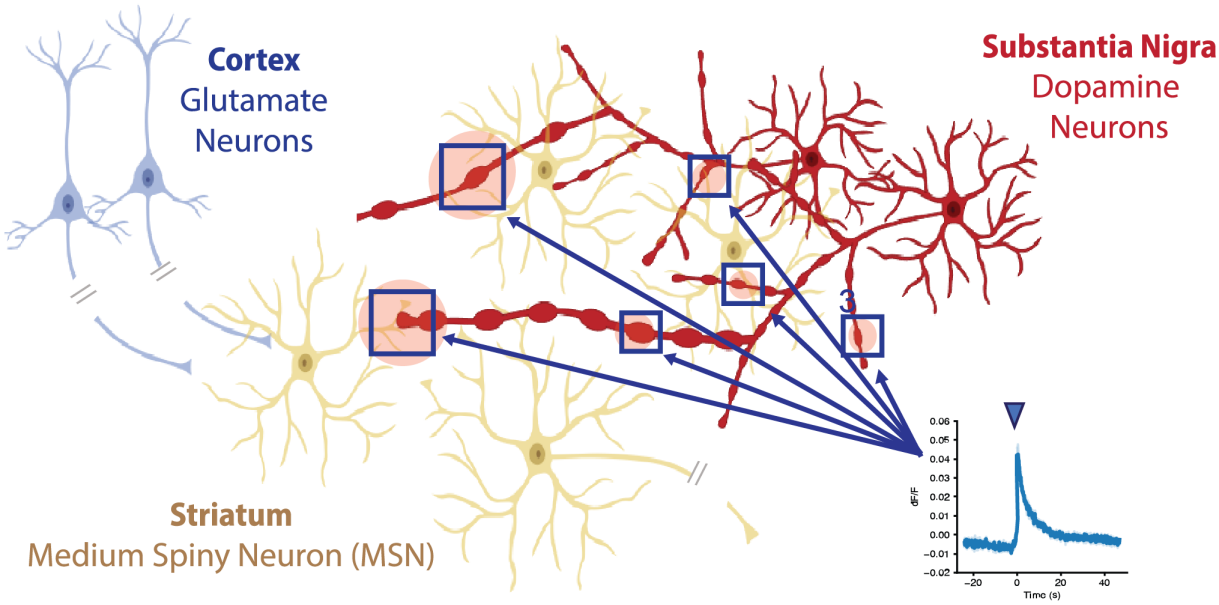

Figure 3.4: nIRCat measured reductions in dopamine release in R6/2 HD mice are comparable to measurements previously measured using FSCV and microdialysis
A. Amount of dopamine released in HD animals as a percentage of WT values was calculated via the equation (WT Hotspot Number x WT mean peak ΔF/F) / (HD Hotspot Number x HD mean peak ΔF/F). These values can be compared to values previously reported in literature. † (Johnson et al., 2006) † † (Callahan and Abercrombie, 2011) B. Diagram of how dopamine hotspot number and mean peak ΔF/F contribute to dopamine signaling across the striatum. Red circles around dopamine boutons denote dopamine release and blue squares represent identified hotspots. Dopamine release and reuptake traces are averages from all hotspots to calculate the mean peak ΔF/F denoted by the blue triangle.

Altogether, this work highlights the utility of nIRCat for elucidating dopamine dynamics in HD. Imaging with nIRCat allows expression-free access of a wide range of time points and deeper spatial insights into how dopamine is mobilized across the striatum. These new spatial insights complement previous work exploring in the role of dopamine in HD and motivat deeper exploration into the events that drive dopamine hotspot loss and dysfunction.

3.5 Materials and Methods

3.5.1 Animals

Male B6CBA-Tg(HDexon1)62Gpb/3J mice (R6/2 mice) were purchased from Jackson Labs and bred at 6 weeks with 10 week old female C57BL/6 mice. Pups were weaned and genotyped for the human HD fragment at 3 weeks. Mice were housed at three to five animals per cage with food and water available ad libitum and maintained in a temperature-controlled environment on a 12h dark/light cycle with light-on at 7:00 am and light-off at 7:00 pm. All animal procedures were approved by the University of California Berkeley Animal Care and Use Committee.

3.5.2 nIRCat Nanosensor synthesis and characterization

Dopamine nIRCat nanosensor was synthesized and characterized as described previously described in (Yang et al., 2021). A single walled carbon nanotube (SWNT) slurry was created by combining 1050 mg of hydrated HiPco SWNTs purchased from NanoIntegris with 25 mL of molecular grade water in a 50 mL Falcon Tube and probe sonicating the solution for 2 minutes at 10% amplitude until the slurry is visually distributed. To create nIRCat nanosensors, 100 µl of SWNT slurry was mixed with 1 mg of (GT)6 oligonucleotides purchased from Integrated DNA Technologies (standard desalting) in 100 mM and bath sonicated for 10 minutes (Branson Ultrasonic 1800) followed by 5 minutes of rest at room temperature. The solution was then sonicated on ice for 10 minutes using a probe-tip sonicator (Cole-Parmer Ultrasonic Processor, 3-mm diameter tip, 5 W power) followed by 5 minutes of rest on ice. The sonicated solution was incubated at room temperature for 30 mins and centrifuged at 16,000 g (Eppendorf 5418) for 30 minutes to removed unsuspended SWNT bundles and amorphous carbon. The supernatant is the removed for use and stored at 4°C C for 30 minutes before characterization. Final supernatant should be stored at 4°C until use.

Nanosensors are synthesized in 1 mL batches and combined for characterization. Nanosensor concentrations were determined using absorbance at 632 nM with an extinction coefficient of 0.036 (mg/L)-1cm-1. To characterize the visible and nIR absorption spectrum, nanosensors were diluted to a concentration of 5 mg/L in 1x PBA and taken using a UV-VIS-nIRC spectrophotometer (Shimadzu UV-3600 Plus). To test fluorescent response to dopamine administration, each sensor batch is diluted to a working concentration of 5 mg/L in 1x PBS and 198 µl aliquots are made into a 96-well plate and baseline fluorescence is taken using a 20x objective on an inverted Zeiss microscope (Axio Observer D1) coupled to a Princeton Instruments spectrograph (SCT 320) and a liquid nitrogen cooled Princeton Instruments InCaAs linear array detector (PyLoN-IR). Nanosensors were excited using a 721-nm lazer (Opto Engine LLC). After the baseline fluorescence was taken, 2 µl of 10 mM Dopamine in 1xPBS is added and a robust fluorescence response to dopamine was confirmed.

3.5.3 Phenotypic Motor Coordination Assessment

The accelerating Rotarod test and hind limb clasp test were used to evaluate changes in motor coordination in R6/2 and WT mice. For accelerating rotarod tests, mice were placed on a Ugo Basile rotarod for 1 min a 5 rpm to adjust to the apparatus. At the end of the 1 min adjustment period, the speed of the rotarod was increased at a constant rate to a final speed of 40 rpm over 350 s. The trial is terminated after mice either fall off the rod, tumble on the rod for two consecutive rotations, or "max out" the rod speed at 360s. Starting at four weeks, mice are introduced to the rotarod and complete the test for 3 consecutive days, before their rotarod times plateau and performance is recorded on the fourth day. For subsequent weeks, mice complete the rotarod only once a week.

Hind limb clasp tests are conducted by grasping mice at the base of the tail and lifting the mouse off the ground for 10 s. Mice that show splayed out legs are assigned a score of 0, mice that contract one hindlimb are scored at 1, mice contract both hindlimbs are scored at 2, and mice that retract both hindlimbs full and curl into the abdomen are scored at 3.

3.5.4 nIRCat dopamine Imaging

Acute live brain slices were prepared using protocols previously described (Yang et al., 2021). Briefly, mice are deeply anesthetized via intraperitoneal ketamine/xylazine cocktail and perfused transcardially using cold cutting buffer (119 mM NaCl, 26.2 mM NaHCO3, 2.5 mM KCl, 1 mM NaH2PO4,3.5 mM MgCl2, 10 mM glucose, and 0 mM CaCl2). The brain was then rapidly dissected, mounted on a vibratome stage (Leica VT1200 S) using super glue, and cut into 300 µm thick slices containing the dorsal striatum. Slices were then collected and incubated at 37°C for 30 minutes in oxygen saturated ACSF (119 mM NaCl, 26.2 mM NaHCO3, 2.5 mM KCl, 1 mM NaH2PO4, 1.3 mM MgCl2, 10 mM glucose, and 2 mM CaCl2) followed by 30-minute incubation at room temperature. All slices are maintained at room temperature until imaging and used within 6 hours of preparation.

Slices are labeled through passive incubation in 5 ml of ACSF containing nIRCat nanosensor at a concentration of 2 mg/L for 15 minutes. After incubation, the slices is transferred through 3 wells of a 24-well plate containing ACSF to rinse off non-localized nIRCat sensor and then left to rest at room temperature ACSF for 15 minutes before transfer to the 32°C recording chamber. Once placed in the recording chamber, slices equilibrate for 15 minutes during which a tungsten bipolar stimulation electrode is positioned at a field of view in the dorsal-lateral striatum using a 4x objective (Olympus XLFluor 4/ 340). Under a 60x objective the electrode is moved 200 µm away from the selected field of view and brought into contact with the surface of the brain slice. In all experiments, 600 total images are acquired into an image-stack at a rate of 9 frames per second. A single stimulation of 0.1 mA or 0.3 mA is applied after 200 frames of baseline are collected. Videos of stimulation at each strength are collected in triplicate and stimulation strengths are alternated. All slices are given 5 minutes between each stimulation with the excitation laser path shuttered. Prior

to stimulation, the laser is un-shuttered for 1 minutes.

3.5.5 Image Stack Processing and Data Analysis of nIRCat Data

Raw Image stack files are processed using a custom-built, publicly available MATLAB program (https://github.com/jtdbod/Nanosensor-Imaging-App). Image processing procedures are described in depth in Yang, del Bonis O'Donnel et al and briefly summarized here. Regions of dopamine release are identified by large changes in nIRCat $\Delta F/F$ response. To minimize bias and improve stack processing time, regions of high $\Delta F/F$ response (dopamine hotspots) were identified by defining a grid of 2 µm squares across the field of view. For each grid square $\Delta F/F$ was calculated using the formula (F- F0) /F0, where F0 is defined by the average fluorescence of the grid square over the first 30 frames of the image stack and F is the fluorescence intensity of the gird square as it changes over the 600 collected frames. Grid squares are identified as regions of interest if they exhibit behavior that is 3 standard deviations above the baseline F0 activity around time of stimulation (200 frames).

Dopamine hotspots were identified for each stimulation replicate image stack taken at a given field-of-view on a brain slice. The peak $\Delta F/F$ of each dopamine hotspot in the image stack were averaged to give the average image stack peak $\Delta F/F$. The average image stack peak $\Delta F/F$ from the three stimulation replicates were then average to give the slice average peak $\Delta F/F$. Similarly, the number of dopamine hotspots identified from each stimulation replicate image stack were averaged to give the slice average hotspot number. Mean dopamine release and reuptake traces are produced by averaging the average traces from each slice (3 stimulations per slice, 1 slice per animal). Percent change in hotspots was calculated as (number hotspots wash - number hotspots 2 mM Ca^{+2})/ (number hotspots 2 mM Ca^{+2}), whereas change in hotspots number was calculated as (number hotspots wash - number hotspots 2 mM Ca^{+2}).

To track hotspot fidelity, each initially defined grid square was assigned a unique position number, allowing the position of each identified dopamine hotspot within an image stack to be recorded. For a set of triplicate image stacks, an array of all unique hotspots active across the stimulation replicates was generated. Then python code was used to analyze whether each unique hotspot was active in each stimulation replicate. The number of stimulations a unique hotspot was active in was summed across the three replicates and assigned as the dopamine release fidelity (e.g. hotspot '12' is active in 2 out of 3 stimulations and is assigned release fidelity 2). The same procedure was used to identify the dopamine release fidelity of hotspots active after drug wash. Hotspots were then separated into three groups: hotspots that are active both before and after drug wash (shared hotspots), hotspots that become active after drug wash (added hotspots), and hotspots that are only active before drug wash. For shared hotspots modulation in hotspot release strength was calculated as the difference in peak $\Delta F/F$ of the unique hotspot before and after drug wash, (mean $\Delta F/F$)post - (mean $\Delta F/F$)pre , where (mean $\Delta F/F$)pre is the average peak $\Delta F/F$ of each unique dopamine hotspot across the three stimulations before drug wash and (mean $\Delta F/F$)post is the average

peak ΔF/F of each unique dopamine hotspot across the three stimulations after drug wash. For hotspots active only after drug wash, there is no corresponding "pre drug wash" ΔF/F. Therefore, the difference in peak ΔF/F was calculated through (mean ΔF/F)post - (mean ΔF/F)pre, shared, where (mean ΔF/F)post represents the average peak ΔF/F of the unique dopamine hotspot active after sulpiride wash across three stimulations and (mean ΔF/F)pre, shared is the average of all the shared hotspots' mean ΔF/F from the slice before drug wash.

3.5.6 Exerimental Design and Statistical Analysis

All nIRCat Imaging data were processed using a custom-built, publicly available MATLAB program (https://github.com/jtdbod/Nanosensor-Imaging-App). Statistical analyses were conducted using the open-source statistical python package pingouin. All bar graphs show the mean with error bars denoting the 95% confidence interval. All single data points correspond to a single slice taken from an animal. Data comparing two variables was analyzed using a mixed-ANOVA with wash condition as the within-subject factor (e.g.sulpiride, blank, calcium concentration) and disease state as the between-subject factor (eg. HD, WT). Paired t-tests were used a post-hoc tests if mixed-ANOVA analyses indicated significant differences. Data comparing two values of one variable were analyzed using tukey's t-test. Group sizes were determined based on previous literature (Adil et al., 2018). Changes in histogram skew were computed through pooling of all hotspots identified across all mice within the disease and wash condition and evaluated using a permutation test using the test statistic μ = skew(post wash) – skew(pre-wash).

Chapter 4

Measurement of Calcium Dependent Dopamine release in R6/2 Huntington's Disease Model Mice using nIRCat Imaging[iv]

[iv]This section is produced in part with permission from the following work: Yang, S. J., et al. "Synaptic scale dopamine disruption in Huntington's Disease model mice imaged with near-infrared catecholamine nanosensors."

4.1 Abstract

Entry of extracellular calcium entry into presynaptic boutons plays a critical in the release of multiple signaling molecules in the brain including glutamate, GABA, Acetylcholine. Specifically, the size of calcium influx into the presynapse can shapes the extent of neurotransmitter release through modulation of the number of active release sites and the number of released vesicles. While striatal dopamine release has been long understood to be calcium dependent, identification of the exact molecular machinery recruited for this process has only been recently accomplished. These studies have shown that a portion of doapmine release occurs through the mobilization of fast-release machinery via the active zone scaffolding protein RIM and the calcium sensor synaptotagmin-1. To date, studies of fast, calcium-dependent dopamine release have utilized Fast Scan Cyclic Voltammetry (FSCV) to provide spatially averaged release from regions within the striatum. In this work we establish a method to use nIRCat imaging in conjunction with a extracellular Ca^{+2} wash experimental framework to investigate calcium-dependent dopamine release at high spatial resolution. We demonstrate that this method can be used to examine the extracellular calcium dependence of dopamine release in WT R6/2 and HD R6/2 mice at early (4 week) and late (12 week) time points of disease progression. Compellingly, we find that R6/2 HD slices early in disease exhibit increased modulation of dopamine hotspot release at high extracellular Ca^{+2} concentrations and R6/2 HD slices late in disease add a similar number of dopamine hotspots at high extracellular Ca^{+2} concentrations to their WT counterparts despite significant neurodegeneration. These findings stand in contrast to previous FSCV studies in R6/2 mice, underscoring the importance and utility of the spatial insights afforded by nIRCat imaging in the study of neurodegeneration.

4.2 Introduction

Calcium entry into the presynaptic terminal is a critical trigger for the fusion of neurotransmitter and neuromodulator containing synaptic vesicles[125;126]. Calcium enters the presynaptic terminal via voltage-gated Ca^{+2} channels, which open in response to the voltage change initiated by the arrival of an action potential or electrical stimulation. Within the presynaptic terminal, calcium displays a fourth-order cooperativity with neurotransmitter release, which is facilitated by the "calcium-sensor" synaptotagmin[127;128]. Activation of synaptotagmin in turn facilitates the fusions of synaptic vesicles with the presynaptic membrane via the interactions of SNAREs (for soluble N-ethylmaleimide–sensitive factor (NSF)-attachment protein receptors) and SM proteins (for Sec1/Munc18-like proteins), ultimately resulting in the release of signaling molecules into the extracellular space (Fig.4.1a)[125].

Striatal dopamine release has been well understood to occur in a calcium dependent manner[129]. However, it is only in the last five years that the field has begun to identify the specific molecular machinery employed during this release process. Structural studies utilizing 3D-SIM super-resolution microscopy have shown that a portion of dopamine release

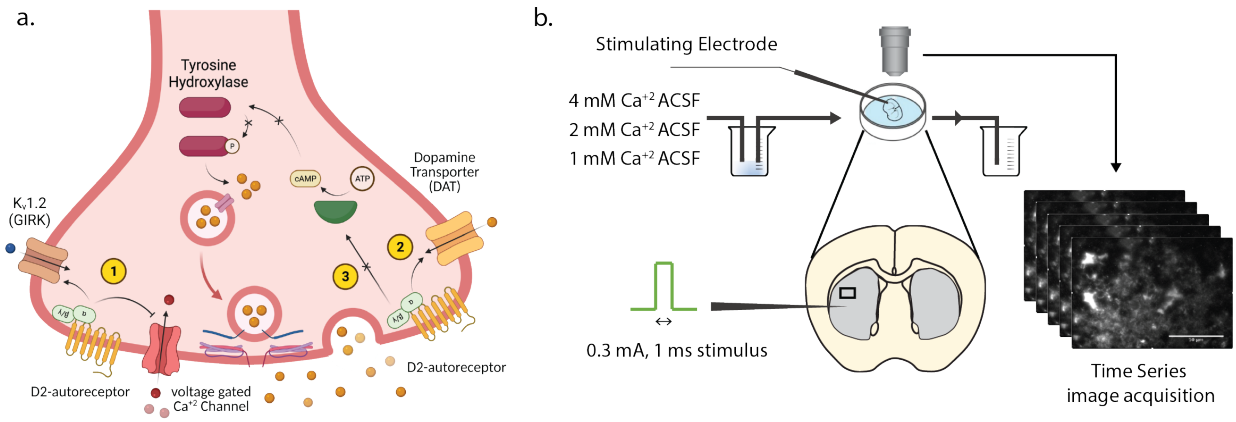

Figure 4.1: Experimental framework for measuring calcium dependence of dopamine release using nIRCat Imaging A. Diagram of molecular machinery involved in the packaging and release of dopamine vesicles for release. B. Experimental set up for substituting artificial cerebral spinal fluid at different calcium concentrations while recording dopamine release using nIRCat imaging

relies on the active zone scaffolding protein RIM, which tethers presynaptic voltage-gated Ca^{+2} channels to active zones within the dopamine bouton where dopamine release occurs[65]. Approximately 30 % of striatal dopamine varicosities within the striatum contain the active zone scaffolding proteins bassoon, RIM, and ELKs, and conditional knock out of RIM disrupts presynaptic scaffolding and abolishes dopamine release[65]. These discoveries indicate that striatal dopamine varicosities have the machinery needed to undergo fast, targeted dopamine release and draw into question classical arguments that dopamine release occurs through slow, unspecialized volume transmission. In complement, functional studies utilizing fast scan cyclic voltammetry (FSCV) have identified synaptotagmin-1 as the Ca^{+2} sensor responsible for fast-striatal dopamine release from these scaffolded varicosities[67]. Knockout of synaptotagmin-1 in mice abolishes electrically stimulated dopamine release, though spontaneous dopamine release in the presence of TTX is still detected. This asynchronous release of dopamine may be achieved through the actions of slower synaptotagmins, such as synaptotagmin-7, which are also present in striatal dopamine neurons.[67]. Together these studies have provided new grounds for exploration into how striatal dopamine release occurs at the level of single dopamine varicosities.

Calcium dependence of neurotransmitter and neuromodulator release is commonly explored *ex vivo* in acute brain slice through varying the extracellular Ca^{+2} Concentration. Physiological calcium concentration has been reported to sit at 1.5 mM Ca^{+2}., though standard preparations of artificial cerebral spinal fluid for ex vivo brain slice work are for 2 mM Ca^{+2} and are typically varied from 1 mM Ca^{+2} through 4 mM Ca^{+2}. This experimental framework was most recently employed in conjunction with carbon fiber amperometry to study electrically and optogenetically stimulated dopamine release profiles change with extracellular calcium concentration[67;130;131] (Fig.4.1b). These experiments have shown that synchronous striatal dopamine release is not only calcium dependent, but also increases linearly with

extracellular calcium concentration between 0.5 mM and 2 mM Ca^{+2}. However, the low spatial resolution of carbon fiber amperometry is unable to provide further insight into how increasing extracellular calcium concentration affects individual boutons. Leitz et al. address this spatial resolution challenge in glutamatergic hippocampal neurons by visualizing single synaptic vesicle mobilization at individual glutamatergic boutons through lentiviral expression of Vglut1-pHluorin. This data set obtained from pHluorin imaging shows that increasing extracellular calcium concentration increases glutamate release by increasing the release probability of active glutamatergic release sites and recruiting less-active boutons to higher releasing states[132]. As such, increases in glutamate release at high calcium concentrations are the result of

In this work we use nIRCat imaging as an analogous high spatial resolution imaging tool to investigate the effect of extracellular calcium concentration on single dopamine release sites. Previous studies have been performed using nIRCat imaging and a Ca^{+2} concentration wash experimental framework to study calcium-dependent dopamine release in the dorsal medial striatum (DMS)[9]. As such, nIRCat has been established to perform robustly and comparably across 0 mM to 4 mM Ca^{+2}. We expand upon this work by examining dopamine release in the dorsal lateral striatum (DLS) and implementing a new method of quantifying dopamine hotspots number and performance. Furthermore, we explore how the calcium dependence of striatal dopamine release changes over the course of Huntington's disease. Studies employing FSCV has shown that at 12 weeks of age, both WT and R6/2 HD mice show equivalent modulation in dopamine release in response to extracellular calcium concentration[117]. This occurs despite an overall decrease in dopamine release in R6/2 HD mice at 12 weeks, suggesting that compromised dopamine release is not the result of altered calcium machinery. In contrast to this finding, disrupted calcium signaling through endoplasmic reticulum stores or N-methyl-D-aspartate receptors (NMDARs) has been noted across multiple disease models of Huntington's Disease[52]. Curiously, current studies into R6/1 and R6/2 HD mouse lines have been noted not to recapitulate aberrant NMDAR Ca^{+2} signaling and subsequent excitotoxicity, a departure from observation of parallel HD. To this end, we utilize nIRCat imaging to study how dopamine hotspot number and mean peak $\Delta F/F$ change in WT and Huntington's Disease animals early (4 weeks) and late (12.5 weeks) in disease, allowing for a more spatially rich depiction of how calcium dependent dopamine release is affected in R6/2 WT and R6/2 HD mice.

4.3 Results and Discussion

4.3.1 Effect of Extracellular Ca^{+2} Concentration on Dopamine Hotspots in R6/2 WT Mice

We first sought to characterize how dopamine hotspots in R6/2 WT slices change in number and peak $\Delta F/F$ with extracellular Ca^{+2} concentration in R6/2 WT mice. Acute striatal brain slices were prepared from WT R6/2 mice at 4 weeks and 12 weeks and incubated with

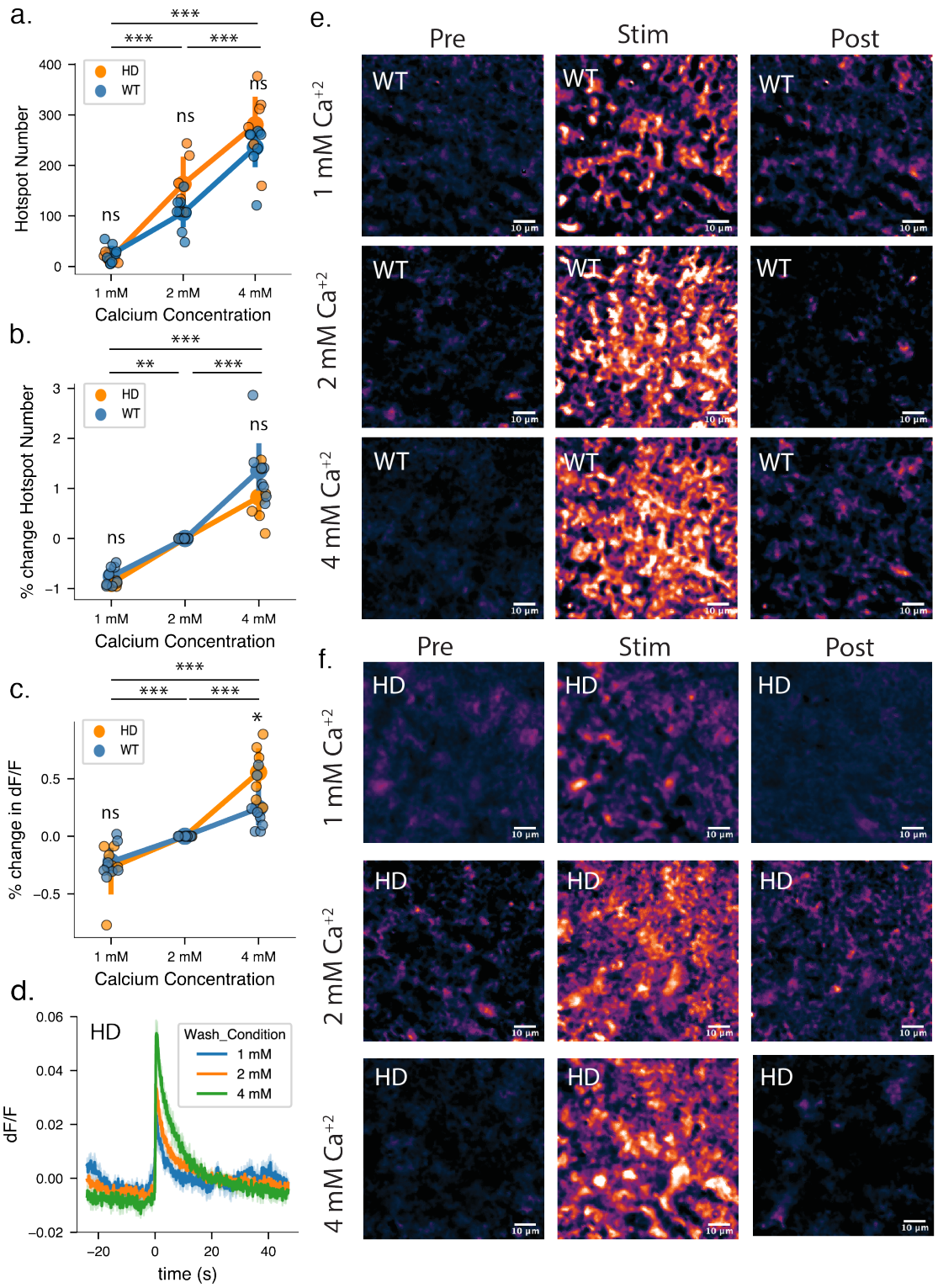

Figure 4.2: WT and R6/2 HD mice show similar extracellular calcium sensitivity for dopamine release at 4 weeks A. The average number of dopamine hotspots active in 4 week WT and R6/2 HD striatal brain slices in response to 0.3 mA stimulation is comparable at 1 mM Ca^{+2}, 2 mM Ca^{+2} and 4 mM Ca^{+2} (WT N = 9 slices, 6 animals, HD N = 6 slices, 6 animals; mixed-ANOVA: disease state, p = 0.10715; wash condition, p ¡ 0.0005 ; interaction, p = 0.0735;. (Continued on the following page.)

Figure 4.2: (Continued from previous page) pairwise t-test: *** p ¡ 0.0005 4mM Ca^{+2} compared with 1 mM Ca^{+2}, *** p ¡ 0.0005 4mM Ca^{+2} compared with 2 mM Ca^{+2}, *** p ¡ 0.0005 2 mM Ca^{+2} compared with 1mM Ca^{+2}) B. The precent change in dopamine hotspots is also comparable at all calcium concentrations. (WT N = 9 slices, 6 animals, HD N = 6 slices, 6 animals; mixed-ANOVA: disease state, p = 0.0995; wash condition, p ¡ 0.0005 ; interaction, p = 0.1592; pairwise t-test: *** p ¡ 0.0005 4 mM Ca^{+2} compared with 1 mM Ca^{+2}, *** p ¡ 0.0005 4 mM Ca^{+2} compared with 1 mM Ca^{+2}, *** p ¡ 0.0005 Normal Ca^{+2} compared with Low Ca^{+2}). C. The percent increase in mean peak $\Delta F/F$ is comparable between WT and R6/2 HD striatal brain slice at 1 mM Ca^{+2} and 2 mM Ca^{+2}. At 4 mM Ca^{+2} R6/2 HD slices show a 31.3% elevated response compared to WT slices (mixed-ANOVA: disease state, p = 0.2468; wash condition, p ¡ 0.0005 ; interaction, p = 0.0057; pairwise t-test: *** p ¡ 0.0005 4 mM Ca^{+2} compared with 1 mM Ca^{+2}, *** p = 0.0002 4 mM Ca^{+2} compared with 2 mM Ca^{+2}, ** p = 0.0033 2 mM Ca^{+2} compared with 1mM Ca^{+2}; *p = 0.0070 High Ca^{+2}/HD compared with High Ca^{+2}/WT). D. Representative dopamine release and reuptake traces from imaged nIRCat-labeled brain slices for 4 week HD mice. Solid lines denote the average taken from all slices and light shaded bands represent one standard deviation from average behavior. A 1 ms, 0.3 mA stimulation is delivered at time = 0s. E. Representative images of dopamine release imaged in 4 week WT mice before, during, and after stimulated dopamine release. F. Representative images of dopamine release imaged in 4 week HD mice before, during, and after stimulated dopamine release.

nIRCat nanosensor. Labeled brain slices were then subject to a 0.3 mA, 1 ms electrical stimulus and while sitting in 1 mM Ca^{+2} (low Ca^{+2} ACSF), 2 mM Ca^{+2} (physiological Ca^{+2} ACSF), and 4 mM Ca^{+2} (High Ca^{+2} ACSF) (Fig.4.1b). At 4 weeks, the number of WT striatal dopamine hotspots increased with extracellular calcium concentration, with significantly more dopamine hotspots active at 4 mM Ca^{+2} than at 2 mM Ca^{+2}, and significantly fewer dopamine hotspots active at 1 mM Ca^{+2} than at 2 mM Ca^{+2} (Fig.4.2a,b). These findings support observations made in hippocampal glutamate neurons using pHluorin-tagged vesicles, showing that increasing extracellular Ca^{+2} concentration drives an increase in release probability and can recruit previously low activity boutons to active dopamine hotspots[132]. Similarly, at 4 weeks WT striatal dopamine hotspot peak $\Delta F/F$ showed a linear dependence on extracellular calcium concentration (Fig.4.2c, Fig.4.3c,). This increase is consistent with the expectation that increasing extracellular calcium concentration should drive and increase in multivesicular release from dopamine varicosities[126;132].

Given that increasing calcium concentration results in an increase in $\Delta F/F$ and dopamine hotspot number, our observed increase in dopamine hotspot number could be the result of increasing calcium concentration pushing low peak $\Delta F/F$ hotspots into nIRCat's range of detection. To investigate this further, we pooled all of the hotspots identified across 6 animals and plotted a histogram of hotspots across peak $\Delta F/F$. This analysis shows that at each extracellular calcium concentration, nIRCat imaging captures a full normal distribution of dopamine hotspots across peak $\Delta F/F$ (Fig.4.3a). These results indicate that the new dopamine hotspots that appear after increase extracellular calcium wash are likely newly active dopamine hotspots rather than previously active hotspots outside of nIRCat's range of detection.

We also examined calcium-dependent release dynamics in 12 week WT R6/2 mice and found no significant difference in calcium sensitivity of dopamine hotspots in comparison to 4 week R6/2 mice (Fig.4.4a). Interestingly the percent change in mean peak ΔF/F with extracellular calcium concentration appeared to change between 4 weeks and 12 weeks (Fig.4.2c, Fig.4.4c). Dopamine hotspots in 4 week animals showed a linear relationship between mean peak ΔF/F and calcium concentration from 1 mM Ca^{+2} to 4 mM Ca^{+2}. Conversely, dopamine hotspots in 12 week mice show a sharp increase in mean peak ΔF/F following 4 mM Ca^{+2} wash. This difference in response may suggest age or experience related alterations in extracellular calcium sensitivity in R6/2 mice. nIRCat's non-genetically encoded nature allows ready access of early age timepoints without expression time, making it an attractive candidate for the study of age-related changes. However, effective analysis of age-related changes would require a method of standardization between nIRCat imaging sessions to normalize for changes in sensor preparation or a timed breeding strategy allowing animals from two time points to be imaged in single sessions with the same nIRCat sensor preparation.

4.3.2 Early Calcium-dependent Disruptions in R6/2 HD Dopamine Hotspots

We next sought to examine whether the extracellular calcium sensitivity of dopamine hotspots differs between R6/2 HD and WT mice early in disease. To this end, we imaged stimulated dopamine release from nIRCat labeled R6/2 HD slices from 4 week animals at 4 mM Ca^{+2}, 2 mM Ca^{+2}, and 1 mM Ca^{+2}. We then examined the resulting changes in dopamine hotspot number and peak dopamine Δ F/F. Similar to WT R6/2 brain slices, increasing extracellular Ca^{+2} concentration from 2 mM Ca^{+2} to 4 mM Ca^{+2} drives increased number of dopamine hotspots in R6/2 HD brain slices while corresponding decrease to 1 mM Ca^{+2} results in fewer dopamine hotspots (Fig.4.2a). At all extracellular calcium concentrations there was no significant difference in the total number of dopamine hotspots active in R6/2 WT and HD brain slices or the percent increase of dopamine hotspots with increasing extracellular Ca^{+2} concentration (Fig.4.2b).

Interestingly, while 4 week R6/2 HD mice do show comparable percent increase in slice average peak dopamine Δ F/F to 4 week WT mice from 1 mM Ca^{+2} to 2 mM Ca^{+2}, 4 week R6/2 HD mice show significantly higher percent increase in slice average peak dopamine Δ F/F from 2 mM Ca^{+2} to 4 mM Ca^{+2} (Fig.4.2d, Fig.4.3e). This increased peak ΔF/F at 4 mM Ca^{+2} in R6/2 HD slices is visually apparent in plotted dopamine release and reuptake traces, which show greater modulation of peak ΔF/F in response to extracellular Ca^{+2} concentration within R6/2 HD slices in comparison to R6/2 WT slices (Fig.4.3c,d). Histograms showing the peak ΔF/F of dopamine hotspots pooled from all R6/2 HD and WT slices show that 4 week R6/2 HD and WT slices both show full normal distributions, suggesting that the observed increase in peak ΔF/F sensitivity in R6/2 HD mice does not account for the the increase in dopamine hotspots observed in R6/2 HD slices with changing extracellular Ca^{+2} concentration. A slight leftward shift in the distribution of peak dF/F histograms in WT slices is observed at high calcium concentrations, suggesting that at high

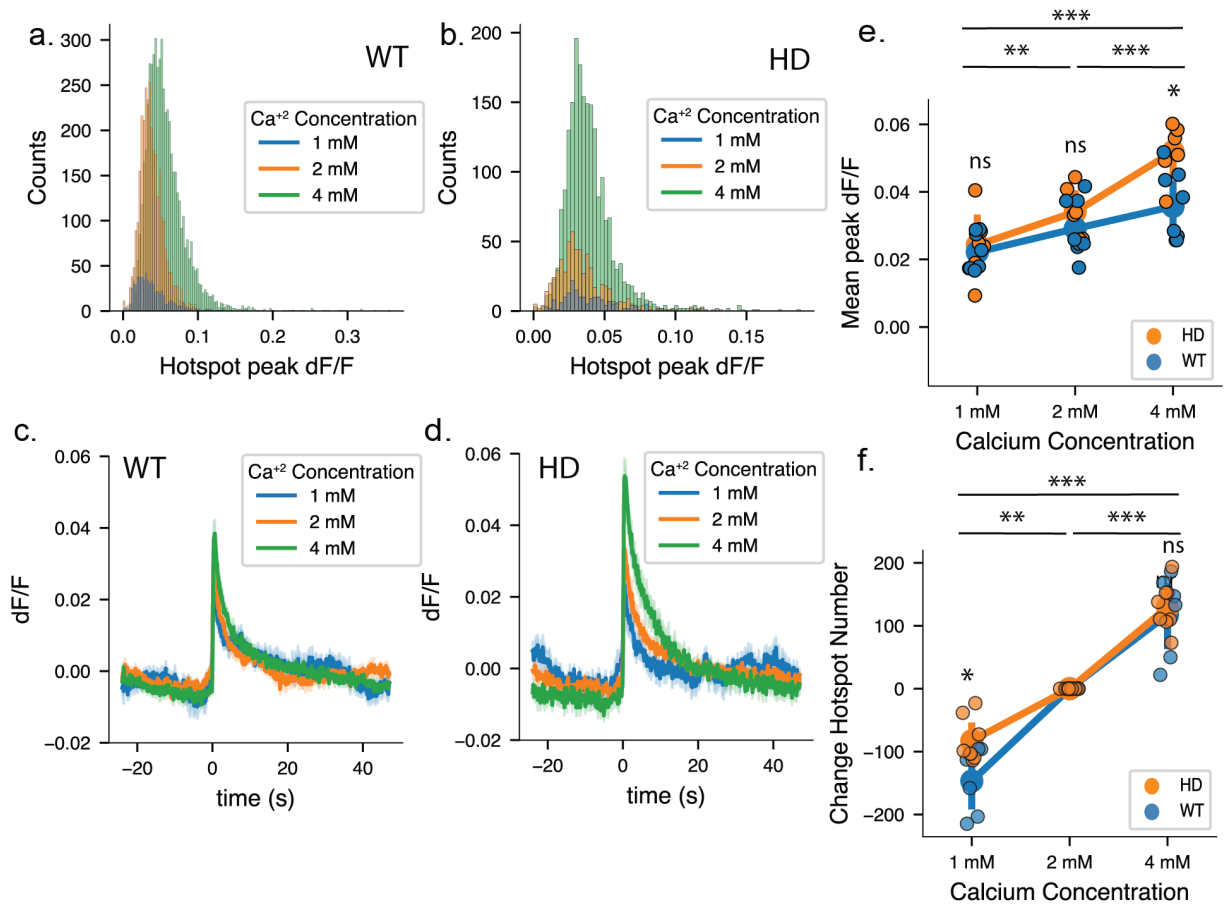

Figure 4.3: Pooled dopamine hotspot histograms and dopamine release and reuptake traces for 4 week R6/2 HD and WT mice A. Histograms of pooled dopamine hotspots from 4 week WT mice. Dark blue bars show hotspots active at 1 mM Ca^{+2}, orange bars hotspots active at 2 mM Ca^{+2}, and green bars hotspots active at 4 mM Ca^{+2}. B. Histograms of pooled dopamine hotspots from 4 week HD mice. C, Dopamine release and reuptake traces from imaged nIRCat-labeled brain slices for 4 week WT mice. Solid lines denote the average taken from all slices and light shaded bands represent one standard deviation from average behavior. A 1 ms, 0.3 mA stimulation is delivered at time = 0s D. Dopamine release and reuptake traces from imaged nIRCat-labeled brain slices for 4 week HD mice. E. The average mean peak $\Delta F/F$ values recorded in 4 week WT and HD slices at 1 mM Ca^{+2}, 2 mM Ca^{+2}, and 4 mM Ca^{+2} (mixed-ANOVA: disease state, *p = 0.1929; wash condition, *** p ¡ 0.0005; interaction, p = 0.0093; pairwise t-test: ** p = 0.007 HD/1 mM Ca^{+2} compared to WT/1 mM Ca^{+2}). F, Total change in hotspots number recorded in 4 week WT and HD slices at 1 mM Ca^{+2}, 2 mM Ca^{+2}, and 4 mM Ca^{+2} (mixed-ANOVA: disease state, *p = 0.0828; wash condition, *** p ¡ 0.0005; interaction, p = 0.735; pairwise t-test: ** p = 0.0338 HD/4 mM Ca^{+2} compared to WT/4 mM Ca^{+2}).

calcium concentrations in slices exhibiting robust dopamine release characteristics dopamine release intensity may be increased overall.

Observed increases in dopamine hotspots from calcium sensitivity early-symptomatic 4 week-old R6/2 HD mice may suggest alterations in calcium machinery early in HD progression that may contribute to later dysfunction. Our rotarod behavioral assay reported in Section3.3.1 indicates that at 4 weeks R6/2 HD mice already show decreased latency to fall over their 4 week WT counterparts. While nIRCat imaged dopamine release at physiological extracellular calcium concentration (2 mM Ca^{+2}) does not appear to be significantly different between 4 week WT R6/2 mice and 4 week R6/2 HD mice, it is possible that a latent disruption in dopamine release calcium machinery may contribute to this disruption in motor ability. Alternatively, it is possible that early changes in motor ability may result from disruptions in other motor circuits in the brain and are exacerbated by or directly drive alterations in dopamine signaling. Fully understanding the ramifications of this early difference in extracellular calcium concentration necessitates examination of a wider range of behavioral tests and molecular manipulations to directly target dopamine release calcium machinery.

4.3.3 Late Calcium-dependent Disruptions in R6/2 Dopamine Hotspots

We next investigated whether the extracellular calcium sensitivity of dopamine hotspots changes late in HD disease development. At 12 weeks, HD mice produce significantly fewer dopamine hotspots than WT mice at 2 mM Ca^{+2} and 4 mM Ca^{+2} (Fig.4.4a). As noted in Chapter 3, this decrease in hotspot number may be driven by physical loss of dopamine release sites over the course of neurodegeneration or functional silencing of dopamine release site due to alterations in dopamine release machinery. Decreasing extracellular calcium concentration to 1 mM Ca^{+2} suppresses the release probability of both WT and HD dopamine hotspots close to nIRCat's detection limit, consistent with Ca^{+2} release literature and previous nIRCat imaging findings in the dorsal medial striatum[9;132]. In contrast, increasing extracellular calcium concentration results in the activation of new, previously inactive hotspots 12 week HD slices, though this increase is not sufficient to rescue R6/2 HD levels to WT levels (Fig.4.3a). These findings indicate that there is some portion of dopamine hotspots in highly degenerated 12 week tissue that can be driven to release dopamine by stronger Ca^{+2} influx. Interestingly, though R6/2 HD slices show lower dopamine hotspot numbers than WT slices, R6/2 HD slices show a larger percent increase in hotspot number after 4 mM Ca^{+2} wash (Fig.4.3b). This dopamine hotspot increase appears to be driven by the fact that WT and HD slices add comparable amounts of dopamine hotspots after 4 mM Ca^{+2} despite the significantly lower number of dopamine hotspots initially present in HD slices at 2 mM Ca^{+2}(Fig.4.5e).

Increasing extracellular Ca^{+2} concentraton also modulates slice average peak dopamine Δ F/F in both R6/2 HD and WT slices (Fig.4.4c,d). In contrast to findings in 4 week mice, 12 week R6/2 HD mice show decreased overall mean peak Δ F/F in comparison to their WT counterparts at 4 mM Ca^{+2}, but do not show a significant difference in percent change in mean peak Δ F/F after wash on of 4 mM Ca^{+2} (Fig.4.4c, Fig.4.4e). These results suggest that a transition in the manner that Ca^{+2} modulates the release from dopamine hotspots may occur between 4 weeks and 12 weeks in R6/2 HD mice.

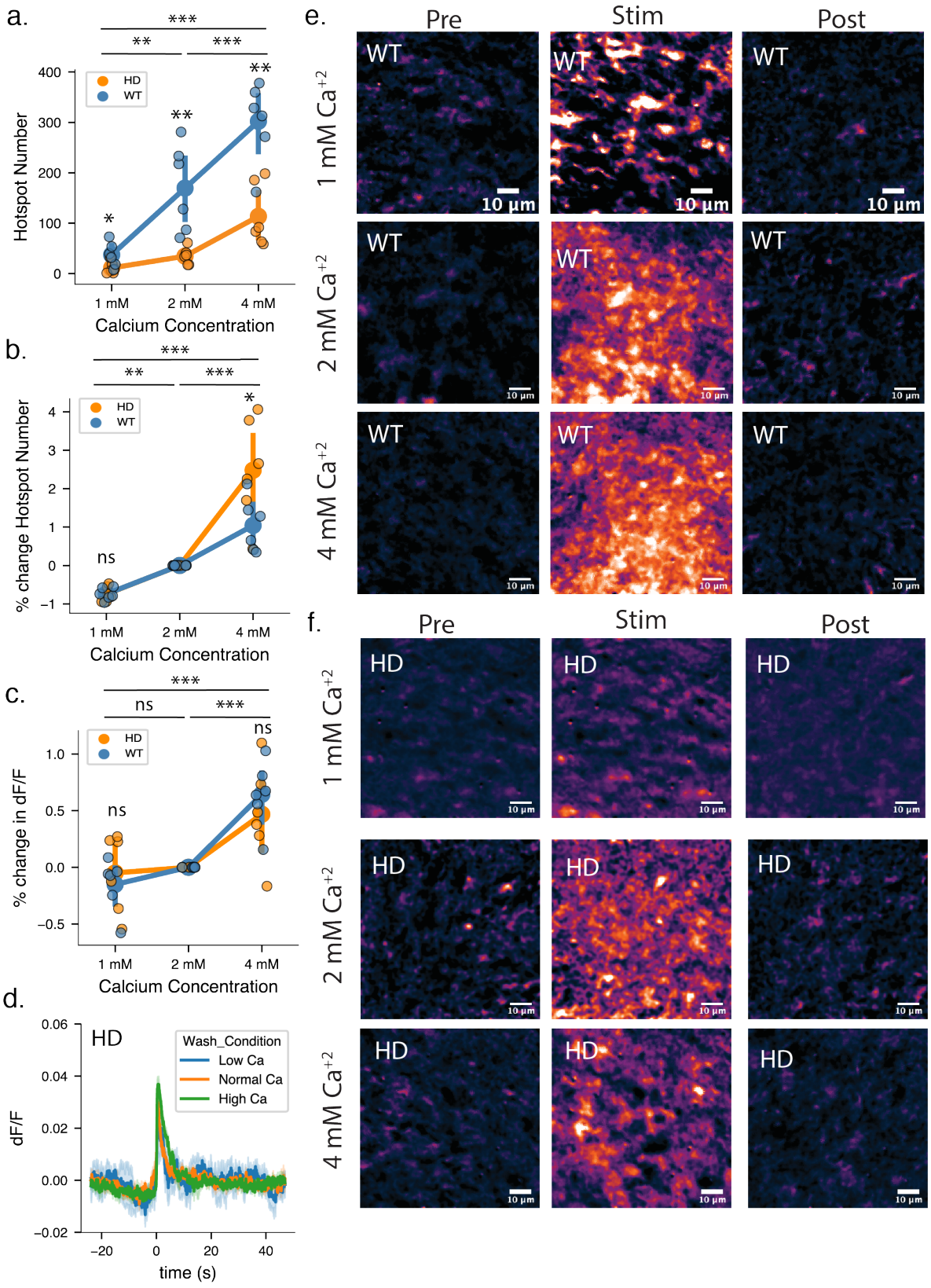

Figure 4.4: (Continued on the following page.)

Figure 4.4: R6/2 HD mice show diminished dopamine release at 12 weeks that is improved but not fully rescued by high extracellular calcium concentration A, The average number of dopamine hotspots active in 12 week R6/2 HD striatal brain slices in response to 0.3 mA stimulation is significantly diminished in comparison to WT brain slices. R6/2 HD slices show a 79.6% decrease in the number of dopamine hotspots at Normal $Ca^{+2}$and a 62.4% decrease in the number of dopamine hotspots at High Ca^{+2}. Increasing external calcium concentration results in an increased number of dopamine hotspots active in HD mice, but is not sufficient to fully rescue to WT levels. (WT N = 6 slices, 6 animals, HD N = 6 slices, 6 animals; mixed-ANOVA: disease state, p = 0.0010; wash condition, *** p ¡ 0.0005; interaction, p ¡ 0.0005; pairwise t-test: ** p = 0.0009 HD/4 mM Ca^{+2} compared to WT/ mM Ca^{+2}, ** p = 0.0036 HD/2 mM Ca^{+2} compared to WT/2 mM Ca^{+2}, * p = 0.0376 HD/1 mM Ca^{+2} compared to WT/1 mM Ca^{+2}). B, R6/2 HD slices show a 247.9% increase in dopamine hotspots number after 4 mM Ca^{+2} wash compared to R6/2 WT slices which show a 104.2% increase in dopamine hotspots after 4 mM Ca^{+2}. (mixed-ANOVA: disease state, p = 0.0383; wash condition, *** p ¡ 0.0005; interaction, p = 0.0170; pairwise t-test: ** p = 0.0429 HD/High Ca^{+2} compared to WT/High Ca^{+2}, nr p = 0.9681 HD/Low Ca^{+2} compared to WT/Low Ca^{+2}). C, R6/2 HD and WT slices show comparable increase in mean peak $\Delta F/F$ at all calcium concentrations. (mixed-ANOVA: disease state, p = 0.823; wash condition, *** p ¡ 0.0005; interaction, p = 0.381; pairwise t-test: nr p = 0.423 HD/4 mM Ca^{+2} compared to WT/4 mM Ca^{+2}, nr p = 0.568 HD/1 mM Ca^{+2} compared to WT/1 mM Ca^{+2}).D, Dopamine release and reuptake traces from imaged from 12 wk HD mice. Solid lines denote the average taken from all slices and light shaded bands represent one standard deviation from average behavior. A 1 ms, 0.3 mA stimulation is delivered at time = 0s. E, Representative images of dopamine release imaged in 12 week WT mice before, during, and after stimulated dopamine release. F, Representative images of dopamine release imaged in 12 week HD mice before, during, and after stimulated dopamine release.

Our findings from nIRCat imaging in R6/2 mice build upon existing Fast Scan Cyclic Voltammetry (FSCV) measurements in R6/2 mice literature that have previously reported that 12 week HD and WT mice show comparable percent change in peak dopamine release concentration in response to increasing extracellular concentration[117]. This discrepancy is likely the result of the spatial averaging that occurs during FSCV measurements which allows the comparable modulation of average dopamine release (% change mean peak $\Delta F/F$) in R6/2

HD an WT slices to to mask differences in dopamine hotspot addition (%change hotspot number). Despite the significant degeneration in the number of dopamine hotspots in 12 wk HD slices, the remaining hotspots in fact exhibit increased sensitivity to extracellular Ca^{+2}. This is an insight previously masked in spatially averaged measurements and reveal by the improved spatial resolution of nIRCat imaging. Furthermore, at 12 weeks there remains a population of dopamine hotspots in HD slices that can be made active through increasing the calcium influx into dopaminergic release sites. As such, changes in calcium dependent dopamine release in late HD may play a larger role in shaping late disease states than previously expected.

4.4 Conclusions

Extracellular calcium handling plays a pivotal role in dopamine release. Molecular distinctions in calcium-related molecular machinery have been suggested to distinguish between modes of fast and slow dopamine signaling, and disruptions in calcium handling have been implicated in Huntington's Disease related dysfunction[67;117]. To date, examinations of changes in dopamine release in response to extracellular calcium concentration have been primarily studied using spatially averaged tools such as FSCV[67;117]. While these methods offer insights into large-scale trends in extracellular calcium dependence, they are unable to provide deeper mechanistic insights into how trends manifest from the level of release sites[132]. In this chapter I demonstrate how nIRCat nanosensors can be used to examine the extracellular calcium dependence of dopamine release in WT R6/2 and HD R6/2 mice at early (4 week) and late (12 week) timepoints of disease progression.

Work in WT R6/2 mice show that increasing extracellular calcium concentration in striatal brain slices drives increased dopamine release through addition of dopamine hotspots and modulation of dopamine release from individual hotspots (mean peak $\Delta F/F$). These increases in dopamine hotspots are the result of new dopamine hotspots made active by increased Ca^{+2} influx rather than the modulation of weakly active dopamine hotspots into nIRCat's range of detection. Analysis of nIRCat imaging in WT R6/2 mice show calcium-dependent dopamine release dynamics similar to those identified in hippocampal glutamate neurons using genetically encoded pHluorins[132]. This similarity suggests that at least some subset of striatal dopamine release shows calcium mobilization dynamics similar to those used in fast-releasing synapses, in line with the recent body of work that indicates dopamine varicosities in the striatum contain fast dopamine release and calcium sensing machinery[65;67].

We utilized nIRCat's ability to visualize dopamine release without genetic manipulation to explore changes in dopamine release early and late in Huntington's Disease disease course. Early in disease at 4 weeks, nIRCat imaging of HD R6/2 mice exhibit increased modulation of dopamine hotspot release at high extracellular Ca^{+2} concentrations. This corresponds to an disease state where shifts in Ca^{+2} influx at dopamine terminals may drive unexpectedly large increases in dopamine release from dopamine hotspots in comparison to WT dynamics. Shifts in Ca^{+2} dependent dopamine release in HD R6/2 mice may arise as the direct result of mutant huntingtin disrupting Ca^{+2} dependent dopamine release or as a compensatory response from the striatal dopamine system to altered signaling in the striatum. As such, exploration into Ca^{+2} changes at 4 week in R6/2 HD slices may provide insight into opportunities for early intervention that correct aberrant signaling patterns and slow the accumulation of dowstream compensatory synaptic alterations.

Late in disease at 12 weeks, nIRCat imaging may provide insight into therapeutic opportunities for treatment late in the degeneration process. Previously in Chapter 3 I demonstrated that nIRCat imaging reveals that decreased dopamine release in 12 week R6/2 HD mice is driven by decreases in dopamine hotspot number and decreases in the average dopamine released from invidual dopamine hotspots (mean peak $\Delta F/F$). Using a Ca^{+2} concentration

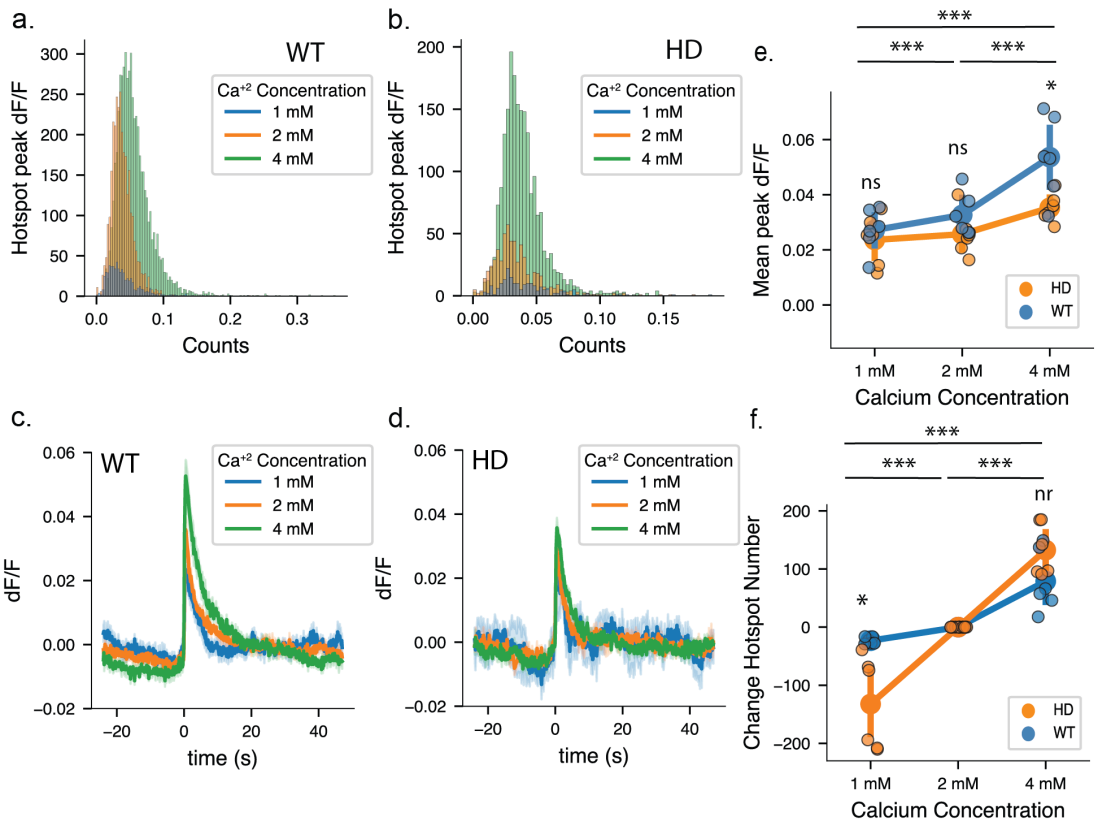

Figure 4.5: Pooled dopamine hotspot histograms and dopamine release and reuptake histograms for 12 week R6/2 HD and WT mice A, Histograms of pooled dopamine hotspots from 12 week WT mic. Dark blue bars show hotspots active at 1 mM Ca^{+2}, orange bars hotspots active at 2 mM Ca^{+2}, and green bars hotspots active at 4 mM Ca^{+2}. B. Histograms of pooled dopamine hotspots from 12 week HD mic. C, Dopamine release and reuptake traces from imaged nIRCat-labeled brain slices for 4 week WT mice. Solid lines denote the average taken from all slices and light shaded bands represent one standard deviation from average behavior. A 1 ms, 0.3 mA stimulation is delivered at time = 0s D, Dopamine release and reuptake traces from imaged nIRCat-labeled brain slices for 4 week HD mice. E, The average mean peak $\Delta F/F$ values recorded in 4 week HD and WT slices at 1 mM Ca^{+2}, 2 mM Ca^{+2}, and 4 mM Ca^{+2} (mixed-ANOVA: disease state, *p = 0.0471; wash condition, *** p ¡ 0.0005; interaction, p = 0.0379; pairwise t-test: * p = 0.0164 HD/4 mMCa^{+2} compared to WT/4 mM Ca^{+2}). F, Total change in hotspots number recorded in 12 week HD and WT slices at 1 mM Ca^{+2}, 2 mM Ca^{+2}, and 4 mM Ca^{+2} (mixed-ANOVA: disease state, p = 0.268; wash condition, *** p ¡ 0.0005; interaction, p ¡ 0.0005 ; pairwise t-test: * p = 0.0074 HD/1 mM Ca^{+2} compared to WT/1 mM Ca^{+2}).)

wash experimental framework I show that even at this late degeneration timepoint, previously inactive dopamine hotspots can be activated release dopamine at high extracellular Ca^{+2} concentration.

These findings suggest that the dopamine hotspot "loss" late in disease is likely the combined result of "anatomical loss" where dopamine hotspots are physically lost and "functional loss" where dopamine hotspots are physically maintained but unable to readily release dopamine.

Strikingly, the number of dopamine hotspots activated at high extracellular Ca^{+2} concentration is similar between R6/2 HD and WT slices, resulting in a higher percent increase in dopamine hotspot in R6/2 HD slices in comparison to their WT counterparts. These findings stand in contrast with previous methods taken in R6/2 mice using FSCV, which reported no significant difference in the extracellular calcium sensitivity of spatially averaged dopamine release of R6/2 WT and R6/2 HD mice at 12 weeks. As such, this work has provided new insights to the nature of Ca^{+2} disruption in Huntington's disease, underscoring the utility of nIRCat's role as a high spatial resolution sensor.

The foundational framework provided in this work for the analysis and interpretation of nIRCat calcium wash datasets may be utilized in future experiments to explore possible mechanisms for Ca^{+2} disruption in HD or to understand how calcium-targeted pharmacology may provide therapeutic benefit to slow HD degeneration. Similarly, this framework can be readily adapted for study of Ca^{+2} dependent dopamine release in other neurodegenerative disease such as Parkinson's Disease and Alzheimer's Disease or to study changes in Ca^{+2} dependent dopamine over healthy brain development.

4.5 Materials and Methods

4.5.1 Animals

Male B6CBA-Tg(HDexon1)62Gpb/3J mice (R6/2 mice) were purchased from Jackson Labs and bred at 6 weeks with 10 week old female C57BL/6 mice. Pups were weaned and genotyped for the human HD fragment at 3 weeks. Mice were housed at three to five animals per cage with food and water available ad libitum and maintained in a temperature-controlled environment on a 12h dark/light cycle with light-on at 7:00 am and light-off at 7:00 pm. All animal procedures were approved by the University of California Berkeley Animal Care and Use Committee.

4.5.2 nIRCat Nanosensor synthesis and characterization

Dopamine nIRCat nanosensor was synthesized and characterized as described previously described in (Yang et al., 2021). A single walled carbon nanotube (SWNT) slurry was created by combining 1050 mg of hydrated HiPco SWNTs purchased from NanoIntegris with 25 mL of molecular grade water in a 50 mL Falcon Tube and probe sonicating the solution for 2 minutes at 10% amplitude until the slurry is visually distributed. To create nIRCat nanosensors, 100 µl of SWNT slurry was mixed with 1 mg of (GT)6 oligonucleotides purchased from Integrated DNA Technologies (standard desalting) in 100 mM and bath sonicated for 10 minutes (Branson Ultrasonic 1800) followed by 5 minutes of rest at room temperature. The solution was then sonicated on ice for 10 minutes using a probe-tip

sonicator (Cole-Parmer Ultrasonic Processor, 3-mm diameter tip, 5 W power) followed by 5 minutes of rest on ice. The sonicated solution was incubated at room temperature for 30 mins and centrifuged at 16,000 g (Eppendorf 5418) for 30 minutes to removed unsuspended SWNT bundles and amorphous carbon. The supernatant is the removed for use and stored at 4°C for 30 minutes before characterization. Final supernatant should be stored at 4°C until use.

Nanosensors are synthesized in 1 mL batches and combined for characterization. Nanosensor concentrations were determined using absorbance at 632 nM with an extinction coefficient of 0.036 (mg/L)-1cm-1. To characterize the visible and nIR absorption spectrum, nanosensors were diluted to a concentration of 5 mg/L in 1x PBA and taken using a UV-VIS-nIRC spectrophotometer (Shimadzu UV-3600 Plus). To test fluorescent response to dopamine administration, each sensor batch is diluted to a working concentration of 5 mg/L in 1x PBS and 198 µl aliquots are made into a 96-well plate and baseline fluorescence is taken using a 20x objective on an inverted Zeiss microscope (Axio Observer D1) coupled to a Princeton Instruments spectrograph (SCT 320) and a liquid nitrogen cooled Princeton Instruments InCaAs linear array detector (PyLoN-IR). Nanosensors were excited using a 721-nm lazer (Opto Engine LLC). After the baseline fluorescence was taken, 2 µl of 10 mM Dopamine in 1xPBS is added and a robust fluorescence response to dopamine was confirmed.

4.5.3 Phenotypic Motor Coordination Assessment

The accelerating Rotarod test and hind limb clasp test were used to evaluate changes in motor coordination in R6/2 and WT mice. For accelerating rotarod tests, mice were placed on a Ugo Basile rotarod for 1 min a 5 rpm to adjust to the apparatus. At the end of the 1 min adjustment period, the speed of the rotarod was increased at a constant rate to a final speed of 40 rpm over 350 s. The trial is terminated after mice either fall off the rod, tumble on the rod for two consecutive rotations, or "max out" the rod speed at 360s. Starting at four weeks, mice are introduced to the rotarod and complete the test for 3 consecutive days, before their rotarod times plateau and performance is recorded on the fourth day. For subsequent weeks, mice complete the rotarod only once a week.

Hind limb clasp tests are conducted by grasping mice at the base of the tail and lifting the mouse off the ground for 10 s. Mice that show splayed out legs are assigned a score of 0, mice that contract one hindlimb are scored at 1, mice contract both hindlimbs are scored at 2, and mice that retract both hindlimbs full and curl into the abdomen are scored at 3.

4.5.4 nIRCat dopamine Imaging

Acute live brain slices were prepared using protocols previously described (Yang et al., 2021). Briefly, mice are deeply anesthetized via intraperitoneal ketamine/xylazine cocktail and perfused transcardially using cold cutting buffer (119 mM NaCl, 26.2 mM NaHCO3,

2.5 mM KCl, 1 mM NaH2PO4,3.5 mM MgCl2, 10 mM glucose, and 0 mM CaCl2). The brain was then rapidly dissected, mounted on a vibratome stage (Leica VT1200 S) using super glue, and cut into 300 µm thick slices containing the dorsal striatum. Slices were then collected and incubated at 37°C for 30 minutes in oxygen saturated ACSF (119 mM NaCl, 26.2 mM NaHCO3, 2.5 mM KCl, 1 mM NaH2PO4, 1.3 mM MgCl2, 10 mM glucose, and 2 mM CaCl2) followed by 30-minute incubation at room temperature. All slices are maintained at room temperature until imaging and used within 6 hours of preparation.

Slices are labeled through passive incubation in 5 ml of ACSF containing nIRCat nanosensor at a concentration of 2 mg/L for 15 minutes. After incubation, the slices is transferred through 3 wells of a 24-well plate containing ACSF to rinse off non-localized nIRCat sensor and then left to rest at room temperature ACSF for 15 minutes before transfer to the 32°C recording chamber. Once placed in the recording chamber, slices equilibrate for 15 minutes during which a tungsten bipolar stimulation electrode is positioned at a field of view in the dorsal-lateral striatum using a 4x objective (Olympus XLFluor 4/ 340). Under a 60x objective the electrode is moved 200 µm away from the selected field of view and brought into contact with the surface of the brain slice. In all experiments, 600 total images are acquired into an image-stack at a rate of 9 frames per second. A single stimulation of 0.1 mA or 0.3 mA is applied after 200 frames of baseline are collected. Videos of stimulation at each strength are collected in triplicate and stimulation strengths are alternated. All slices are given 5 minutes between each stimulation with the excitation laser path shuttered. Prior to stimulation, the laser is un-shuttered for 1 minutes.

4.5.5 nIRCat Imaging Calcium Wash and Sulpiride wash

To image nIRCat-labeled acute brains slices at multiple extracellular calcium concentrations, buffers were prepared at three calcium concentrations: 1 mM Low Calcium Buffer (119 mM NaCl, 26.2 mM NaHCO3, 2.5 mM KCl, 1 mM NaH2PO4, 1.3 mM MgCl2, 10 mM glucose, and 1 mM CaCl2), 2 mM Normal Calcium Buffer (119 mM NaCl, 26.2 mM NaHCO3, 2.5 mM KCl, 1 mM NaH2PO4, 1.3 mM MgCl2, 10 mM glucose, and 2 mM CaCl2), 4 mM High Calcium Buffer (119 mM NaCl, 26.2 mM NaHCO3, 2.5 mM KCl, 1 mM NaH2PO4, 1.3 mM MgCl2, 10 mM glucose, and 4 mM CaCl2). Following stimulation in 2 mM Normal Calcium Buffer, 4 mM High Calcium buffer was flowed into the imaging chamber for 15 minutes (Full bath turnover in 3 minutes). After buffer transfer, the slice was stimulated at 0.1 mA and 0.3 mA in triplicate as described for 2 mM Normal Calcium Buffer. Buffer was then exchanged again to 1 mM Low Calcium Buffer via 15-minute wash and the slice was stimulated at 0.1 mA and 0.3 mA in triplicate.

To nIRCat image acute brain slices in the presence of the D2-antagonist Sulpiride, S-Sulpiride was dissolved in sterile DMSO and frozen in 100 µl aliquots at -20°C. Prior to use, single aliquots are thawed and added to 100 mL of ACSF to produce a 10 µM Sulpiride solution. Acute brain slices were stimulated at 0.1 mA and 0.3 mA in triplicate in sulpiride-free ACSF. Sulpiride solution was flowed into the imagine chamber for 15 minutes before stimulating

the slice at 0.1 mA and 0.3 mA in triplicate.

4.5.6 Image Stack Processing and Data Analysis of nIRCat Data

Raw Image stack files are processed using a custom-built, publicly available MATLAB program (https://github.com/jtdbod/Nanosensor-Imaging-App). Image processing procedures are described in depth in Yang, del Bonis O'Donnel et al and briefly summarized here. Regions of dopamine release are identified by large changes in nIRCat $\Delta F/F$ response. To minimize bias and improve stack processing time, regions of high $\Delta F/F$ response (dopamine hotspots) were identified by defining a grid of 2 µm squares across the field of view. For each grid square $\Delta F/F$ was calculated using the formula (F- F0) /F0, where F0 is defined by the average fluorescence of the grid square over the first 30 frames of the image stack and F is the fluorescence intensity of the gird square as it changes over the 600 collected frames. Grid squares are identified as regions of interest if they exhibit behavior that is 3 standard deviations above the baseline F0 activity around time of stimulation (200 frames).

Dopamine hotspots were identified for each stimulation replicate image stack taken at a given field-of-view on a brain slice. The peak $\Delta F/F$ of each dopamine hotspot in the image stack were averaged to give the average image stack peak $\Delta F/F$. The average image stack peak $\Delta F/F$ from the three stimulation replicates were then average to give the slice average peak $\Delta F/F$. Similarly, the number of dopamine hotspots identified from each stimulation replicate image stack were averaged to give the slice average hotspot number. Mean dopamine release and reuptake traces are produced by averaging the average traces from each slice (3 stimulations per slice, 1 slice per animal). Percent change in hotspots was calculated as (number hotspots wash - number hotspots 2 mM Ca^{+2})/ (number hotspots 2 mM Ca^{+2}), whereas change in hotspots number was calculated as (number hotspots wash - number hotspots 2 mM Ca^{+2}).

To track hotspot fidelity, each initially defined grid square was assigned a unique position number, allowing the position of each identified dopamine hotspot within an image stack to be recorded. For a set of triplicate image stacks, an array of all unique hotspots active across the stimulation replicates was generated. Then python code was used to analyze whether each unique hotspot was active in each stimulation replicate. The number of stimulations a unique hotspot was active in was summed across the three replicates and assigned as the dopamine release fidelity (e.g. hotspot '12' is active in 2 out of 3 stimulations and is assigned release fidelity 2). The same procedure was used to identify the dopamine release fidelity of hotspots active after drug wash. Hotspots were then separated into three groups: hotspots that are active both before and after drug wash (shared hotspots), hotspots that become active after drug wash (added hotspots), and hotspots that are only active before drug wash. For shared hotspots modulation in hotspot release strength was calculated as the difference in peak $\Delta F/F$ of the unique hotspot before and after drug wash, (mean $\Delta F/F$)post - (mean $\Delta F/F$)pre , where (mean $\Delta F/F$)pre is the average peak $\Delta F/F$ of each unique dopamine hotspot across the three stimulations before drug wash and (mean $\Delta F/F$)post is the average

peak ΔF/F of each unique dopamine hotspot across the three stimulations after drug wash. For hotspots active only after drug wash, there is no corresponding "pre drug wash" ΔF/F. Therefore, the difference in peak ΔF/F was calculated through (mean ΔF/F)post - (mean ΔF/F)pre, shared, where (mean ΔF/F)post represents the average peak ΔF/F of the unique dopamine hotspot active after sulpiride wash across three stimulations and (mean ΔF/F)pre, shared is the average of all the shared hotspots' mean ΔF/F from the slice before drug wash.

4.5.7 Exerimental Design and Statistical Analysis

All nIRCat Imaging data were processed using a custom-built, publicly available MATLAB program (https://github.com/jtdbod/Nanosensor-Imaging-App). Statistical analyses were conducted using the open-source statistical python package pingouin. All bar graphs show the mean with error bars denoting the 95% confidence interval. All single data points correspond to a single slice taken from an animal. Data comparing two variables was analyzed using a mixed-ANOVA with wash condition as the within-subject factor (e.g.sulpiride, blank, calcium concentration) and disease state as the between-subject factor (eg. HD, WT). Paired t-tests were used a post-hoc tests if mixed-ANOVA analyses indicated significant differences. Data comparing two values of one variable were analyzed using tukey's t-test. Group sizes were determined based on previous literature (Adil et al., 2018). Changes in histogram skew were computed through pooling of all hotspots identified across all mice within the disease and wash condition and evaluated using a permutation test using the test statistic μ = skew(post wash) – skew(pre-wash).

Chapter 5

Elucidating D2-Autoreceptor Regulation of Dopamine Release in R6/2 Huntington's Disease Model Mice using nIRCat [v]

[v]This section is produced in part with permission from the following work: Yang, S. J., et al. "Synaptic scale dopamine disruption in Huntington's Disease model mice imaged with near-infrared catecholamine nanosensors."

5.1 Abstract

D2-autoreceptors located on dopamine-releasing presynaptic boutons play a key role in regulating striatal dopamine release. Historically, study of these receptors has been challenging due to difficulties separating the activity of presynaptic D2-autoreceptors and postsynaptic D2 receptors. Decreases in overall D2-receptor expression and transcription have been documented in both the striatum of HD model mice and human HD patients. However, little is known about how these changes specifically affect D2-autoreceptors. In this work we utilize nIRCat imaging to visualize dopamine hotspot response to wash-on of the D2 receptor antagonist Sulpiride. We find that Sulpiride antagonsim of D2-autoreceptors increases the number of active dopamine hotspots as well as their mean peak $\Delta F/F$. Interestingly, we find that dopamine hotspot sensitivity to sulpiride response changes in R6/2 WT mice between 4 weeks and 12 weeks of age. Furthermore, R6/2 HD mice show differing response to sulpiride early in disease at 4 weeks but no difference in percent change of hotspot number of mean peak $\Delta F/F$ late in disease at 12 weeks. These findings underscore the utility of nIRCat's compatibility with dopamine pharmacology and suggest a role for D2-autoreceptors in the development of healthy mice as well as early disease dynamics within HD.

5.2 Introduction

Axonal dopamine release in the striatum is regulated at multiple stages of the dopamine release process. As such, the amount of axonal dopamine release from striatal varicosities does not scale purely with the intracellular Ca^{+2} level[66]. Dopamine signals through D1-type and D2-type dopamine receptors, which couple to excitatory and inhibitory G-protein pathways respectively. Dopaminergic receptors are primarily located on non-dopaminergic neurons where they are termed heteroreceptors. Within the stratum, dopamine heteroreceptors are primarily found on medium spiny neurons (MSNs) where they allow dopamine released in the striatum to modulate MSN activity (Fig.5.1a).

The discovery of D2-type dopamine receptors on the soma, dendrites, and axonal terminals of dopaminergic neurons themselves revealed that dopamine could also shape its own release[133;134;135] (Fig.5.1a). These receptors on dopaminergic neurons are termed autoreceptors and their activation initiates intracellular processes within dopaminergic neurons to inhibit future dopamine through presynaptic feedback inhibition[13;136;137]. Though the exact mechanism that underlies this feedback inhibition is still unknown, D2-autoreceptor activation has been demonstrated to directly modulate dopamine release through action on voltage gated calcium currents and involvement of inhibitory G-protein activated inwardly rectifying potassium channels (GIRK)[138] (Fig.5.1b). Indirect modulation of dopamine release is also achieved by D2-autoreceptor modulation of dopamine synthesis via tyrosine hydroxylase (TH) and regulation of the expression of neuronal vesicular monoamine transporter (VMAT2)[13;139;140]. Altogether, these action result in decreased dopamine release and decreased excitability of dopaminergic neurons.

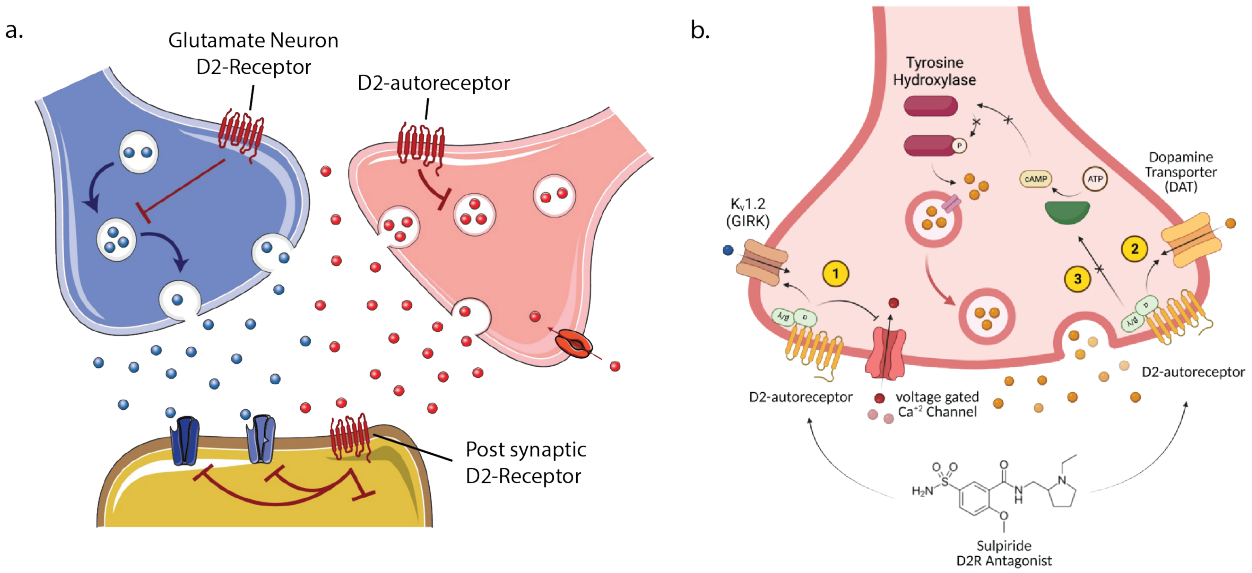

Figure 5.1: D2-Autoreceptors regulate dopamine signaling at the site of release A. Type D2 dopamine receptors are expressed postsynaptically on medium spiny neurons (yellow) and presynaptically on glutamatergic cortical projection neurons (blue) and dopaminergic neurons (red). B. Sulpiride antagonism of D2-autoreceptors drives increased dopamine release through action on Kv1.2 channels, voltage gated calcium channels, dopamine transporters, and synthesis of dopamine via tyroside hydroxylase

Decreases in D2-receptor expression and transcription have been documented in both the striatum of HD model R6/2 mice and within the caudate of human HD patients[141;142]. However, little is known about how D2-autoreceptors play a role during this degenerative process. This is due to the difficulty in separating the activity of D2-autoreceptors from D2-heteroreceptors. Separation of autoreceptor function from heteroreceptor function is typically accomplished through specifically measuring presynaptic dopamine release while modulating collective D2-receptor activity through D2-receptor specific drug wash. Increasingly refined targeting of auto-receptor specific function has been achieved through generation D2-autoreceptor specific knock out mice, which display increased locomotor hyperactivity and sensitivity to cocaine[143;144]. Study of acute striatal brain slices from D2-autoreceptor knock out mice using Fast Scan Cyclic Voltammetry (FSCV) show that these animals are insensitive to sulpiride and quinpirole, indicating that that D2 receptors are the predominant D2-autoreceptor subtype. In line with this body of work, nIRCat nanosensors have previously been used examine D2-autoreceptor activity in the dorsal medial striatum and shown that dopamine hotspots show heterogenous modulation of response after Sulpiride wash. We build upon this emerging understanding of D2-autoreceptor function and leverage the spatial resolution of nIRCat imaging to study changes in D2-autoreceptor in the dorsal lateral striatum of R6/2 HD mice early and late in disease.

5.3 Results and Discussion

5.3.1 Analysis Strategies for Dopamine Hotspot Sulpiride Response

Sulpiride antagonism of inhibitory D2-autoreceptor pathways results in increased striatal dopamine release[9;145;146] (Fig.5.1b). As such, we hypothesize that this increase in dopamine release can manifest through an increase in dopamine hotspots, increase in mean peak $\Delta F/F$, or a combination between hotspot and mean peak $\Delta F/F$ increase. Previous analyses of nIRCat imaging in the dorsal medial striatum tracked dopamine release from a set number of dopamine hotspots. This set of dopamine hotspots, referred to as a "mask", was selected from a single stimulation taken in Blank ACSF and used across all stimulation replicates and drug wash conditions. This strategy allowed single hotspots to be tracked across before and after Sulpiride wash and demonstrated that Sulpiride wash in the dorsal medial striatum results in an increase in mean peak $\Delta F/F$ of dopamine hotspots. A challenge in using the mask method to track dopamine hotspots across drug washes is that it fixes the number of dopamine hotspots across stimulations and drug washes. While measuring dopamine release in the dorsal lateral striatum we observed a marked change in the number of dopamine hotspots between stimulation replicates and in response to drug wash. Tracking dopamine hotspots in this context using the mask method would fail to capture this dynamic. Furthermore, tracking of dopamine hotspots using the mask method assumes that dopamine hotspots are consistently active across multiple stimulations and drug washes. For experiments in this work, we chose to instead use a strategy of analyzing the population of all active dopamine hotspots rather the mask method in order to fully analyze how dopamine hotspots respond to sulpiride wash through dopamine hotspot activation and mechanisms of hotspot modulation.

5.3.2 D2-Autoreceptor Response to Sulpiride Wash in R6/2 WT Mice

We first sought to characterize how nIRCat visualized dopamine hotspots in WT animals change in number and mean peak $\Delta F/F$ in response to 1 µM sulpiride wash. NIRCat labeled 4 week and 12 week R6/2 WT brain slices were subject to a 0.3 mA, 1 ms electrical stimulus taken in triplicate while in sulpiride-free ACSF (Blank ACSF). Following baseline measurements in Blank ACSF, slices were bathed in 1 µM sulpiride for 15 min and stimulated in triplicate at the same field of view. Consistent with previous findings reported in Chapter3, R6/2 WT animals at 4 weeks and 12 weeks showed a comparable number of dopamine hotspots in blank ACSF before sulpiride wash (Fig.5.2a, (Fig.5.4a).

Sulpiride wash-on to 4 week slices resulted in a moderate percent increase in dopamine hotspots (Fig.5.2a). In contrast, sulpiride wash onto 12 week slices resulted in a larger percent increase in dopamine hotspots number (Fig.5.4b). This increase in dopamine hotspot addition does not appear to be driven by an increase in sulpiride's ability to modulate the

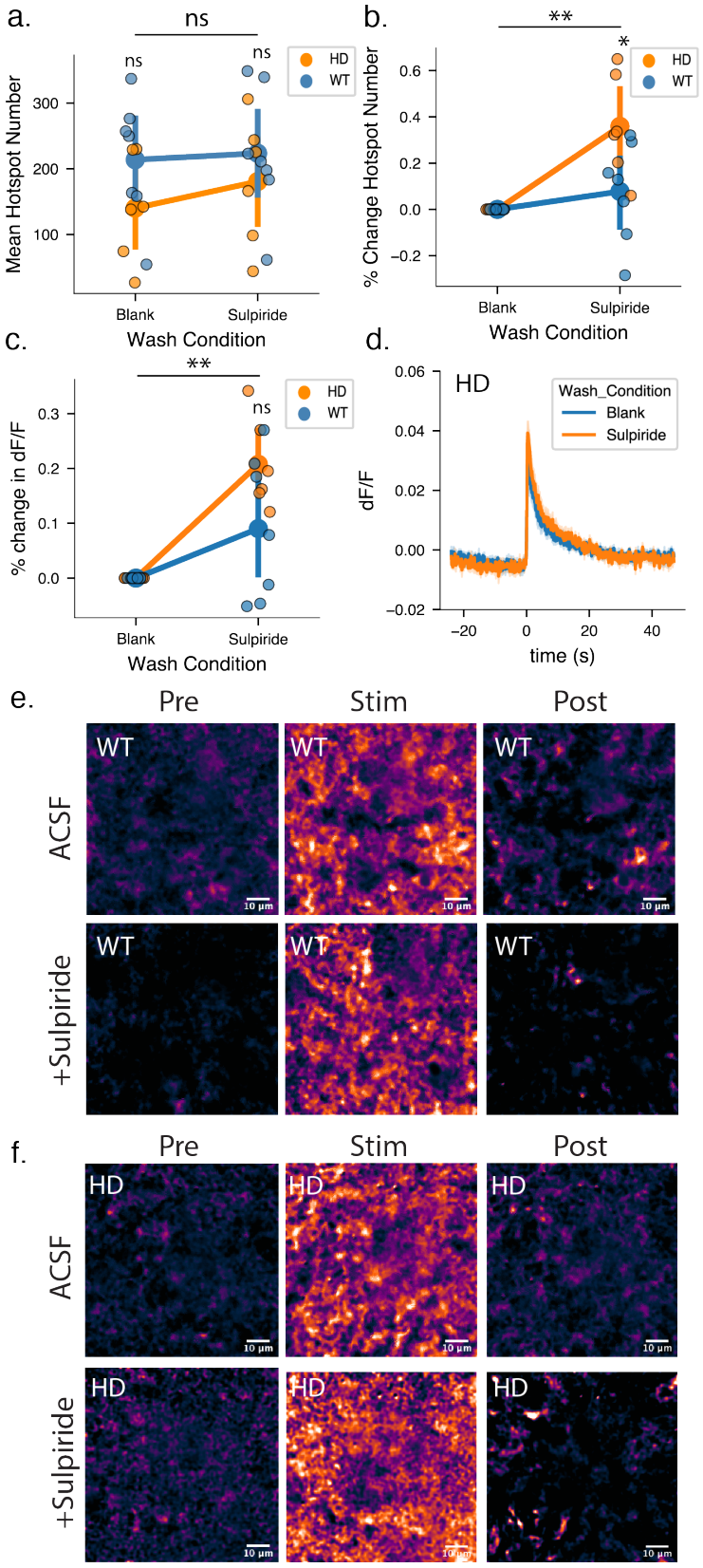

Figure 5.2: Both WT and R6/2 HD mice at 4 weeks show modulation of dopamine release via D2-autoreceptor antagonist Sulpiride (Continued on the following page.)

Figure 5.2: (continued) A, Both WT and R6/2 HD slices show a comparable increase in active dopamine hotspots in response to 0.3 mA stimulation after Sulpiride wash. (WT N = 7 slices, 7 animals, HD N = 6 slices, 6 animals; mixed-ANOVA: disease state, p = 0.2728; wash condition, p = 0.0733; interaction, p = 0.2313; paired t-test: nr p = 0.1589 HD/Blank compared to WT/Blank, nr p = 0.4469 HD/Sulpiride compared to WT/Sulpiride) B, R6/2 HD slices show a larger percent increase in dopamine hotspots after Sulpiride wash compared to WT slices at 4 weeks (mixed-ANOVA: disease state, p = 0.0419; wash condition, ** p ¡ 0.0059; interaction, p = 0.0419; paired t-test: * p = 0.0433 HD/Sulpiride compared to WT/Sulpiride). C, Both R6/2 HD and WT slices show similar increase in percent increase in peak ΔF/F after Sulpiride wash (mixed-ANOVA: disease state, p = 0.088; wash condition, p = 0.001; interaction, p = 0.0878; paired t-test: ns p = 0.080 HD/Sulpiride compared to WT/Sulpiride). D, Dopamine release and reuptake traces from 12 wk HD mice. Solid lines denote the average taken from all slices and light shaded bands represent one standard deviation from average behavior. A 1 ms, 0.3 mA stimulation is delivered at time = 0s. E, Representative images of dopamine release imaged in 4 week WT mice before, during, and after stimulated dopamine release in the presence and absence of Sulpiride. F, Representative images of dopamine release imaged in 4 week HD mice before, during, and after stimulated dopamine release in the presence and absence of Sulpiride.

mean peak ΔF/F of dopamine hotspots at 12 weeks compared to 4 weeks as WT R6/2 slices show similar percent increase in mean peak ΔF/F of dopamine hotspots at both 4 weeks and 12 weeks (Fig.5.2c, Fig.5.4c). Furthermore, both 4 week and 12 week hotspots show a full normal distribution under blank and sulpiride wash, suggesting that hotspot intensity modulation alone does not drive the increase in dopamine hotspots (Fig.5.3a, Fig.5.5a). These results suggest that D2-autoreceptor regulation may change over the course of development from 4 weeks to 12 weeks.

We also note that sulpiride-induced modulation of dopamine hotspot peak ΔF/F measured in the dorsal lateral striatum of R6/2 HD and WT mice is smaller than previously recorded modulations in the dorsal medial striatum of C57BL/6J mice (Fig.5.3c-d, Fig.5.5 c-d)[9]. This may be a result of the different hotspot identification strategies used between these studies, or a biologically notable difference between patterns of dopamine signaling in the dorsal lateral striatum and dorsal medial striatum. Further study comparing the signaling dynamics observed between these two regions is needed to fully characterize differences in signaling dynamics throughout the striatum.

5.3.3 Changes in D2-Autoreceptor Response to Sulpiride Wash Over the Course of Huntington's Disease in R6/2 Mice

We next examined the effect of sulpiride on R6/2 HD and R6/2 WT slices early in disease at 4 weeks. While the number of dopamine hotspots in R6/2 HD and R6/2 WT slices is not significantly different at 4 weeks, R6/2 HD and R6/2 WT slices do show differences in the number of dopamine hotspots added by sulpiride wash (Fig.5.2a-b). Wash on of sulpiride did not initially appear to drive an increase in the average number of dopamine hotspots

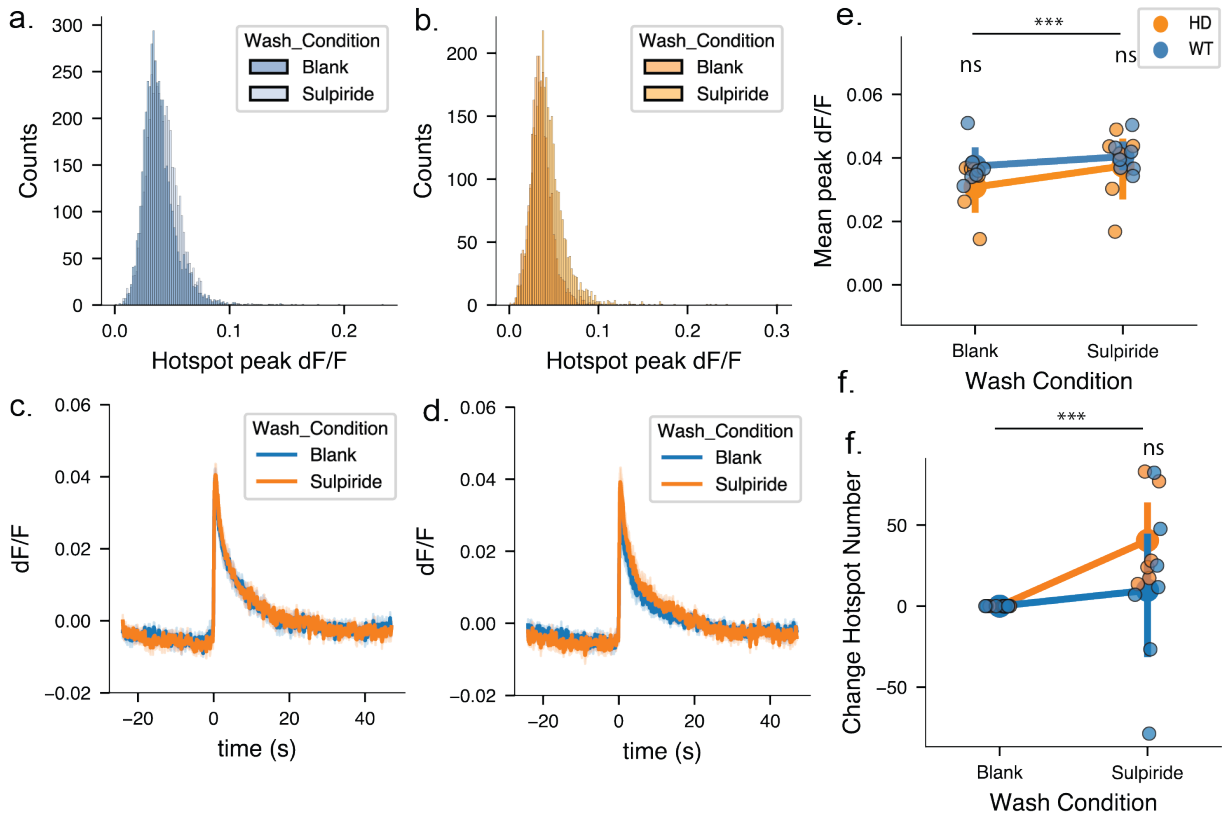

Figure 5.3: Pooled dopamine hotspot histograms and dopamine release and reuptake traces for 4 week R6/2 HD and WT mice after Sulpiride Wash A, Histograms of pooled dopamine hotspots from 4 week WT mic. Dark blue bars show hotspots active before Sulpiride wash, and light blue bars show hotspots active after Sulpiride wash. B. Histograms of pooled dopamine hotspots from 4 week HD mic. Dark orange bars show hotspots active before Sulpiride wash, and light orange bars show hotspots active after Sulpiride wash. C, Dopamine release and reuptake traces from imaged nIRCat-labeled brain slices for 4 week WT mice. Solid lines denote the average taken from all slices and light shaded bands represent one standard deviation from average behavior. A 1 ms, 0.3 mA stimulation is delivered at time = 0s D, Dopamine release and reuptake traces from imaged nIRCat-labeled brain slices for 4 week HD mice. E, The average mean peak $\Delta F/F$ values recorded in 4 week WT and HD slices before and after Sulpiride wash (mixed-ANOVA: disease state, p = 0.310; wash condition, ** p = 0.002; interaction, p = 0.1466; pairwise t-test: ns p = 0.1676 HD/No Sulpiride compared to WT/No Sulpiride; ns p = 0.5927 HD/Sulpiride compared to WT/Sulpiride). F, Total change in hotspots number recorded in 4 week WT and HD slices after Sulpiride Wash (mixed-ANOVA: disease state, p = 0.231; wash condition, ns p = 0.073; interaction, p = 0.231 ; pairwise t-test: ns p = 0.2170 HD/Sulpiride compared to WT/Sulpiride)

active across all 4 week R6/2 HD and R6/2 WT slices (Fig.5.2a). However, examination of the percent increase in dopamine hotpot number within each brain slice showed that sulpiride wash drives a significant percent increase in dopamine hotspots in both R6/2 WT and R6/2 HD slices from the initial number of dopamine hotspots active in blank ACSF (Fig.5.2 b). Intriguingly, R6/2 HD slices show a larger percent increase in dopamine hotspots following

sulpiride wash than R6/2 WT slices. This may be in part due to observed decreases in dopamine hotspot number in a portion of R6/2 WT slices, an event that was principally observed in WT slices with a large number of dopamine hotspots initially active in blank ACSF prior to sulpiride wash. Both 4-week R6/2 HD and R6/2 WT slices show a comparable percent increase in mean peak $\Delta F/F$ after Sulpiride wash (Fig.5.2c-d). Collectively, these findings suggest that D2-autoreceptor expression and signaling may differ in R6/2 WT and HD slices early in disease.

To further explore disease-related changes in D2-autoreceptors, we assessed response to sulpiride wash in R6/2 HD and WT mice late in HD at 12 weeks. Similar to observed dopamine hotspot response at 4 weeks, both WT and HD mice show increased hotspot number and slice average peak $\Delta F/F$ in response to sulpiride wash on at 12 weeks (Fig.5.4a-b). Interestingly, WT and HD slice show comparable percent increase in dopamine hotspots and slice average peak dopamine $\Delta F/F$ after sulpiride wash (Fig.5.4b-c). This stands in contrast to the increased sulpiride-driven percent increase in dopamine hotspots observed in R6/2 HD mice over R6/2 WT mice at 4-weeks. Comparisons between timepoints suggest that this is primarily due to changes in WT response to sulpiride between 4 weeks and 12 weeks (Fig s5b). R6/2 WT slices show moderate increase in dopamine hotspot number and slice average peak $\Delta F/F$ in response to sulpiride at 4 weeks and a more dramatic increase in both measures at 12 weeks (Fig.5.2b, Fig.5.4b). In contrast R6/2 HD slices show comparable response at 4 weeks and 12 weeks (Fig.5.2b, Fig.5.4b). This may suggest that D2-autoreceptor signaling varies over striatal development in R6/2 WT mice, and this signaling is disrupted in R6/2 HD mice. These disruptions may be compensatory changes initiated in the striatum in response to disease conditions or dysfunction in dopamine-related molecular machinery that drive later disease states.

5.4 Conclusions

D2-autoreceptors play a critical role in shaping dopamine release in the striatum by regulating future dopamine signaling at the site of of release. Though changes in overall D2 receptor expression and transcription are have been documented in HD patients and R6/2 HD model mice, specific isolation of D2-autoreceptor action on dopamine release remains technologically challenging[50;141]. Spatially averaged dopamine measurements from methods such as Fast Scan Cyclic Voltammetry are unable to distinguish between post synaptic D2 receptors and presynaptic D2-autorecptors. Presently available genetically encoded dopamine sensors are limited in their compatibility with dopamine pharmacology, as their dopamine receptor derived binding domain results in modulation of sensor output in response to both dopamine release and presence of pharmacological agents. In this work we utilize nIRCat's pharmacological compatibility and ability to track individual dopamine hotspots to examine how dopamine hotspots response to D2-autoreceptor antagonism via sulpiride.

We first demonstrate that nIRCat is capable of visualizing sulpiride-responsive dopamine hotspots in dorsal lateral striatum R6/2 WT slices. Wash on of sulpiride to R6/2 WT slices

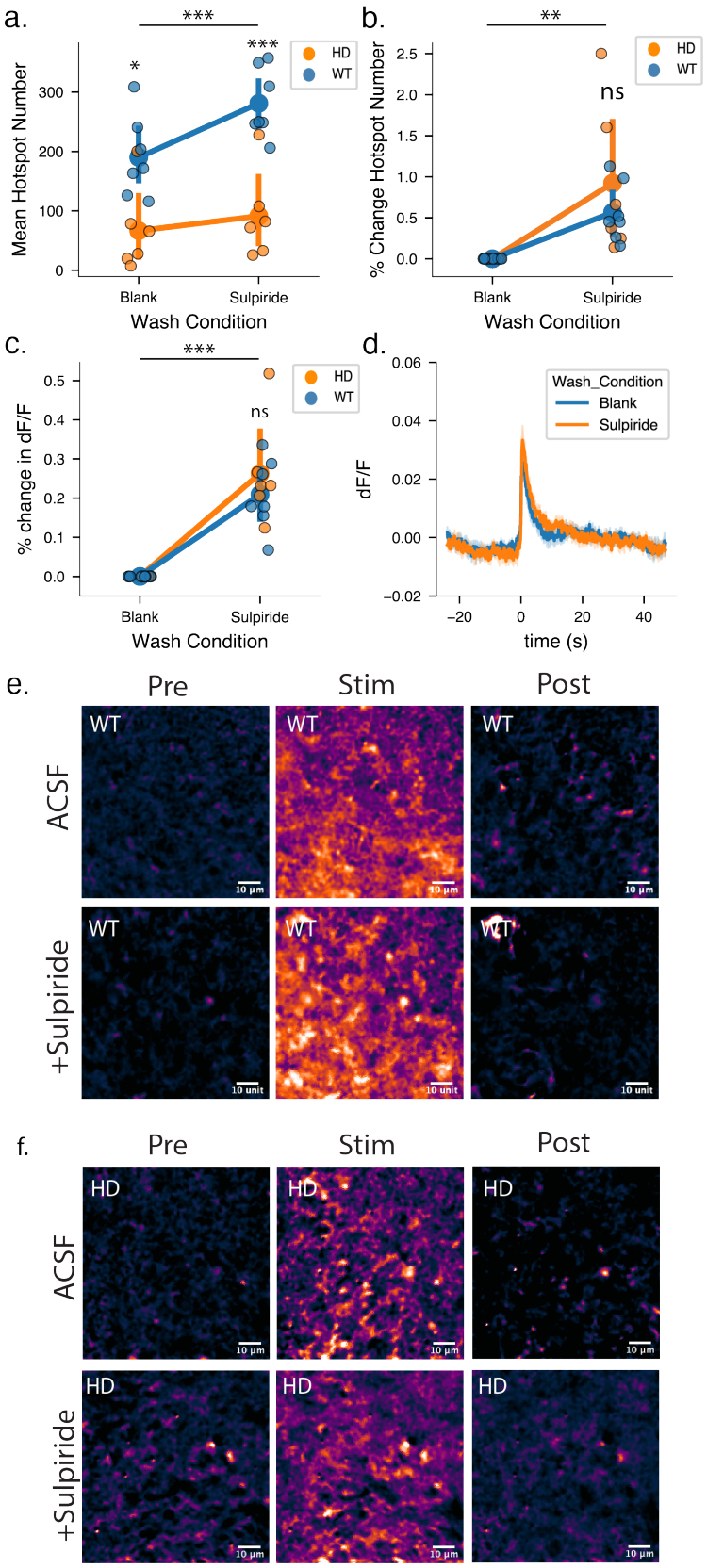

Figure 5.4: R6/2 HD mice at 12 weeks show comparable sensitivity to modulation of dopamine release via D2-autoreceptor antagonist Sulpiride (Cont. on the following page.)

Figure 5.4: (continued) A, WT mice show a significant increase in the number of active dopamine hotspots in response to 0.3 mA stimulation after Sulpiride wash. In contrast, R6/2 mice show a significantly blunted increase in active dopamine hotspots. (WT N = 7 slices, 7 animals, HD N = 6 slices, 6 animals; mixed-ANOVA: disease state, p = 0.001; wash condition, *** p ¡ 0.0005; interaction, p = 0.001; paired t-test: * p = 0.009 HD/Blank compared to WT/Blank, ** p ¡ 0.0005 HD/Sulpiride compared to WT/Sulpiride) B, Sulpiride wash results in comparable percent increase of dopamine hotspots in 12 week R6/2 HD and WT mice. (WT N = 7 slices, 7 animals, HD N = 6 slices, 6 animals; mixed-ANOVA: disease state, p = 0.074; wash condition, p = 0.003; interaction, p = 0.369; paired t-test: ns p = 0.412 HD/Sulpiride compared to WT/Sulpiride). C, Both R6/2 HD and WT slices show similar increase in percent increase in peak $\Delta F/F$ after Sulpiride wash (WT N = 7 slices, 7 animals, HD N = 6 slices, 6 animals; mixed-ANOVA: disease state, p = 0.411; wash condition, p ¡ 0.0005 ; interaction, p = 0.411; paired t-test: ns p = 0.429 HD/Sulpiride compared to WT/Sulpiride). D, Dopamine release and reuptake traces from imaged from 12 wk HD mice. Solid lines denote the average taken from all slices and light shaded bands represent one standard deviation from average behavior. A 1 ms, 0.3 mA stimulation is delivered at time = 0s. E, Representative images of dopamine release imaged in 12 week WT mice before, during, and after stimulated dopamine release in the presence and absence of Sulpiride. F, Representative images of dopamine release imaged in 12 week HD mice before, during, and after stimulated dopamine release in the presence and absence of Sulpiride.

increases the number of dopamine hotspots and the mean peak $\Delta F/F$ of hotspots in 4 week and 12 week slices. Interestingly, the percent increase in dopamine hotspots resulting from sulpiride wash is greater in 12 week slices than in 4 week slices. While expression of dorsal lateral striatal D2-autoreceptors is known to increase and exhibit heightened sensitivity over the course of adolescence in rats, we find the opposite trend in WT R6/2 mice, with 4 week mice exhibiting lower response to sulpiride in comparison to 12 week mice[147]. These differences may be a result of studying dopamine release in response to single stimulations, which contribute minimally to basal dopamine levels on D2Rs, rather than stimulation trains. Notably, the sulpiride-induced modulation of dopamine hotspot peak $\Delta F/F$ measured in the dorsal lateral striatum of R6/2 WT mice is smaller than previously recorded modulations in the dorsal medial striatum of C57BL/6J mice[9]. This finding may indicate geographic differences in dopamine hotspot behavior across the striatum or between mouse lines.

We next examine differences in sulpiride antagonism of D2-autoreceptors in R6/2 HD and WT mice. Intriguingly, R6/2 HD and WT mice showed difference in sulpiride response early in disease at 4 weeks but not late in disease at 12 week. These results suggest changes in D2-autoreceptor function play a role in the early development of Huntington's Disease. Conversely, changes in D2-autoreceptor function may not substantially contribute to the severe change in motor performance observed in R6/2 HD mice. We performed follow-up studies using the data collected in this study to explore if changes in D2-autoreceptor action may be observed in 12 week R6/2 HD mice may manifest through metrics outside of doapmine hotspot number and mean peak $\Delta F/F$. The results of this follow up study are discussed in Chapter 6.

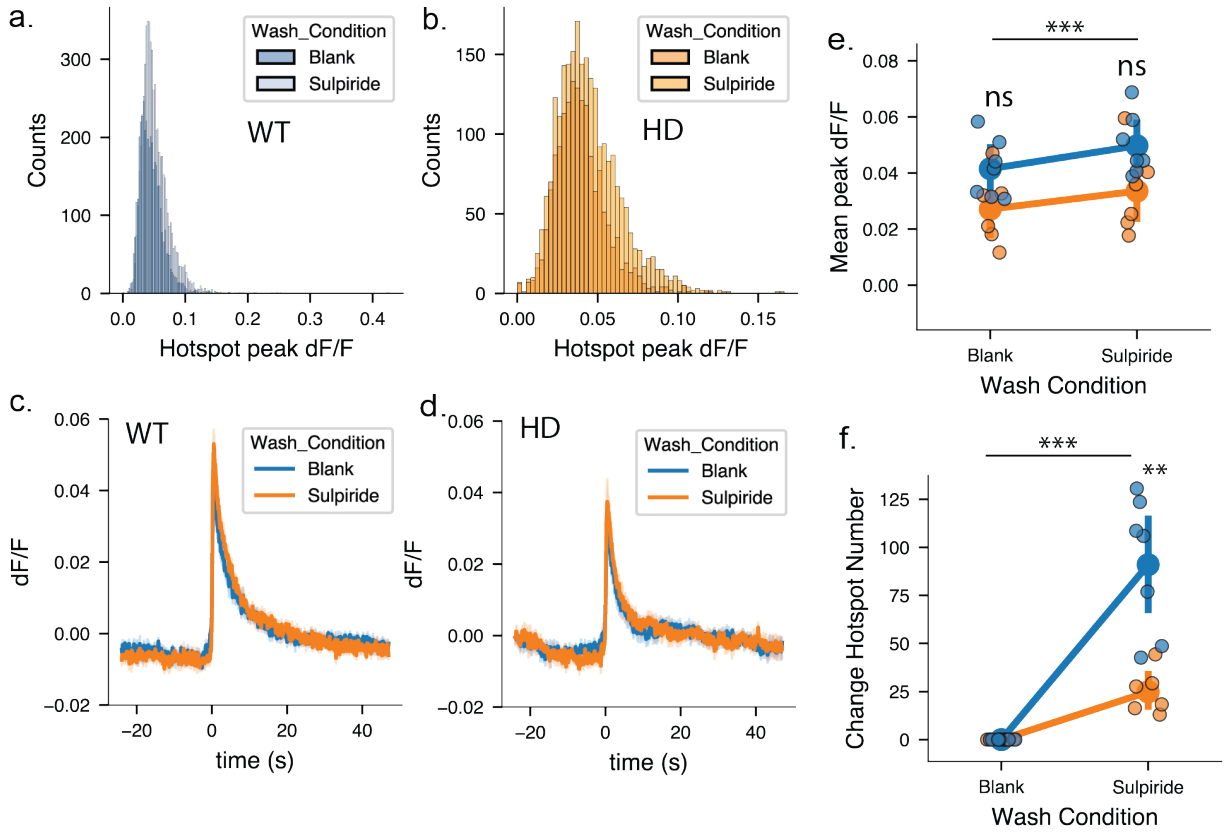

Figure 5.5: Pooled dopamine hotspot histograms and dopamine release and reuptake traces for 12 week R6/2 HD and WT mice after Sulpiride Wash A, Histograms of pooled dopamine hotspots from 12 week WT mic. Dark blue bars show hotspots active before Sulpiride wash, and light blue bars show hotspots active after Sulpiride wash. B. Histograms of pooled dopamine hotspots from 12 week HD mic. Dark orange bars show hotspots active before Sulpiride wash, and light orange bars show hotspots active after Sulpiride wash. C, Dopamine release and reuptake traces from imaged nIRCat-labeled brain slices for 4 week WT mice. Solid lines denote the average taken from all slices and light shaded bands represent one standard deviation from average behavior. A 1 ms, 0.3 mA stimulation is delivered at time = 0s D, Dopamine release and reuptake traces from imaged nIRCat-labeled brain slices for 4 week HD mice. E, The average mean peak $\Delta F/F$ values recorded in 4 week WT and HD slices before and after Sulpiride wash (WT N = 7 slices, 7 animals, HD N = 6 slices, 6 animals; mixed-ANOVA: disease state, p = 0.0465; wash condition, p ¡ 0.0005; interaction, p = 0.314; paired t-test: * p = 0.050 HD/Blank compared to WT/Blank, ns p = 0.059 HD/Sulpiride compared to WT/Sulpiride). F, Total change in hotspots number recorded in 12 week WT and HD slices at 1 mM Ca+2, 2 mM Ca+2, and 4 mM Ca+2 (WT N = 7 slices, 7 animals, HD N = 6 slices, 6 animals; mixed-ANOVA: disease state, p = 0.001; wash condition, p ¡ 0.0005; interaction, p = 0.001; paired t-test: ** p = 0.002 HD/Sulpiride compared to WT/Sulpiride)

5.5 Materials and Methods

5.5.1 Animals

Male B6CBA-Tg(HDexon1)62Gpb/3J mice (R6/2 mice) were purchased from Jackson Labs and bred at 6 weeks with 10 week old female C57BL/6 mice. Pups were weaned and genotyped for the human HD fragment at 3 weeks. Mice were housed at three to five animals per cage with food and water available ad libitum and maintained in a temperature-controlled environment on a 12h dark/light cycle with light-on at 7:00 am and light-off at 7:00 pm. All animal procedures were approved by the University of California Berkeley Animal Care and Use Committee.

5.5.2 nIRCat Nanosensor synthesis and characterization

Dopamine nIRCat nanosensor was synthesized and characterized as described previously described in (Yang et al., 2021). A single walled carbon nanotube (SWNT) slurry was created by combining 1050 mg of hydrated HiPco SWNTs purchased from NanoIntegris with 25 mL of molecular grade water in a 50 mL Falcon Tube and probe sonicating the solution for 2 minutes at 10% amplitude until the slurry is visually distributed. To create nIRCat nanosensors, 100 µl of SWNT slurry was mixed with 1 mg of (GT)6 oligonucleotides purchased from Integrated DNA Technologies (standard desalting) in 100 mM and bath sonicated for 10 minutes (Branson Ultrasonic 1800) followed by 5 minutes of rest at room temperature. The solution was then sonicated on ice for 10 minutes using a probe-tip sonicator (Cole-Parmer Ultrasonic Processor, 3-mm diameter tip, 5 W power) followed by 5 minutes of rest on ice. The sonicated solution was incubated at room temperature for 30 mins and centrifuged at 16,000 g (Eppendorf 5418) for 30 minutes to removed unsuspended SWNT bundles and amorphous carbon. The supernatant is the removed for use and stored at 4°C for 30 minutes before characterization. Final supernatant should be stored at 4°C until use.

Nanosensors are synthesized in 1 mL batches and combined for characterization. Nanosensor concentrations were determined using absorbance at 632 nM with an extinction coefficient of 0.036 (mg/L)-1cm-1. To characterize the visible and nIR absorption spectrum, nanosensors were diluted to a concentration of 5 mg/L in 1x PBA and taken using a UV-VIS-nIRC spectrophotometer (Shimadzu UV-3600 Plus). To test fluorescent response to dopamine administration, each sensor batch is diluted to a working concentration of 5 mg/L in 1x PBS and 198 µl aliquots are made into a 96-well plate and baseline fluorescence is taken using a 20x objective on an inverted Zeiss microscope (Axio Observer D1) coupled to a Princeton Instruments spectrograph (SCT 320) and a liquid nitrogen cooled Princeton Instruments InCaAs linear array detector (PyLoN-IR). Nanosensors were excited using a 721-nm lazer (Opto Engine LLC). After the baseline fluorescence was taken, 2 µl of 10 mM Dopamine in 1xPBS is added and a robust fluorescence response to dopamine was confirmed.

5.5.3 Phenotypic Motor Coordination Assessment

The accelerating Rotarod test and hind limb clasp test were used to evaluate changes in motor coordination in R6/2 and WT mice. For accelerating rotarod tests, mice were placed on a Ugo Basile rotarod for 1 min a 5 rpm to adjust to the apparatus. At the end of the 1 min adjustment period, the speed of the rotarod was increased at a constant rate to a final speed of 40 rpm over 350 s. The trial is terminated after mice either fall off the rod, tumble on the rod for two consecutive rotations, or "max out" the rod speed at 360s. Starting at four weeks, mice are introduced to the rotarod and complete the test for 3 consecutive days, before their rotarod times plateau and performance is recorded on the fourth day. For subsequent weeks, mice complete the rotarod only once a week.

Hind limb clasp tests are conducted by grasping mice at the base of the tail and lifting the mouse off the ground for 10 s. Mice that show splayed out legs are assigned a score of 0, mice that contract one hindlimb are scored at 1, mice contract both hindlimbs are scored at 2, and mice that retract both hindlimbs full and curl into the abdomen are scored at 3.

5.5.4 nIRCat dopamine Imaging

Acute live brain slices were prepared using protocols previously described (Yang et al., 2021). Briefly, mice are deeply anesthetized via intraperitoneal ketamine/xylazine cocktail and perfused transcardially using cold cutting buffer (119 mM NaCl, 26.2 mM NaHCO3, 2.5 mM KCl, 1 mM NaH2PO4,3.5 mM MgCl2, 10 mM glucose, and 0 mM CaCl2). The brain was then rapidly dissected, mounted on a vibratome stage (Leica VT1200 S) using super glue, and cut into 300 µm thick slices containing the dorsal striatum. Slices were then collected and incubated at 37°C for 30 minutes in oxygen saturated ACSF (119 mM NaCl, 26.2 mM NaHCO3, 2.5 mM KCl, 1 mM NaH2PO4, 1.3 mM MgCl2, 10 mM glucose, and 2 mM CaCl2) followed by 30-minute incubation at room temperature. All slices are maintained at room temperature until imaging and used within 6 hours of preparation.

Slices are labeled through passive incubation in 5 ml of ACSF containing nIRCat nanosensor at a concentration of 2 mg/L for 15 minutes. After incubation, the slices is transferred through 3 wells of a 24-well plate containing ACSF to rinse off non-localized nIRCat sensor and then left to rest at room temperature ACSF for 15 minutes before transfer to the 32°C recording chamber. Once placed in the recording chamber, slices equilibrate for 15 minutes during which a tungsten bipolar stimulation electrode is positioned at a field of view in the dorsal-lateral striatum using a 4x objective (Olympus XLFluor 4/ 340). Under a 60x objective the electrode is moved 200 µm away from the selected field of view and brought into contact with the surface of the brain slice. In all experiments, 600 total images are acquired into an image-stack at a rate of 9 frames per second. A single stimulation of 0.1 mA or 0.3 mA is applied after 200 frames of baseline are collected. Videos of stimulation at each strength are collected in triplicate and stimulation strengths are alternated. All slices are given 5 minutes between each stimulation with the excitation laser path shuttered. Prior

to stimulation, the laser is un-shuttered for 1 minutes.

5.5.5 nIRCat Imaging Calcium Wash and Sulpiride wash

To image nIRCat-labeled acute brains slices at multiple extracellular calcium concentrations, buffers were prepared at three calcium concentrations: 1 mM Low Calcium Buffer (119 mM NaCl, 26.2 mM NaHCO3, 2.5 mM KCl, 1 mM NaH2PO4, 1.3 mM MgCl2, 10 mM glucose, and 1 mM CaCl2), 2 mM Normal Calcium Buffer (119 mM NaCl, 26.2 mM NaHCO3, 2.5 mM KCl, 1 mM NaH2PO4, 1.3 mM MgCl2, 10 mM glucose, and 2 mM CaCl2), 4 mM High Calcium Buffer (119 mM NaCl, 26.2 mM NaHCO3, 2.5 mM KCl, 1 mM NaH2PO4, 1.3 mM MgCl2, 10 mM glucose, and 4 mM CaCl2). Following stimulation in 2 mM Normal Calcium Buffer, 4 mM High Calcium buffer was flowed into the imaging chamber for 15 minutes (Full bath turnover in 3 minutes). After buffer transfer, the slice was stimulated at 0.1 mA and 0.3 mA in triplicate as described for 2 mM Normal Calcium Buffer. Buffer was then exchanged again to 1 mM Low Calcium Buffer via 15-minute wash and the slice was stimulated at 0.1 mA and 0.3 mA in triplicate.

To nIRCat image acute brain slices in the presence of the D2-antagonist Sulpiride, S-Sulpiride was dissolved in sterile DMSO and frozen in 100 µl aliquots at -20°C. Prior to use, single aliquots are thawed and added to 100 mL of ACSF to produce a 10 µM Sulpiride solution. Acute brain slices were stimulated at 0.1 mA and 0.3 mA in triplicate in sulpiride-free ACSF. Sulpiride solution was flowed into the imagine chamber for 15 minutes before stimulating the slice at 0.1 mA and 0.3 mA in triplicate.

5.5.6 Image Stack Processing and Data Analysis of nIRCat Data

Raw Image stack files are processed using a custom-built, publicly available MATLAB program (https://github.com/jtdbod/Nanosensor-Imaging-App). Image processing procedures are described in depth in Yang, del Bonis O'Donnel et al and briefly summarized here. Regions of dopamine release are identified by large changes in nIRCat $\Delta F/F$ response. To minimize bias and improve stack processing time, regions of high $\Delta F/F$ response (dopamine hotspots) were identified by defining a grid of 2 µm squares across the field of view. For each grid square $\Delta F/F$ was calculated using the formula (F- F0) /F0, where F0 is defined by the average fluorescence of the grid square over the first 30 frames of the image stack and F is the fluorescence intensity of the gird square as it changes over the 600 collected frames. Grid squares are identified as regions of interest if they exhibit behavior that is 3 standard deviations above the baseline F0 activity around time of stimulation (200 frames).

Dopamine hotspots were identified for each stimulation replicate image stack taken at a given field-of-view on a brain slice. The peak $\Delta F/F$ of each dopamine hotspot in the image stack were averaged to give the average image stack peak $\Delta F/F$. The average image stack peak $\Delta F/F$ from the three stimulation replicates were then average to give the slice average

peak ΔF/F. Similarly, the number of dopamine hotspots identified from each stimulation replicate image stack were averaged to give the slice average hotspot number. Mean dopamine release and reuptake traces are produced by averaging the average traces from each slice (3 stimulations per slice, 1 slice per animal). Percent change in hotspots was calculated as (number hotspots wash - number hotspots 2 mM Ca^{+2})/ (number hotspots 2 mM Ca^{+2}), whereas change in hotspots number was calculated as (number hotspots wash - number hotspots 2 mM Ca^{+2}).

To track hotspot fidelity, each initially defined grid square was assigned a unique position number, allowing the position of each identified dopamine hotspot within an image stack to be recorded. For a set of triplicate image stacks, an array of all unique hotspots active across the stimulation replicates was generated. Then python code was used to analyze whether each unique hotspot was active in each stimulation replicate. The number of stimulations a unique hotspot was active in was summed across the three replicates and assigned as the dopamine release fidelity (e.g. hotspot '12' is active in 2 out of 3 stimulations and is assigned release fidelity 2). The same procedure was used to identify the dopamine release fidelity of hotspots active after drug wash. Hotspots were then separated into three groups: hotspots that are active both before and after drug wash (shared hotspots), hotspots that become active after drug wash (added hotspots), and hotspots that are only active before drug wash. For shared hotspots modulation in hotspot release strength was calculated as the difference in peak ΔF/F of the unique hotspot before and after drug wash, (mean ΔF/F)post - (mean ΔF/F)pre , where (mean ΔF/F)pre is the average peak ΔF/F of each unique dopamine hotspot across the three stimulations before drug wash and (mean ΔF/F)post is the average peak ΔF/F of each unique dopamine hotspot across the three stimulations after drug wash. For hotspots active only after drug wash, there is no corresponding "pre drug wash" ΔF/F. Therefore, the difference in peak ΔF/F was calculated through (mean ΔF/F)post - (mean ΔF/F)pre, shared, where (mean ΔF/F)post represents the average peak ΔF/F of the unique dopamine hotspot active after sulpiride wash across three stimulations and (mean ΔF/F)pre, shared is the average of all the shared hotspots' mean ΔF/F from the slice before drug wash.

5.5.7 Exerimental Design and Statistical Analysis

All nIRCat Imaging data were processed using a custom-built, publicly available MATLAB program (https://github.com/jtdbod/Nanosensor-Imaging-App). Statistical analyses were conducted using the open-source statistical python package pingouin. All bar graphs show the mean with error bars denoting the 95% confidence interval. All single data points correspond to a single slice taken from an animal. Data comparing two variables was analyzed using a mixed-ANOVA with wash condition as the within-subject factor (e.g.sulpiride, blank, calcium concentration) and disease state as the between-subject factor (eg. HD, WT). Paired t-tests were used a post-hoc tests if mixed-ANOVA analyses indicated significant differences. Data comparing two values of one variable were analyzed using tukey's t-test. Group sizes were determined based on previous literature (Adil et al., 2018). Changes in histogram skew were computed through pooling of all hotspots identified across all mice within the disease

and wash condition and evaluated using a permutation test using the test statistic μ = skew(post wash) – skew(pre-wash).

Chapter 6

Changes in dopamine hotspot release fidelity in R6/2 Huntington's Disease Model Mice [vi]

[vi]This section is produced in part with permission from the following work: Yang, S. J., et al. "Synaptic scale dopamine disruption in Huntington's Disease model mice imaged with near-infrared catecholamine nanosensors."

6.1 Abstract

Striatal dopamine signaling relies on the spatial and temporal precision of dopamine release to coordinate information from multiple neuronal inputs. This process is dynamic, with dopamine release occurring with some probability upon the arrival of an electrical stimulus. Measuring the release probability of a dopamine release site has been historically challenging due to lack of tools that enable direct visualization of dopamine release from individual release sites. To this end, we demonstrate the use of nIRCat imaging to simultaneously track dopamine release hotspots in *ex vivo* brain slices over the course of up to 10 successive stimulations from a tungsten electrode. This allows for the measurement of the number of successful dopamine release events within a given number of stimulations, a metric we term release fidelity. We also take advantage of nIRCat's pharmacological compatibility to show that dopamine release is increased by D2-autoreceptor antagonism by Sulpiride, as a result of the addition of new dopamine hotspots as well as the promotion of lower fidelity hotspots to higher fidelity release states. This ability to raise hotspots to high fidelity release states is compromised in 12 week R6/2 HD slices, suggesting that the timing of dopamine release is compromised late in HD. Lastly, we show that dopamine hotspot fidelity cannot be rescued through direct blockage of the Kv1.2 channels using 4-AP to bypass of D2-autoreceptor activation. These findings implicate Kv1.2 channel disruption in altered dopamine signaling late in HD and may offer a new therapeutic target for the treatment of Huntington's Disease.

6.2 Introduction

Efficient information transfer between neurons relies on both precise spatial positioning of presynaptic terminals and precise temporal release of signaling molecules. Within the striatum, this complex spatio-temporal dynamic forms the backbone of signaling for learning, motivation, voluntary movement[21]. In Chapter 3 I demonstrate how the spatial resolution of nIRCat imaging gives insights into how efficiently dopamine release is able to cover the dorsal lateral striatum. Building on these insights, we next sought to see if nIRCat imaging could also be used to explore how dopamine release may be temporally altered over the course of Huntington's Disease.

Foundational theory on neurotransmitter release behavior from single release sites was developed by Castillo and Katz in a landmark work exploring spontaneous synaptic potentials in the frog neuromuscular junction[126]. Castillo and Katz hypothesized that the strength of a synaptic connection is determined by the number of synaptic contacts a presynaptic neuron makes on a postsynaptic neurons, the size of postsynaptic depolarization caused by the neurotransmitter released from a single synaptic vesicle (quantal size), and the probability of presynaptic neurotransmitter release in response to stimulus (release probability). The imperfect correlation between stimulus and neurotransmitter release is the result of the stochasticity of the biological processes that result in synaptic vesicle fusion at the presynaptic membrane[148;149]. These include presynaptic calcium handling and D2-autoreceptor

regulations as discussed in Chapter 4 and Chapter 5.

Directly observing and measuring release probability for neurotransmitters remains an unresolved challenge within the field of neuroscience. Quantal analysis is a classical method of measuring release probability where data on neurotransmitter release between pre and post synaptic pair of cells can be fit using a binomial-model to extract quantal parameters such as release probability. Collecting a sufficiently large dataset for quantal analysis require long and stable electrophysiological recordings that must be collected one pair at a time. These experiments are often technically challenging and do not allow direct observation of neurotransmitter release. Release probability can also be determined through the frequency of failures method, where the number of successful neurotransmitter release events is counted within a set number of stimulations. Initial studies utilizing the frequency of failures method and electrophysiological recordings were only able to roughly estimate the overall probability of release. This is due to the fact that failure rate is shaped by both the probability of release and the number of release sites. Electrophysiology's inability to distinguish the number individual release sites active during a stimulation renders it unable to measure the exact probability of release. Use of synaptic imaging methods such as FM dyes and pHluorins that are able to visualize exocytotic events at release sites overcomes this technical barrier, allowing direct measurement of release probability through the frequency of failures method[150].

We build upon this growing toolbox of imaging tools for direct release probability measurement by developing an experimental method utilizing nIRCat to measure the probability of dopamine release. Measuring the release probability of neuromodulators presents a unique set of challenges that build upon existing challenges in measuring the release probability of neurotransmitters. Quantal analysis is not readily developed for studying neuromodulator release as many neuromodulators do not form specified synaptic connections and neuromodulator release and binding does not result in a direct change in electrical properties. As such, the electrophysiological recordings traditionally used in quantal analysis cannot be established for the detection of neuromodulator release. Fast scan cyclic voltammetry can in be used to detect dopamine release, but is not able to distinguish dopamine release from single release sites. Given that individual release sites are tuned to have varying probabilities of release and that this diversity is paramount to the integration of neuronal inputs, FSCV's lack of spatial resolution is a major technical challenge in measuring the release probability of single release sites. In this light, the use of nIRCat imaging to directly visualize dopamine release from single release sites offers a unique opportunity to directly measure release probability at multiple release sites via the frequency of failures method. This method not only provides the ability to directly measure dopamine release, but also permits the simultaneous tracking of multiple release sites within one field of view, significantly increasing the rate of data collection. In this chapter, I demonstrate how this powerful application of nIRCat imaging can be used to characterize the release probability of dopamine hotspots in R6/2 WT brain slices in blank ACSF as well as in the presence of pharmacology documented to act upon molecular pathways that influence release probability. I then explore how the probability of dopamine hotspots in R6/2 WT brain slices is altered in late Huntington's Disease and identify potential molecular origins for this disruption using dopamine pharma-

cology. Altogether, this work showcases how nIRCat's high spatio-temporal resolution and pharmacological compatibility synergistically combine to reveal new insights in the technically challenging field of measuring neuromodulator release probability.

6.3 Results and Discussion

6.3.1 Initial Approaches Towards Quantifying Dopamine Hotspot Release Fidelity

The coverage of dopamine signaling across the striatum is influenced not only by hotspot number and peak $\Delta F/F$, but also the fidelity of hotspot release. Here we term "hotspot release fidelity" as the ability of the same dopamine hotspot to fire upon repeated stimulations. To explore hotspot release fidelity, we utilized our ability to track individual dopamine hotspots across stimulations and recorded the number of stimulations out of three total that each hotspot was active (Fig.6.1a). As such, hotspots that responded in all three stimulations were assigned a hotspot release fidelity of 3, while hotspots responsive in only one of three stimulations were assigned a hotspot release fidelity of 1. We then pooled all hotspots identified across 7 WT slices and 6 HD slices at 12 weeks and examined the distribution of hotspots across the three hotspot release fidelities before and after Sulpiride wash. As noted previously in Chapter 5, Sulpiride can modulate dopamine release through increasing the number of dopamine hotspots or modulating the activity of existing hotspots. Therefore, we separated hotspots into those that are active before and after sulpiride wash ("shared hotspots") and those that emerge after Sulpiride wash ("added hotspots").

Before sulpiride wash, WT 12 week mice show an even distribution of dopamine hotspots across fidelities. This distribution shifts following sulpiride wash, resulting in an increase in the percentage of high release fidelity 3 hotspots from 31.0% of all dopamine hotspots to 66.6% of all hotspots (pairwise tukey: ** $p = 0.0016$) (Fig.6.1b). In contrast, high release fidelity 3 hotspots represent 23.7% less of the of total dopamine hotspot population (pairwise tukey: * $p = 0.0137$) in HD 12 week mice compared to WT 12 week mice. Furthermore, 12 week HD slices do not show a significant increase in fidelity 3 dopamine hotspots after sulpiride wash (pairwise tukey: $p = 0.197$) (Fig.6.1c). Given that the number and identity of the shared hotspots is held constant before and after sulpiride wash, increases in high release fidelity 3 hotspots in response to sulpiride wash is driven by lower release fidelity hotspots transitioning into high release fidelity 3 hotspots. These findings are consistent with hypotheses that altered signaling through the D2-autoreceptor may alter voltage sensitivity of 4-amino-pyradine (4-AP) sensitive K^{+1} channels such as Kv1.2 to shape the responsiveness of dopamine release[151]. We also examined whether a dopamine hotspot initial release fidelity in the absence of sulpiride changed its modulation in peak dopamine $\Delta F/F$ following sulpiride wash. Strikingly, we observed consistent modulation in dopamine hotspot peak $\Delta F/F$ regardless of initial release fidelity in both WT and HD slices, which suggests increases in fidelity are not a result of increased dopamine release leading to more consistent

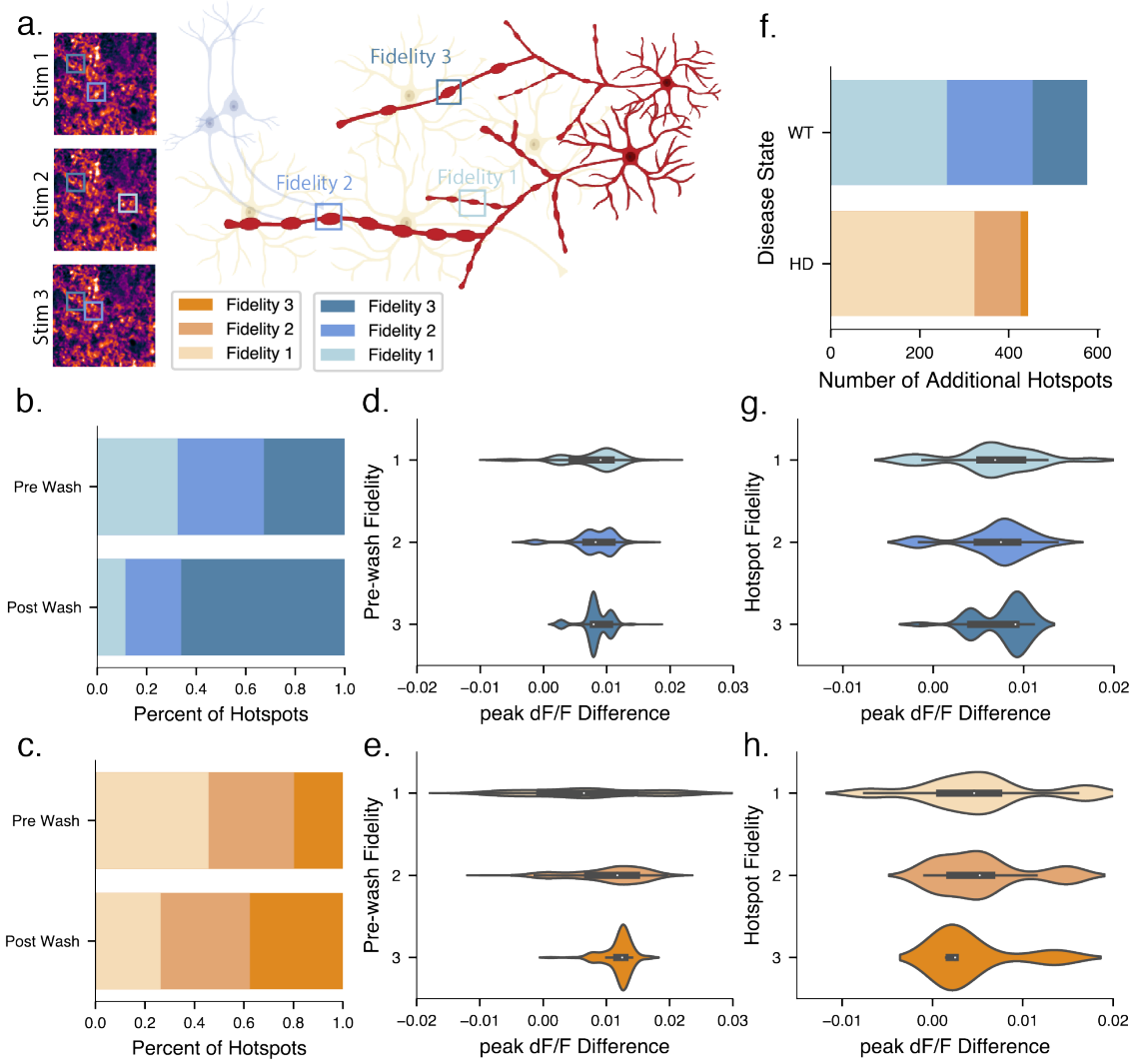

Figure 6.1: Sulpiride promotes increased firing fidelity of ΔF/F dopamine hotspots in both R6/2 HD and WT mice A. Graphical overview of how individual dopamine hotspots can be tracked across stimulation replicates and assigned fidelity scores based on the number of stimulations that are active in. B. Stacked bar plot showing the distribution of shared dopamine hotspots active both before and after Sulpiride wash in WT 12 week mice (3836 dopamine hotspots total, pooled from 7 slices from 7 animals). Before Sulpiride wash 12 week WT dopamine hotspots are even distribution across fidelity scores (dark blue: fidelity 3, mid blue: fidelity 2, light blue: fidelity 1). After Sulpiride wash, fidelity 3 dopamine hotspots increase from making up 32.7% of all dopamine hotspots to 66.1% of all hotspots (pairwise tukey: ** p = 0.002). This is paired with a decrease in fidelity 2 and fidelity 1 hotspots. C. Stacked bar plot showing the distribution of dopamine hotspots active both before and after Sulpiride wash in HD 12 week mice (1094 dopamine hotspots total, pooled from 6 slices from 6 animals). Before Sulpiride wash the majority of 12 week HD dopamine hotspots are fidelity 1 hotspots. (dark orange: fidelity 3, mid orange: fidelity 2, light orange: fidelity 1). Compared to fidelity 3 hotspots in WT slices, fidelity 3 hotspots in HD slices make up 13.0% less of the total dopamine hotspot population (pairwise tukey: * p = 0.035). (Continued on the following page.)

Figure 6.1: (continued) After Sulpiride wash, 12 week HD slices do not show a significant increase in fidelity 3 dopamine hotspots (pairwise tukey: p = 0.308). D. Stacked violin plot showing the increase in dopamine hotspots mean peak ΔF/F after Sulpiride wash of WT dopamine hotspots active before and after Sulpiride wash. Values are sorted by the initial fidelity exhibited by the dopamine hotspot pre-Sulpiride wash. E. Stacked violin plot showing the increase in hotspots mean peak ΔF/F after Sulpiride wash of HD dopamine hotspots active before and after Sulpiride wash. Values are sorted by the initial fidelity exhibited by the dopamine hotspot pre-Sulpiride wash. F. Stacked bar plot showing the number of dopamine hotspots added by in WT and HD slices after Sulpiride wash. WT and HD Slices add a comparable number of dopamine hotspots after Sulpiride wash (pairwise tukey: p = 0.548). However, fidelity 3 hotspots make up a significantly higher percentage of added hotspots in WT slices compared to HD slices (pairwise tukey: * p = 0.004). G. Stacked violin plot showing the increase in hotspot mean peak ΔF/F after Sulpiride wash of WT dopamine hotspots added after Sulpiride wash compared to the average mean peak ΔF/F of all hotspots active before Sulpiride wash. Values are sorted by the fidelity exhibited by the dopamine hotspot after it appears following Sulpiride wash. H, Stacked violin plot showing the increase in hotspot mean peak ΔF/F after Sulpiride wash of HD dopamine hotspots added after Sulpiride wash compared to the average mean peak ΔF/F of all hotspots active before Sulpiride wash. Values are sorted by the fidelity exhibited by the dopamine hotspot after it appears following Sulpiride wash.

detection and that mechanisms leading to increase fidelity are separate from those that increase peak ΔF/F (Fig.6.1d,e). We next examined the activity of hotspots added after Sulpiride wash. Interestingly, when controlling for the unique identity of dopamine hotspots, we found that WT and HD slices add comparable number of dopamine hotspots after Sulpiride wash (pairwise tukey: p = 0.836) (Fig.6.1f). However, release fidelity 3 and release fidelity 2 hotspots make up 13.7% more and 10.7% more of the population of added dopamine hotspots in WT slices in comparison to the dopamine hotspots added in HD slices. As such, reduced transition of dopamine hotspots to higher fidelity release states combined with decreased addition of higher fidelity dopamine release hotspots ultimately results in fewer hotspots active in HD slices during a given stimulation.

Furthermore, while the fidelity of dopamine hotspots is significantly changed between WT and HD mice over the course of disease, changes in the peak dopamine ΔF/F of hotspots are comparatively mild even late in disease at 12 weeks. Together, these results suggest that altered dopamine release in HD is characterized by degeneration of dopamine release processes such that spatial coverage of active dopamine hotspots across the striatum is reduced. Though exposing late disease HD slices at 12 weeks to high extracellular calcium concentrations or sulpiride indicates that additional dopamine hotspots can be engaged via molecular rescue, full rescue of dopamine signaling likely necessitates intervention at earlier HD timepoints.

6.3.2 Advanced Approaches Towards Quantifying Dopamine Hotspot Release Fidelity

D2-autoreceptor action on the voltage gated K^{+1} channel Kv1.2 plays a critical role in facilitating D2-autoreceptor mediated regulation of axonal dopamine release[151]. Kv1.2 is the most abundant K_v subunit in the mammalian brain and blocking Kv1.2 activity through 4-AP has been shown to counteract the ability of quinpirole to decrease FSCV detected dopamine overflow[151]. To assess whether the observed reduction in HD slice response to sulpiride D2-autoreceptor antagonism at 12 week is driven by disruptions in D2-autoreceptor action on Kv1.2 channels or significant downregulation of D2-autoreceptors in the Striatum as a response to the dopamine depletion in late HD, we co-washed sulpiride and the broad spectrum Kv1 channel family blocker 4-aminopyradine (4-AP) on slices to see if direct blockade of Kv1.2 could further increase dopamine release from HD slices. We also increase the number of stimulation replicates from 3 to 10 to capture a wider view of how dopamine hotspots fidelity shifts with pharmacological action.

As anticipated, WT slices showed a progressive increase in number of dopamine hotspots following initial Sulpiride wash and subsequent Sulpiride and 4-AP co-wash (Fig.6.2a,b). This increase is in part facilitated through the promotion of lower release fidelity hotspots to higher release fidelity states, resulting in a progressive shift in the distribution of WT dopamine hotspots from skewing heavily towards low fidelity states to more even distributions following Sulpiride and 4-AP drug wash (Fig.6.2d). Intriguingly, while HD slices show an increase in dopamine hotspots and high-fidelity dopamine hotspot after 10 µM sulpiride wash, co-wash of Sulpiride and 4-AP decreases the number of dopamine hotspots and high-fidelity dopamine hotspots (Fig.6.2a,b). This unexpected effect is not the result in decreased mean peak $\Delta F/F$ of R6/2 HD dopamine hotspots compared to WT dopamine hotspots (Fig.6.2c).

Altogether, these findings point suggest that altered dopamine release in late HD is not driven by D2-autoreceptor downregulation alone. Rather, the ability of Kv1.2 channels to drive dopamine release may be compromised. We hypothesize may be due to altered scaffolding of Kv1.2 channels at the dopaminergic bouton or impairment of Kv1.2 function. Alternatively, Kv1.2 channels may be overactive in R6/2 HD dopamine hotspots, driving increased spontaneous release that drains already diminished dopamine stores. This activity would reduce the ability of R6/2 HD dopamine hotspots to continue releasing dopamine upon successive stimulations, shifting the hotspot fidelity histogram towards primarily lower fidelity hotspots. We note that studies in have shown 4-AP also has the ability to increase dopamine release through a second pathway outside of action on K_v channels where it facilitates the opening of voltage gated Ca^{+2} channels to increase dopamine overflow[51;151]. The increased extracellular Ca^{+2} sensitivity we observe in HD slices at 12 weeks described in Chapter 4 suggests that direction action on voltage gated Ca^{+2} channels should increase dopamine hotspot number and mean peak $\Delta F/F$ in HD slices. Therefore, 4-AP facilitated opening of voltage gated Ca^{+2} channels does not account for the observed decrease in dopamine release in HD slices.

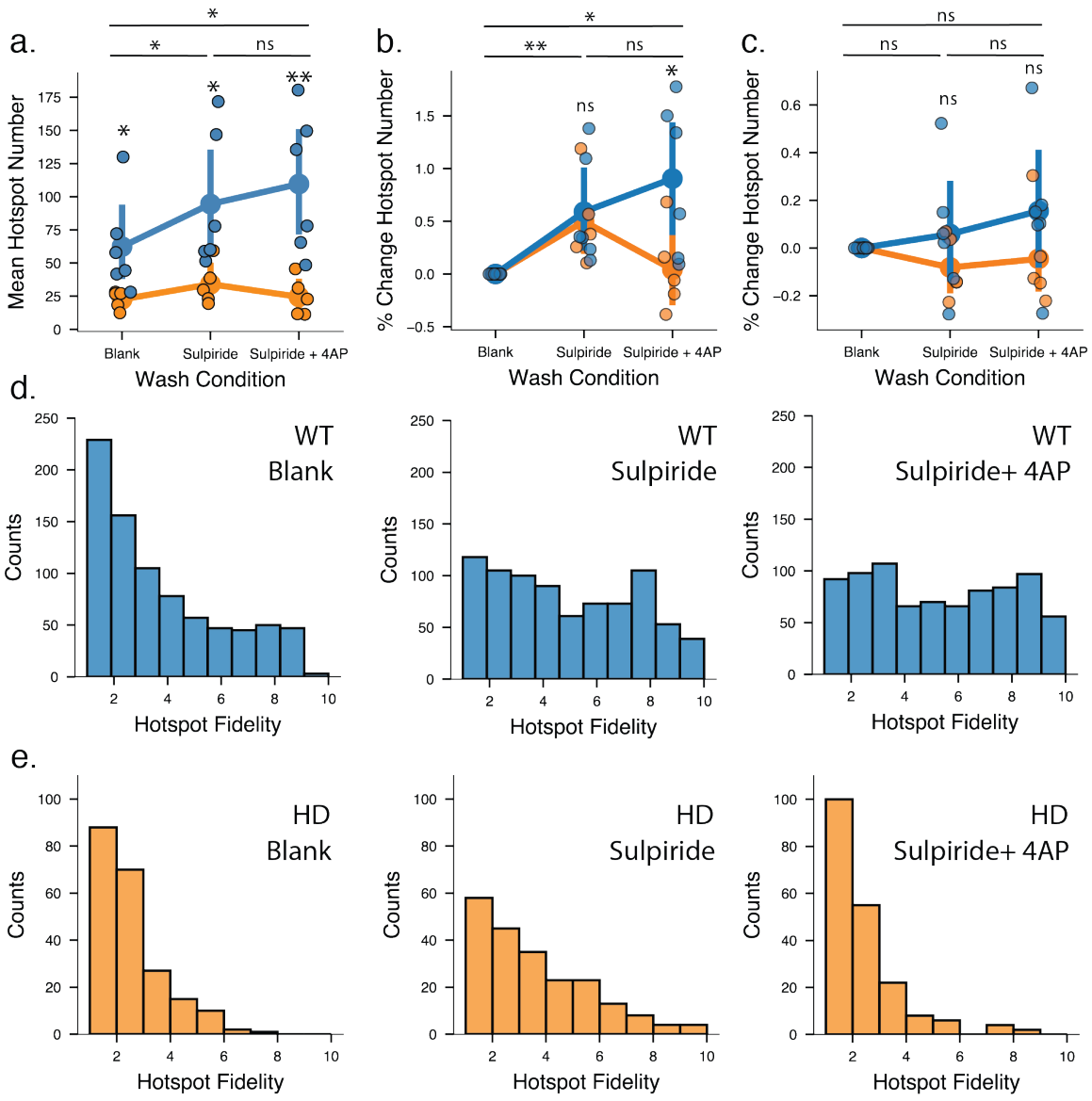

Figure 6.2: Sulpiride and 4-Aminopyridine (4-AP) co-wash increases dopamine hotspot fidelity in WT slices but decreases dopamine hotspot fidelity in HD slices A. WT slices show a significant increase in the number of active dopamine hotspots over the course of progressive Sulpiride and 4-AP Wash. In contrast, HD mice show an increase in dopamine hotspots after sulpiride wash followed by a decrease in dopamine hotspots after 4-AP co-wash. (WT N = 6 slices, 6 animals HD N = 5 slices, 5 animals ; mixed-ANOVA: disease state, *p = 0.014; wash condition, ** p = 0.006; interaction, *p = 0.029; paired t-test: * p = 0.043 HD/Blank to WT/Blank, * p ¡ 0.034 HD/Sulpiride to WT/Sulpiride, ** p ¡ 0.001 HD/Sulpiride+4AP to WT/Sulpiride+4AP) B. WT and HD slices show comparable percent increase in dopamine hotspots after Sulpiride wash. However, HD slices show a striking departure in response after Sulpiride and 4-AP co-wash characterized by a decrease in dopamine hotspot number (mixed-ANOVA: disease state, p = 0.156; wash condition, ** p = 0.003; interaction, *p = 0.020; paired t-test: p = 0.756 HD/Sulpiride to WT/Sulpiride, *p = 0.038 HD/Sulpiride+4AP to WT/Sulpiride+4AP) (Continued on the following page.)

Figure 6.2: (continued) C. WT and HD slices show comparable percentx increase in mean peak dF/F after progressive Sulpiride and 4-AP wash (mixed-ANOVA: disease state, p = 0.264 wash condition, ** p = 0.492; interaction, *p = 0.293; paired t-test: p = 0.299 HD/Sulpiride to WT/Sulpiride, p = 0.226 HD/Sulpiride+4AP to WT/Sulpiride+4AP) D. Histograms of pooled dopamine hotspots from all WT slices show that in blank ACSF dopamine hotspot distribution is skewed towards low release fidelity. Followed Sulpiride wash, dopamine hotspots increase in release fidelity, resulting in a more even distribution. This is further increased by Sulpiride and 4-AP co-wash. (permutation test on skew(post wash) – skew(pre-wash): statistic = -0.603 *** p ¡ 0.0005 Blank/Sulpiride, statistic = -0.130 * p = 0.045 Sulpiride + 4AP/Sulpiride) E. Histograms of pooled dopamine hotspots from all HD slices show that in blank ACSF dopamine hotspot distribution is skewed towards low release fidelity. Followed Sulpiride wash, dopamine hotspots increase in release fidelity, resulting in a more even distribution. However, this increase in release fidelity is lost after Sulpiride and 4-AP co-wash. (permutation test on skew(post wash) – skew(pre-wash): statistic = -0.364 p = 0.085 Blank/Sulpiride, statistic = 1.2 ** p 1.0 Sulpiride + 4AP/Sulpiride)

6.4 Conclusions

D2-autoreceptors expressed on dopaminergic boutons play an active role in regulating dopamine release by initiating molecular events within the active boutons themselves. While expression and transcription of striatal D2 receptors is decreased in both HD patients and R6/2 mice, isolation of D2-autoreceptor behavior from dopamine receptors on neighboring cells remains challenging (Ariano et al., 2002; Vashishtha et al., 2013). In this work we utilize nIRCat's pharmacological compatibility and ability to track individual dopamine hotspots to study the effect of the D2R antagonist Sulpiride and the Kv1.2 blocker 4-AP at the level of dopamine hotspots. These experiments underscore the pharmacological versatility of nIRCat and bring to light new insights into how these small molecule drugs affect dopamine release and how these effects are altered during Huntington's Disease.

In Chapter 5 we demonstrated that Sulpiride antagonism of D2-autoreceptors drives an increase in dopamine hotspot number and mean peak $\Delta F/F$, and that this increase is comparable in R6/2 HD and WT mice. In this work, we explore the effect of Sulpiride antagonsim of D2-autoreceptors further by re-analyzing the Sulpiride wash dataset to examine how Sulpiride changes dopamine hotspot fidelity over triplicate stimulation. In WT slices, Sulpiride antagonism of D2-autoreceptors shifts dopamine hotspots to higher release fidelities and promotes the activation of previously inactive high-fidelity dopamine hotspots. We find that high release fidelity dopamine hotspots comprise of 31% of all detected dopamine hotspots in WT slices, which stand in marked agreement with findings that only 20% of dopamine varicosities release dopamine and only 30% of dopamine varicosities are equipped with fast release, active zone-like machinery (Pereira et al., 2016; Liu et al., 2018). In contrast, dopamine hotspots from R6/2 HD slices show diminished ability to convert dopamine hotspots into higher release fidelities. Sulpiride wash also adds fewer high fidelity dopamine hotspots in R6/2 HD slices in comparison to their WT counterparts, further attenuating R6/2 HD slice's ability to mobilize dopamine. These findings show that fully understanding

dopamine dysfunction during HD will require not only spatially resolving where release is occurring, but also temporally resolving when it occurs over multiple release events.

Decreases in dopamine hotspot release fidelity modulation by Sulpiride may be the result of disruption in the ability of D2-autoreceptors to work through Kv1.2 channel pathways or down-regulation of D2R autoreceptor expression and pathways. To test these hypotheses, we examined co-wash of Sulpiride and the Kv1.2 channel blocker 4-AP on R6/2 HD and WT brain slices over the course of 10 successive stimulations. We provide compelling evidence for disrupted Kv1.2 channel activity, showing that cowash of Sulpiride and 4-AP shifts the distribution of dopamine hotspots from primarily low-fidelity hotspots towards high-fidelity hotspots in WT mice but not R6/2 HD mice. Instead, co-wash of sulpiride and 4-AP in R6/2 HD mice results in a decrease in the number of active dopamine hotspots, driven from a shift of hotspots towards low-fidelity release states. These findings implicate Kv1.2 channels as playing a role in HD driven neurodegeneration and as a potential target for therapeutic development. Future work may seek to identify when Kv1.2 channel dysfunction begins, and elucidate whether early changes in Kv1.2 channel may drive alterations in R6/2 HD brain function that manifest late in disease.

The analytical framework established in this work for studying changes in dopamine release fidelity offers a powerful lens to turn towards new questions and applications. Adaptation of this method to study dopamine release fidelity from single axons via channel rhodopsin stimulation would allow direct measurement of dopamine release probability from multiple dopamine release sites simultaneously. This ability to directly measure release probability at large scales presents a unique opportunity to visualize the previously hidden process of dopamine mobilization across the striatum. These studies may be extended to study how dopamine mobilization changes during the course of Huntington's Disease, Parkinson's Disease, or other neurodegenerative disease. Alternatively, dopamine fidelity changes can be studied over the course of adolescence or learning to understand how changes in dopamine mobilization become encoded and shape behavior.

6.5 Materials and Methods

6.5.1 Animals

Male B6CBA-Tg(HDexon1)62Gpb/3J mice (R6/2 mice) were purchased from Jackson Labs and bred at 6 weeks with 10 week old female C57BL/6 mice. Pups were weaned and genotyped for the human HD fragment at 3 weeks. Mice were housed at three to five animals per cage with food and water available ad libitum and maintained in a temperature-controlled environment on a 12h dark/light cycle with light-on at 7:00 am and light-off at 7:00 pm. All animal procedures were approved by the University of California Berkeley Animal Care and Use Committee.

6.5.2 nIRCat Nanosensor synthesis and characterization

Dopamine nIRCat nanosensor was synthesized and characterized as described previously described in (Yang et al., 2021). A single walled carbon nanotube (SWNT) slurry was created by combining 1050 mg of hydrated HiPco SWNTs purchased from NanoIntegris with 25 mL of molecular grade water in a 50 mL Falcon Tube and probe sonicating the solution for 2 minutes at 10% amplitude until the slurry is visually distributed. To create nIRCat nanosensors, 100 µl of SWNT slurry was mixed with 1 mg of (GT)6 oligonucleotides purchased from Integrated DNA Technologies (standard desalting) in 100 mM and bath sonicated for 10 minutes (Branson Ultrasonic 1800) followed by 5 minutes of rest at room temperature. The solution was then sonicated on ice for 10 minutes using a probe-tip sonicator (Cole-Parmer Ultrasonic Processor, 3-mm diameter tip, 5 W power) followed by 5 minutes of rest on ice. The sonicated solution was incubated at room temperature for 30 mins and centrifuged at 16,000 g (Eppendorf 5418) for 30 minutes to removed unsuspended SWNT bundles and amorphous carbon. The supernatant is the removed for use and stored at 4°C for 30 minutes before characterization. Final supernatant should be stored at 4°C until use.

Nanosensors are synthesized in 1 mL batches and combined for characterization. Nanosensor concentrations were determined using absorbance at 632 nM with an extinction coefficient of 0.036 (mg/L)-1cm-1. To characterize the visible and nIR absorption spectrum, nanosensors were diluted to a concentration of 5 mg/L in 1x PBA and taken using a UV-VIS-nIRC spectrophotometer (Shimadzu UV-3600 Plus). To test fluorescent response to dopamine administration, each sensor batch is diluted to a working concentration of 5 mg/L in 1x PBS and 198 µl aliquots are made into a 96-well plate and baseline fluorescence is taken using a 20x objective on an inverted Zeiss microscope (Axio Observer D1) coupled to a Princeton Instruments spectrograph (SCT 320) and a liquid nitrogen cooled Princeton Instruments InCaAs linear array detector (PyLoN-IR). Nanosensors were excited using a 721-nm lazer (Opto Engine LLC). After the baseline fluorescence was taken, 2 µl of 10 mM Dopamine in 1xPBS is added and a robust fluorescence response to dopamine was confirmed.

6.5.3 Phenotypic Motor Coordination Assessment

The accelerating Rotarod test and hind limb clasp test were used to evaluate changes in motor coordination in R6/2 and WT mice. For accelerating rotarod tests, mice were placed on a Ugo Basile rotarod for 1 min a 5 rpm to adjust to the apparatus. At the end of the 1 min adjustment period, the speed of the rotarod was increased at a constant rate to a final speed of 40 rpm over 350 s. The trial is terminated after mice either fall off the rod, tumble on the rod for two consecutive rotations, or "max out" the rod speed at 360s. Starting at four weeks, mice are introduced to the rotarod and complete the test for 3 consecutive days, before their rotarod times plateau and performance is recorded on the fourth day. For subsequent weeks, mice complete the rotarod only once a week.

Hind limb clasp tests are conducted by grasping mice at the base of the tail and lifting the mouse off the ground for 10 s. Mice that show splayed out legs are assigned a score of 0, mice that contract one hindlimb are scored at 1, mice contract both hindlimbs are scored at 2, and mice that retract both hindlimbs fully and curl into the abdomen are scored at 3.

6.5.4 nIRCat dopamine Imaging

Acute live brain slices were prepared using protocols previously described (Yang et al., 2021). Briefly, mice are deeply anesthetized via intraperitoneal ketamine/xylazine cocktail and perfused transcardially using cold cutting buffer (119 mM NaCl, 26.2 mM NaHCO3, 2.5 mM KCl, 1 mM NaH2PO4,3.5 mM MgCl2, 10 mM glucose, and 0 mM CaCl2). The brain was then rapidly dissected, mounted on a vibratome stage (Leica VT1200 S) using super glue, and cut into 300 µm thick slices containing the dorsal striatum. Slices were then collected and incubated at 37°C for 30 minutes in oxygen saturated ACSF (119 mM NaCl, 26.2 mM NaHCO3, 2.5 mM KCl, 1 mM NaH2PO4, 1.3 mM MgCl2, 10 mM glucose, and 2 mM CaCl2) followed by 30-minute incubation at room temperature. All slices are maintained at room temperature until imaging and used within 6 hours of preparation.

Slices are labeled through passive incubation in 5 ml of ACSF containing nIRCat nanosensor at a concentration of 2 mg/L for 15 minutes. After incubation, the slices is transferred through 3 wells of a 24-well plate containing ACSF to rinse off non-localized nIRCat sensor and then left to rest at room temperature ACSF for 15 minutes before transfer to the 32°C recording chamber. Once placed in the recording chamber, slices equilibrate for 15 minutes during which a tungsten bipolar stimulation electrode is positioned at a field of view in the dorsal-lateral striatum using a 4x objective (Olympus XLFluor 4/ 340). Under a 60x objective the electrode is moved 200 µm away from the selected field of view and brought into contact with the surface of the brain slice. In all experiments, 600 total images are acquired into an image-stack at a rate of 9 frames per second. A single stimulation of 0.1 mA or 0.3 mA is applied after 200 frames of baseline are collected. Videos of stimulation at each strength are collected in triplicate and stimulation strengths are alternated. All slices are given 5 minutes between each stimulation with the excitation laser path shuttered. Prior to stimulation, the laser is un-shuttered for 1 minutes.

6.5.5 nIRCat Imaging Calcium Wash and Sulpiride wash

To image nIRCat-labeled acute brains slices at multiple extracellular calcium concentrations, buffers were prepared at three calcium concentrations: 1 mM Low Calcium Buffer (119 mM NaCl, 26.2 mM NaHCO3, 2.5 mM KCl, 1 mM NaH2PO4, 1.3 mM MgCl2, 10 mM glucose, and 1 mM CaCl2), 2 mM Normal Calcium Buffer (119 mM NaCl, 26.2 mM NaHCO3, 2.5 mM KCl, 1 mM NaH2PO4, 1.3 mM MgCl2, 10 mM glucose, and 2 mM CaCl2), 4 mM High Calcium Buffer (119 mM NaCl, 26.2 mM NaHCO3, 2.5 mM KCl, 1 mM NaH2PO4, 1.3 mM MgCl2, 10 mM glucose, and 4 mM CaCl2). Following stimulation in 2 mM Normal

Calcium Buffer, 4 mM High Calcium buffer was flowed into the imaging chamber for 15 minutes (Full bath turnover in 3 minutes). After buffer transfer, the slice was stimulated at 0.1 mA and 0.3 mA in triplicate as described for 2 mM Normal Calcium Buffer. Buffer was then exchanged again to 1 mM Low Calcium Buffer via 15-minute wash and the slice was stimulated at 0.1 mA and 0.3 mA in triplicate.

To nIRCat image acute brain slices in the presence of the D2-antagonist Sulpiride, S-Sulpiride was dissolved in sterile DMSO and frozen in 100 µl aliquots at -20°C. Prior to use, single aliquots are thawed and added to 100 mL of ACSF to produce a 10 µM Sulpiride solution. Acute brain slices were stimulated at 0.1 mA and 0.3 mA in triplicate in sulpiride-free ACSF. Sulpiride solution was flowed into the imagine chamber for 15 minutes before stimulating the slice at 0.1 mA and 0.3 mA in triplicate.

6.5.6 Image Stack Processing and Data Analysis of nIRCat Data

Raw Image stack files are processed using a custom-built, publicly available MATLAB program (https://github.com/jtdbod/Nanosensor-Imaging-App). Image processing procedures are described in depth in Yang, del Bonis O'Donnel et al and briefly summarized here. Regions of dopamine release are identified by large changes in nIRCat $\Delta F/F$ response. To minimize bias and improve stack processing time, regions of high $\Delta F/F$ response (dopamine hotspots) were identified by defining a grid of 2 µm squares across the field of view. For each grid square $\Delta F/F$ was calculated using the formula (F- F0) /F0, where F0 is defined by the average fluorescence of the grid square over the first 30 frames of the image stack and F is the fluorescence intensity of the gird square as it changes over the 600 collected frames. Grid squares are identified as regions of interest if they exhibit behavior that is 3 standard deviations above the baseline F0 activity around time of stimulation (200 frames).

Dopamine hotspots were identified for each stimulation replicate image stack taken at a given field-of-view on a brain slice. The peak $\Delta F/F$ of each dopamine hotspot in the image stack were averaged to give the average image stack peak $\Delta F/F$. The average image stack peak $\Delta F/F$ from the three stimulation replicates were then average to give the slice average peak $\Delta F/F$. Similarly, the number of dopamine hotspots identified from each stimulation replicate image stack were averaged to give the slice average hotspot number. Mean dopamine release and reuptake traces are produced by averaging the average traces from each slice (3 stimulations per slice, 1 slice per animal). Percent change in hotspots was calculated as (number hotspots wash - number hotspots 2 mM Ca^{+2})/ (number hotspots 2 mM Ca^{+2}), whereas change in hotspots number was calculated as (number hotspots wash - number hotspots 2 mM Ca^{+2}).

To track hotspot fidelity, each initially defined grid square was assigned a unique position number, allowing the position of each identified dopamine hotspot within an image stack to be recorded. For a set of triplicate image stacks, an array of all unique hotspots active across the stimulation replicates was generated. Then python code was used to analyze whether each unique hotspot was active in each stimulation replicate. The number of stimulations

a unique hotspot was active in was summed across the three replicates and assigned as the dopamine release fidelity (e.g. hotspot '12' is active in 2 out of 3 stimulations and is assigned release fidelity 2). The same procedure was used to identify the dopamine release fidelity of hotspots active after drug wash. Hotspots were then separated into three groups: hotspots that are active both before and after drug wash (shared hotspots), hotspots that become active after drug wash (added hotspots), and hotspots that are only active before drug wash. For shared hotspots modulation in hotspot release strength was calculated as the difference in peak $\Delta F/F$ of the unique hotspot before and after drug wash, (mean $\Delta F/F$)post - (mean $\Delta F/F$)pre , where (mean $\Delta F/F$)pre is the average peak $\Delta F/F$ of each unique dopamine hotspot across the three stimulations before drug wash and (mean $\Delta F/F$)post is the average peak $\Delta F/F$ of each unique dopamine hotspot across the three stimulations after drug wash. For hotspots active only after drug wash, there is no corresponding "pre drug wash" $\Delta F/F$. Therefore, the difference in peak $\Delta F/F$ was calculated through (mean $\Delta F/F$)post - (mean $\Delta F/F$)pre, shared, where (mean $\Delta F/F$)post represents the average peak $\Delta F/F$ of the unique dopamine hotspot active after sulpiride wash across three stimulations and (mean $\Delta F/F$)pre, shared is the average of all the shared hotspots' mean $\Delta F/F$ from the slice before drug wash.

6.5.7 Exerimental Design and Statistical Analysis

All nIRCat Imaging data were processed using a custom-built, publicly available MATLAB program (https://github.com/jtdbod/Nanosensor-Imaging-App). Statistical analyses were conducted using the open-source statistical python package pingouin. All bar graphs show the mean with error bars denoting the 95% confidence interval. All single data points correspond to a single slice taken from an animal. Data comparing two variables was analyzed using a mixed-ANOVA with wash condition as the within-subject factor (e.g.sulpiride, blank, calcium concentration) and disease state as the between-subject factor (eg. HD, WT). Paired t-tests were used a post-hoc tests if mixed-ANOVA analyses indicated significant differences. Data comparing two values of one variable were analyzed using tukey's t-test. Group sizes were determined based on previous literature (Adil et al., 2018). Changes in histogram skew were computed through pooling of all hotspots identified across all mice within the disease and wash condition and evaluated using a permutation test using the test statistic μ = skew(post wash) – skew(pre-wash).

Chapter 7

Future Work [vi]

[vi] This section is produced in part with permission from the following works: Yang, S. J.*, Del Bonis-O'Donnell, J.T.*, et al. "Near-infrared catecholamine nanosensors for high spatiotemporal dopamine imaging." *Nature Protocols* (2021), 16, 3026–3048., Beyene, A.G.*, Yang, S.J.*, Landry, M.P., "Tools and Trends for Probing Brain Neurochemistry." *Journal of Vacuum Science and Technology A* (2019), 37(4): 040802.

7.1 Future Work

Previous work from Beyene et al. established nIRCat imaging as a powerful and viable tool for visualizing dopamine release in *ex vivo* brain slices. In the work presented in this dissertation, I demonstrate the versatility of nIRCat imaging in answering biological questions whose answer were previously limited by available sensing technologies. In the Section 7.1.1 I discuss how the nIRCat imaging platform may be further developed for a the new, developing frontier of neuroscience questions. In the Section 7.1.2 and Section 7.1.3 I discuss how the methods and protocols presently availble for nIRCat imaging can be adapted to explore new questions in the field of dopamine signaling and Huntington's Disease.

7.1.1 Future Directions for the nIRCat Imaging Platform

The development and application of the nIRCat imaging for biological studies in *ex vivo* living brain slices represents a landmark achievement in the field of single-walled carbon nanotube (SWNT) sensor development. Nevertheless, there remain large frontiers for future SWNT sensor development and exploration. In this section I discuss the principle limitations of present nIRCat imaging technology and potential avenues for future discovery.

The three main limitations of nIRCat imaging at present are the unique microscopy tools required for its implementation, its verification only in acute brain slice preparations, and its inability to distinguish between the catecholamines dopamine and norepinephrine. The unique nIR spectral range of nIRCat nanosensors confers multiple benefits, including imaging within the tissue transparency window and a strong theoretical ability to multiplex with other neurobiolgoical optical tools due to minimal spectral overlap. However, imaging in the nIR requires specialized short-wavelength IR detectors that are less commonly available to neurobiology laboratories than visible microscopy. This presents a major obstacle in the adoption of nIRCat imaging and other nIR imaging technologies in standard biology labs interested in utilizing nIRCat imaging. In contrast, genetically encoded dopamine sensors have found ready adoption in the biological community due to their utilization of standard techniques and visible-wavelength optics commonly found in biology labs. However, by similar principle, the green fluorescent protein (GFP) used in standard dLight and GRAB-DA constructs that occupies the same spectral wavelengths as other biological tools results in inability to multiplex dopamine imaging with other GFP sensors. As a result, this has required the development of red-shifted variants of dLight and GRAB-DA to allow for sensor multiplexing[152].

Second, to date, SWNT-based nIR nanosensors have been used only to image dopamine, or other monoamines, in *in vitro* cell cultures, primary nerons and *ex vivo* brain slices. There is presently no established method for in vivo imaging of dopamine with nIRCat, and more work must be done to use nIRCat within live animals. Living mice are able to sustain direct stereotaxic injection of nIRCat sensor into the striatum. However, examination of nIRCat

distribution in prepared brain slices shows that the majority of nanosensor remains localized around the site of injection rather than distributing evenly throughout the striatum. This high concentration of nanosensor within brain tissue may serve as a strong driver of immune and inflammatory response in the brain, particularly if left on the scale of days[11]. Furthermore, nIRCat nanosensor does not appear to remain responsive to dopamine 24 hrs following injection suggesting that extended time in the protein-rich extracellular milieu of the living brain may drive biofouling of nIRCat nanosensors or displacement of the $(GT)_6$ from the SWNT surface. Robust performance of SWNT sensors *in vivo* will require nanosensors to maintain a robust response to dopamine and resistance to biofouling ideally over the course of days to weeks. Imaging at these timescales would allow researchers to fully take advantage of SWNT-sensors' resistance to photobleaching and measure biological phenomena that occur over extended timescales. Addressing these challenges will require new methods to engineer improved and stable binding dynamics at the SWNT surfaces, either through covalent modifications that allow stable binding domains at the SWNT surface without disruption of optical properties or through passive adsorption of bio-mimicking polymers or proteins that "cloak" SWNT sensors from immune response in the brain. In both cases, a deep understanding of tradeoffs between sensor response, immune responsiveness, and stability will be required. As such, development of robust SWNT sensors for *in vivo* work will be driven by studies that develop a deeper, fundamental understanding of how SWNT sensors affect and are affected by biological environments.

Lastly, nIRCat is presently a catecholamine sensor that is unable to distinguish between the molecules dopamine and norepinephrine. Therefore, nIRCat can be used as a dopamine probe in the context of brain regions or organisms absent of norepinephrinergic innervation, or alongside pharmacological agents for suppressing norepinephrine release. Present protocols focus on using nIRCat as a dopamine probe in the dorsal striatum, a brain region where dopamine is a key neuromodulator with minimal competing catecholamine release. developing sensors that are able to distinguish between catecholamine and norepinepherine will require either deeper understanding of SWNT sensor binding dynamics at the molecular level, enabling rational design, or development of a "directed evolution" method for the identification of SWNT-sensors with desirable properties. Initial steps towards developing a "direct evolution-like" selection process for SWNT-nanosensors have been made by the SELEC system, which supported the identification of a SWNT-sensor for seratonin[153]. However, the principle weakness of SELEC lies in its inability to directly screen for robust sensor performance. Currently, candidates within a SELEC pool are screened for their ability to bind to a target molecule over competing molecules. Strong binders are then separately evaluated for optical response. As such, SELEC is a system that directly screens for selectivity and then manually selects for optical response afterwards. This compromise in selection process allows for the identification of strong selective binders, but does not readily identify sensors with the strong optical turn on response needed for robust biological imaging[153]. A more powerful mechanism for SWNT-sensor engineering would be a system that simultaneously screens for selectivity and optical response over successive rounds, allowing for the identification of sensor candidates from the full library pool rather than a small, pre-selected pool. This may be accomplished by coupling a SELEC sensor specificity selection with a robot-assisted optical response selection that can be evaluated under a microscope similar

to those applied to the development of voltage sensors[154].

Establishing an efficient and effective method of screening SWNT sensors would support the new development of second-generation dopamine and seratonin sensors as well as the discovery of SWNT sensors for new targets. Future methods may seek to multiplex SWNT-sensors for different targets in single experiments to understand release-dynamics of different signaling molecules in relation to one another. Achievement of SWNT sensor multiplexing requires the generation of different colors of SWNT for assignment to different sensors. SWNT chiralities already exhibit fluorescence at different wavelengths, and preparation of sensors at specific chiralities would require minimal adjustment to existing SWNT sensor synthesis protocols as present methods produce SWNT sensor from a mix of SWNT chiralities. Present bottlenecks for the creation of an expanded SWNT-sensor color palette instead lies in the ability to separate SWNT sensors based on individual chiralities. As such, expanded methods for the generation or purification of specific SWNT chiralities will be required in order to establish SWNT sensor multiplexing.

7.1.2 Future Directions for nIRCat in Dopamine Research

Imaging dopamine release with nIRCat nanosensors in *ex vivo* has provided new insights into how dopamine release is mobilized and regulated across the striatum. To date, nIRCat imaging has been used to image dopamine release in the dorsal medial striataum of C57BL/6, dorsal medial striatum of *M. spicilegus*, and in this work the dorsal lateral striatum of R6/2 Huntington's Disease model mice. We find here that dopamine hotspot number, mean peak $\Delta F/F$, and dopamine release fidelity are all metrics that shape dopamine release over the course of neurodegeneration. Studies employing nIRCat imaging have to date all elected to characterize dopamine release in a single region of the striatum. Given recent findings that the striatum is composed of different regions of molecularly defined dopamine subtypes, future applications of nIRCat imaging may focus on mapping different dopamine release patterns across the striatum may provide insight into how these molecular subtypes shape different signaling patterns that shape behavior[155]. This could be accomplished through imaging multiple fields of view across the striatum or conducting nIRCat imaging at lower magnification to visualize the entire striatum in a imaging field of view. Imaging at higher magnification affords greater ability to resolve indivudal hotspot dynamics while imaging at lower magnification allows for visualization of how regions may signal between one another. Connection of nIRCat dopamine release profiles with genetic sub populations of dopamine neurons may be achieved by preserving striatal brain slices for post-imaging immunostaining or imaging within mouselines that genetically visualize dopamine neuron sub-populations via fluorescent protein expression. Developing a post-imaging immunostaining method would allow connection between genetic neuron identity and dopamine release in multiple mouse models. However, simultaneous imaging of visible and nIR signals within mouselines that genetically visualize dopamine neuron subpopulations would allow real-time observation of how dopamine release is organized spatially within the striatum.

Future applications of nIRCat imaging can also be found in utilizing nIRCat's non-genetically encoded nature to explore early age timepoints with no sensor expression time. Studies into striatal development have shown that dopamine release properties in mice may be shaped by cholinergic signaling as early as 10 days of age and dopamine release in turn can shape medium spiny neuron excitability[156;157]. Typical expression times for genetically encoded sensors typically range on the scale of 1-2 weeks. Imaging mice during this critical period would require injection of sensor construct into young animals, and over-expression of sensor constructs could affect normal striatal development. In these contexts, use of a non-genetically encoded sensors that can be introduced after brain slices have been generated is particularly advantageous. In a similar vein, non-genetically sensors are well suited for studying neurodegenerative disease, allowing animals to undergo disease processes without interference from sensor expression.

Lastly, expanded application of nIRCat into non-murine animal models should be explored to facilitate the use of non-genetically tractable animal models for dopamine research. Initial efforts my be focused on implementation of nIRCat imaging in genetically tractable, but non-murine animal models such as rats, flies, and zebrafish. Imaging with nIRCat may be especially attractive in flies (Drosophila melanogaster) where there is no cross-signaling from norepinepherine. Further development may choose to focus on mid-size animals such as ferrets and naked mole rats, which have found applications in specific disorders or biological reseasrch, and ultimately culminate in non-human primates. Expansion of dopamine research into non-murine applications will allow for the development of a deeper understanding of the broad fundamentals of dopamine signaling outside of specific instances within rodent models.

7.1.3 Future Directions for nIRCat in Huntington's Disease Research

I demonstrate in this dissertation that nIRCat imaging can provide new insights into how disruptions in dopamine signaling manifest during Huntington's Disease (HD). Use of nIRCat imaging to gain new insights into HD is a rich and promising area for future development of nIRCat applications and method development. Many of the methods discussed in Section7.1.2 can be adapted for Huntington's Disease research. Methods visualizing molecular subpopulations of dopamine neurons or protein expression within striatal neurons through immunostaining may be utilized to investigate how mutant huntingtin driven molecular disruptions are associated with different aspects of dopamine release. For example, visualizing whether disruptions in Kv1.2 channel organization in the presynapse underlie changes in dopamine release fidelity. Similarly, methods for nIRCat imaging in young mice can be used for study of early critical periods in HD development and methods for nIRCat imaging in non-murine organisms can be used to explore dopamine disruptions in mini pig or non-human primate models of Huntington's Disease.

One of the most compelling applications for nIRCat imaging is the opportunity to study how dopamine signaling changes in patients and model organisms in response to therapy. Hunt-

ington's Disease is believed to manifest through the collective result of cell autonomous events and disruptions in synaptic signaling that compound into greater dysfunction[4]. Global suppression of mutant huntingtin—even after symptom onset— has shown to facilitate molecular and behavior recovery in HD model mice[158]. Ongoing efforts to find effective treatments or cures for Huntington's Disease have primarily focused on directly addressing the production of disease-causing mutant huntingtin protein at levels across translation, transcription, and the gene itself in striatal and cortical regions[71;72;74;76]. Coordinated targeting of mutant huntingtin in these compartments together has been shown to have a synergistic effect, strengthening the hypothesis that striatal cortico-striatal synapses play a critical role in HD pathogenesis[159]. Our findings suggest that the dopaminergic neurons that natively modulate this cortico-striatal signaling are a promising new therapeutic area that experience dysfunction during HD and may confer synergistic effects during treatment. These therapies may also find differing efficacy depending on the stage of disease development they are delivered.

Imaging changes in dopamine release over the course of therapeutic administration would provide pivotal insights into mechanisms of therapeutic action, the processes by which the brain functionally adapts to treatment on a circuits level, and opportunities to individually adjust treatment strategies based on patient responsiveness. Imaging *ex vivo* brain slices from animal undergoing gene therapies or cell replacement therapies may provide insights into how the brain adapts to the introduction of therapeutic constructs to repair signaling to healthy levels. This knowledge is critical for the creation of improved therapeutics as well as the advancement of basic science understandings of how the brain responds to large interventions that shut down gene function or introduce large numbers of new neurons. In a similar vein, current methods of evaluating therapeutic efficacy rely on end-point analysis, where subjects are administered therapies and then evaluated for therapeutic efficacy at defined endpoints. This study structure hides the day to day dynamics of therapeutic action. Visualization of these hidden dynamics would provide the unique opportunity to understand the procession of therapeutic mechanism at a more temporally defined level and actively adjust therapeutic parameters to provide optimal patient response. However, long-term sensing experiments within the brain are a technologically challenging area of active research. An *in vivo* application of nIRCat to visualize these dynamics may be particularly well suited to these technical challenges given that nIRCat is resistant to photo bleaching and can utilize near-infrared wavelengths for non-invasive imaging over long studies. Realization of this application will require the development of a nIRCat SWNT-sensor variant that can resist biofouling and escape immune detection *in vivo* over long experiment courses as discussed in Section7.1.1. Nevertheless, the promising adaptation of nIRCat nanosensors from an *in vitro* context to biological *ex vivo* application as demonstrated in this dissertation work suggests that the SWNT sensor field is rapidly expanding into a frontier where robust *in vivo* SWNT sensors play a key role in making complex studies of neurological biology and disease over multiple time and size scales a reality.

Bibliography

[1] P. Calabresi, B. Picconi, A. Tozzi, M. Di Filippo, *Trends in Neurosciences* **2014**, *30*, 5 211.

[2] S. Bariselli, W. Fobbs, M. Creed, A. Kravitz, *Brain Research* **2019**, *1713* 70.

[3] F. Saudou, S. Humbert, *Neuron* **2016**, *89*, 5 910.

[4] C. Cepeda, M. S. Levine, *The Neuroscientist* **2020**, 107385842097266.

[5] A. Muller, V. Joseph, P. A. Slesinger, D. Kleinfeld, *Nature Methods* **2014**, *11*, 12 1245.

[6] A. G. Beyene, K. Delevich, S. J. Yang, M. P. Landry, *Biochemistry* **2018**, *57*, 45 6379.

[7] D. Sames, M. Dunn, R. J. Karpowicz, D. Sulzer, *ACS Chemical Neuroscience* **2013**, *4*, 5 648.

[8] S. Golovynskyi, I. Golovynska, L. I. Stepanova, O. I. Datsenko, L. Liu, J. Qu, T. Y. Ohulchanskyy, *Journal of Biophotonics* **2018**, *11*, 12 e201800141.

[9] A. G. Beyene, K. Delevich, J. T. Del Bonis-O'Donnell, D. J. Piekarski, W. C. Lin, A. W. Thomas, S. J. Yang, P. Kosillo, D. Yang, G. S. Prounis, L. Wilbrecht, M. P. Landry, *Science Advances* **2019**, *5*, 7 eaaw3108.

[10] S. J. Yang, J. T. Del Bonis-O'Donnell, A. G. Beyene, M. P. Landry, *Nature Protocols* **2021**, *16*, 6 3026.

[11] D. Yang, S. J. Yang, J. T. Del Bonis-O'Donnell, R. L. Pinals, M. P. Landry, *ACS Nano* **2020**, *14*, 10 13794.

[12] M. O. Klein, D. S. Battagello, A. R. Cardoso, D. N. Hauser, J. C. Bittencourt, R. G. Correa, *Cellular and Molecular Neurobiology* **2018**, *39*, 1.

[13] D. Sulzer, S. J. Cragg, M. E. Rice, *Basal Ganglia* **2016**, *6*, 3 123.

[14] M. Scanziani, M. Häusser, *Nature* **2009**, *461*, 7266 930.

[15] E. D. P. De Robertis, H. S. Bennett, *The Journal of Biophysical and Biochemical Cytology* **1954**, *1*, 1 47.

[16] L. T. Coddington, J. T. Dudman, *Neuron* **2019**, *104*, 1 63.

[17] S. Grillner, B. Robertson, M. Stephenson-Jones, *The Journal of Physiology* **2013**, *591*, 22 5425.

[18] G. Graveland, M. Difiglia, *Brain Research* **1985**, *327*, 1 307.

[19] M. Assous, J. M. Tepper, *European Journal of Neuroscience* **2019**, *49*, 5 593.

[20] C. Liu, X. Cai, A. Ritzau-Jost, P. F. Kramer, Y. Li, Z. M. Khaliq, S. Hallermann, P. S. Kaeser, *Science* **2022**, *375*, 6587 1378.

[21] A. C. Burton, K. Nakamura, M. R. Roesch, *Neurobiology of Learning and Memory* **2015**, *117* 51.

[22] C. M. Gremel, R. M. Costa, *Nature Communications* **2013**, *4*, 1 2264.

[23] A. V. Kravitz, B. S. Freeze, P. R. L. Parker, K. Kay, M. T. Thwin, K. Deisseroth, A. C. Kreitzer, *Nature* **2010**, *466*, 7306 622.

[24] G. Cui, S. B. Jun, X. Jin, M. D. Pham, S. S. Vogel, D. M. Lovinger, R. M. Costa, *Nature* **2013**, *494*, 7436 238.

[25] F. Tecuapetla, X. Jin, S. Q. Lima, R. M. Costa, *Cell* **2016**, *166*, 3 703.

[26] H. Sontheimer, *Chapter 7: Huntington Disease*, Elsevier, London Wall, London, **2015**.

[27] S. Finkbeiner, *Cold Spring Harbor Perspectives in Biology* **2011**, *3*, 6 a007476.

[28] R. Paoli, A. Botturi, A. Ciammola, V. Silani, C. Prunas, C. Lucchiari, E. Zugno, E. Caletti, *Brain Sciences* **2017**, *7*, 12 67.

[29] J. F. Gusella, N. S. Wexler, P. M. Conneally, S. L. Naylor, M. A. Anderson, R. E. Tanzi, P. C. Watkins, K. Ottina, M. R. Wallace, A. Y. Sakaguchi, A. B. Young, I. Shoulson, E. Bonilla, J. B. Martin, *Nature* **1983**, *306*, 5940 234.

[30] A. Reiner, I. Dragatsis, P. Dietrich, *Genetics and Neuropathology of Huntington's Disease*, volume 98, Elsevier, **2011**.

[31] I. S. Seong, J. M. Woda, J.-J. Song, A. Lloret, P. D. Abeyrathne, C. J. Woo, G. Gregory, J.-M. Lee, V. C. Wheeler, T. Walz, R. E. Kingston, J. F. Gusella, R. A. Conlon, M. E. MacDonald, *Human Molecular Genetics* **2010**, *19*, 4 573.

[32] M. El-Daher, E. Hangen, J. Bruyère, G. Poizat, I. Al-Ramahi, R. Pardo, N. Bourg, S. Souquere, C. Mayet, G. Pierron, S. Lévêque-Fort, J. Botas, S. Humbert, F. Saudou, *The EMBO Journal* **2015**, *34*, 17 2255.

[33] H. Runne, E. Regulier, A. Kuhn, D. Zala, O. Gokce, V. Perrin, B. Sick, P. Aebischer, N. Deglon, R. Luthi-Carter, *Journal of Neuroscience* **2008**, *28*, 39 9723.

[34] J. Fan, C. M. Cowan, L. Y. J. Zhang, M. R. Hayden, L. A. Raymond, *Journal of Neuroscience* **2009**, *29*, 35 10928.

[35] C. Zuccato, M. Marullo, B. Vitali, A. Tarditi, C. Mariotti, M. Valenza, N. Lahiri, E. J. Wild, J. Sassone, A. Ciammola, A. C. Bachoud-Lèvi, S. J. Tabrizi, S. Di Donato, E. Cattaneo, *PLoS ONE* **2001**, *6*, 8 e22966.

[36] L. W. Ho, J. Carmichael, J. Swartz, A. Wyttenbach, J. Rankin, D. C. Rubinsztein, *Psychological Medicine* **2001**, *31*, 1 3.

[37] E. Cattaneo, D. Rigamonti, D. Goffredo, C. Zuccato, F. Squitieri, S. Sipione, *Trends in Neurosciences* **2001**, *24*, 3 182.

[38] R. K. Graham, E. J. Slow, Y. Deng, N. Bissada, G. Lu, J. Pearson, J. Shehadeh, B. R. Leavitt, L. A. Raymond, M. R. Hayden, *Neurobiology of Disease* **2006**, *21*, 2 444.

[39] S.-H. Li, G. Schilling, W. Young, X.-. Li, R. Margolis, O. Stine, M. Wagster, M. Abbott, M. Franz, N. Ranen, S. Folstein, J. Hedreen, C. Ross, *Neuron* **1993**, *11*, 5 985.

[40] M. DiFiglia, E. Sapp, K. Chase, C. Schwarz, A. Meloni, C. Young, E. Martin, J.-P. Vonsattel, R. Carraway, S. A. Reeves, F. M. Boyce, N. Aronin, *Neuron* **1995**, *14*, 5 1075.

[41] G. B. Landwehrmeyer, S. M. McNeil, L. S. Dure, P. Ge, H. Aizawa, Q. Huang, C. M. Ambrose, M. P. Duyao, E. D. Bird, E. Bonilla, M. de Young, A. J. Avila-Gonzales, N. S. Wexler, M. DiFiglia, J. F. Gusella, M. E. MacDonald, J. B. Penney, A. B. Young, J.-P. Vonsattel, *Annals of Neurology* **1995**, *37*, 2 218.

[42] M. Arrasate, S. Mitra, E. S. Schweitzer, M. R. Segal, S. Finkbeiner, *Nature* **2004**, *431*, 7010 805.

[43] T. Takahashi, S. Kikuchi, S. Katada, Y. Nagai, M. Nishizawa, O. Onodera, *Human Molecular Genetics* **2008**, *17*, 3 345.

[44] G. E. Hardingham, H. Bading, *Nature Reviews Neuroscience* **2010**, *11*, 10 682.

[45] V. M. André, C. Cepeda, M. S. Levine, *CNS Neuroscience & Therapeutics* **2010**, *16*, 3 163.

[46] C. Rangel-Barajas, G. V. Rebec, *Journal of Huntington's Disease* **2016**, *5*, 4 303.

[47] T.-T. Huang, R. Smith, K. Bacos, D.-Y. Song, R. M. Faull, H. J. Waldvogel, J.-Y. Li, *Acta Neuropathologica Communications* **2020**, *8*, 1 77.

[48] S. Blumenstock, I. Dudanova, *Science* **2022**, *377*, 6613 1383.

[49] W. F. Kaemmerer, R. Grondin, *Degenerative Neurological and Neuromuscular Disease* **2019**, *Volume 9* 3.

[50] C. Cepeda, R. S. Hurst, C. R. Calvert, E. Hernández-Echeagaray, O. K. Nguyen, E. Jocoy, L. J. Christian, M. A. Ariano, M. S. Levine, *The Journal of Neuroscience* **2003**, *23*, 3 961.

[51] P. R. Joshi, N.-P. Wu, V. M. Andre, D. M. Cummings, C. Cepeda, J. A. Joyce, J. B. Carroll, B. R. Leavitt, M. R. Hayden, M. S. Levine, N. S. Bamford, *Journal of Neuroscience* **2009**, *29*, 8 2414.

[52] E. T. Koch, L. A. Raymond, *Journal of Neuroscience Research* **2019**, jnr.24495.

[53] M. P. Parsons, M. P. Vanni, C. L. Woodard, R. Kang, T. H. Murphy, L. A. Raymond, *Nature Communications* **2016**, *7*, 1 11251.

[54] L. Raymond, V. André, C. Cepeda, C. Gladding, A. Milnerwood, M. Levine, *Neuroscience* **2011**, *198* 252.

[55] J. Plotkin, M. Day, J. Peterson, Z. Xie, G. Kress, I. Rafalovich, J. Kondapalli, T. Gertler, M. Flajolet, P. Greengard, M. Stavarache, M. Kaplitt, J. Rosinski, C. Chan, D. Surmeier, *Neuron* **2014**, *83*, 1 178.

[56] J. Creus-Muncunill, M. E. Ehrlich, *Neurotherapeutics* **2019**, *16*, 4 957.

[57] I. Sebastianutto, M. A. Cenci, T. Fieblinger, *Neurobiology of Disease* **2017**, *105* 117.

[58] B. Y. Braz, D. Wennagel, L. Ratié, D. A. R. de Souza, J. C. Deloulme, E. L. Barbier, A. Buisson, F. Lanté, S. Humbert, *Science* **2022**, *377*, 6613 eabq5011.

[59] J. Segura-Aguilar, I. Paris, P. Muñoz, E. Ferrari, L. Zecca, F. A. Zucca, *Journal of Neurochemistry* **2014**, *129*, 6 898.

[60] A. N. Ortiz, B. J. Kurth, G. L. Osterhaus, M. A. Johnson, *Journal of Neurochemistry* **2010**, *112*, 3 755.

[61] A. N. Ortiz, B. J. Kurth, G. L. Osterhaus, M. A. Johnson, *Neuroscience Letters* **2011**, *492*, 1 11.

[62] J. W. Callahan, E. D. Abercrombie, *Frontiers in Systems Neuroscience* **2011**, *5*.

[63] C. Cepeda, K. P. Murphy, M. Parent, M. S. Levine, *The role of dopamine in huntington's disease*, volume 211, Elsevier, **2014**.

[64] V. M. André, Y. E. Fisher, M. S. Levine, *Frontiers in Systems Neuroscience* **2011**, *5*.

[65] C. Liu, L. Kershberg, J. Wang, S. Schneeberger, P. S. Kaeser, *Cell* **2018**, *172*, 4 706.

[66] C. Liu, P. S. Kaeser, *Current Opinion in Neurobiology* **2019**, *57* 46.

[67] A. Banerjee, J. Lee, P. Nemcova, C. Liu, P. S. Kaeser, *eLife* **2020**, *9* e58359.

[68] J. K. Dreyer, K. F. Herrik, R. W. Berg, J. D. Hounsgaard, *Journal of Neuroscience* **2010**, *30*, 42 14273.

[69] J. K. Dreyer, J. Hounsgaard, *Journal of Neurophysiology* **2013**, *109*, 1 171.

[70] S. Frank, *Neurotherapeutics* **2014**, *11*, 1 153.

[71] Y. Machida, T. Okada, M. Kurosawa, F. Oyama, K. Ozawa, N. Nukina, *Biochemical and Biophysical Research Communications* **2006**, *343*, 1 190.

[72] J. L. McBride, M. R. Pitzer, R. L. Boudreau, B. Dufour, T. Hobbs, S. R. Ojeda, B. L. Davidson, *Molecular Therapy* **2011**, *19*, 12 2152.

[73] A. D. Carri, M. Onorati, M. J. Lelos, V. Castiglioni, A. Faedo, R. Menon, S. Camnasio, R. Vuono, P. Spaiardi, F. Talpo, M. Toselli, G. Martino, R. A. Barker, S. B. Dunnett, G. Biella, E. Cattaneo, *Development* **2013**, *140*, 2 301.

[74] K. D. Fink, P. Deng, J. Gutierrez, J. S. Anderson, A. Torrest, A. Komarla, S. Kalomoiris, W. Cary, J. D. Anderson, W. Gruenloh, A. Duffy, T. Tempkin, G. Annett, V. Wheelock, D. J. Segal, J. A. Nolta, *Cell Transplantation* **2016**, *25*, 4 677.

[75] M. M. Adil, T. Gaj, A. T. Rao, R. U. Kulkarni, C. M. Fuentes, G. N. Ramadoss, F. K. Ekman, E. W. Miller, D. V. Schaffer, *Stem Cell Reports* **2018**, *10*, 5 1481.

[76] M. M. Evers, J. Miniarikova, S. Juhas, A. Vallès, B. Bohuslavova, J. Juhasova, H. K. Skalnikova, P. Vodicka, I. Valekova, C. Brouwers, B. Blits, J. Lubelski, H. Kovarova, Z. Ellederova, S. J. van Deventer, H. Petry, J. Motlik, P. Konstantinova, *Molecular Therapy* **2018**, *26*, 9 2163.

[77] F. K. Ekman, D. S. Ojala, M. M. Adil, P. A. Lopez, D. V. Schaffer, T. Gaj, *Molecular Therapy - Nucleic Acids* **2019**, *17* 829.

[78] D. Kwon, *Nature* **2021**, *593*, 7858 180.

[79] C. Sheridan, *Nature Biotechnology* **2021**, *39*, 6 650.

[80] Y. Kubota, J. Sohn, Y. Kawaguchi, *Frontiers in Neural Circuits* **2018**, *12* 98.

[81] C. S. Xu, K. J. Hayworth, Z. Lu, P. Grob, A. M. Hassan, J. G. García-Cerdán, K. K. Niyogi, E. Nogales, R. J. Weinberg, H. F. Hess, *eLife* **2017**, *6* e25916.

[82] K. J. Hayworth, D. Peale, M. Januszewski, G. W. Knott, Z. Lu, C. S. Xu, H. F. Hess, *Nature Methods* **2020**, *17*, 1 68.

[83] A. L. Hodgkin, A. F. Huxley, *Nature* **1939**, *144*, 3651 710.

[84] J. K. Haumesser, J. Kühn, C. Güttler, D.-H. Nguyen, M. H. Beck, A. A. Kühn, C. van Riesen, *Journal of Visualized Experiments* **2017**, *e55940*, 124 55940.

[85] D. L. Hunt, C. Lai, R. D. Smith, A. K. Lee, T. D. Harris, M. Barbic, *Nature Biomedical Engineering* **2019**, *3*, 9 741.

[86] D. Khodagholy, T. Doublet, P. Quilichini, M. Gurfinkel, P. Leleux, A. Ghestem, E. Ismailova, T. Hervé, S. Sanaur, C. Bernard, G. G. Malliaras, *Nature Communications* **2013**, *4*, 1 1575.

[87] T. Branco, K. Staras, *Nature Reviews Neuroscience* **2009**, *10*, 5 373.

[88] S. Chemla, F. Chavane, *Journal of Physiology-Paris* **2010**, *104*, 1 40.

[89] H. V. Davila, B. M. Salzberg, L. B. Cohen, A. S. Waggoner, *Nature New Biology* **1973**, *241*, 109 159.

[90] B. E. Kang, B. J. Baker, *Scientific Reports* **2016**, *6*, 1 23865.

[91] L. Jin, Z. Han, J. Platisa, J. Wooltorton, L. Cohen, V. Pieribone, *Neuron* **2012**, *75*, 5 779.

[92] R. Y. Tsien, *Biochemistry* **1980**, *19*, 11 2396.

[93] T.-W. Chen, T. J. Wardill, Y. Sun, S. R. Pulver, S. L. Renninger, A. Baohan, E. R. Schreiter, R. A. Kerr, M. B. Orger, V. Jayaraman, L. L. Looger, K. Svoboda, D. S. Kim, *Nature* **2013**, *499*, 7458 295.

[94] M. Tada, A. Takeuchi, M. Hashizume, K. Kitamura, M. Kano, *European Journal of Neuroscience* **2014**, *39*, 11 1720.

[95] S. Sankaranarayanan, D. De Angelis, J. E. Rothman, T. A. Ryan, *Biophysical Journal* **2000**, *79*, 4 2199.

[96] J. S. Marvin, Y. Shimoda, V. Magloire, M. Leite, T. Kawashima, T. P. Jensen, I. Kolb, E. L. Knott, O. Novak, K. Podgorski, N. J. Leidenheimer, D. A. Rusakov, M. B. Ahrens, D. M. Kullmann, L. L. Looger, *Nature Methods* **2019**, *16*, 8 763.

[97] J. S. Marvin, B. Scholl, D. E. Wilson, K. Podgorski, A. Kazemipour, J. A. Müller, S. Schoch, F. J. U. Quiroz, N. Rebola, H. Bao, J. P. Little, A. N. Tkachuk, E. Cai, A. W. Hantman, S. S.-H. Wang, V. J. DePiero, B. G. Borghuis, E. R. Chapman, D. Dietrich, D. A. DiGregorio, D. Fitzpatrick, L. L. Looger, *Nature Methods* **2018**, *15*, 11 936.

[98] T. Patriarchi, J. R. Cho, K. Merten, A. Marley, G. J. Broussard, R. Liang, J. Williams, A. Nimmerjahn, M. von Zastrow, V. Gradinaru, L. Tian, *Nature Protocols* **2019**, *14*, 12 3471.

[99] F. Sun, J. Zeng, M. Jing, J. Zhou, J. Feng, S. F. Owen, Y. Luo, F. Li, H. Wang, T. Yamaguchi, Z. Yong, Y. Gao, W. Peng, L. Wang, S. Zhang, J. Du, D. Lin, M. Xu, A. C. Kreitzer, G. Cui, Y. Li, *Cell* **2019**, *174*, 2 481.

[100] N. G. Gubernator, H. Zhang, R. G. W. Staal, E. V. Mosharov, D. B. Pereira, M. Yue, V. Balsanek, P. A. Vadola, B. Mukherjee, R. H. Edwards, D. Sulzer, D. Sames, *Science* **2009**, *324*, 5933 1441.

[101] M. A. Gaffield, W. J. Betz, *Nature Protocols 1*, 6 2916.

[102] G. Hong, A. L. Antaris, H. Dai, *Nature Biomedical Engineering* **2017**, *1*, 1 0010.

[103] A. G. Beyene, A. A. Alizadehmojarad, G. Dorlhiac, N. Goh, A. M. Streets, P. Král, L. Vuković, M. P. Landry, *Nano Letters* **2018**, *18*, 11 6995.

[104] M. E. Matlashov, D. M. Shcherbakova, J. Alvelid, M. Baloban, F. Pennacchietti, A. A. Shemetov, I. Testa, V. V. Verkhusha, *Nature Communications* **2020**, *11*, 1 239.

[105] F. Wang, G. Dukovic, L. E. Brus, T. F. Heinz, *Science* **2005**, *308*, 5723 838.

[106] G. Bisker, J. Dong, H. D. Park, N. M. Iverson, J. Ahn, J. T. Nelson, M. P. Landry, S. Kruss, M. S. Strano, *Nature Communications* **2016**, *7*, 1 10241.

[107] S. Kruss, M. P. Landry, E. Vander Ende, B. M. Lima, N. F. Reuel, J. Zhang, J. Nelson, B. Mu, A. Hilmer, M. Strano, *Journal of the American Chemical Society* **2014**, *136*, 2 713.

[108] J. T. Coyle, *Biological Psychiatry* **1979**, *14*, 2 251.

[109] C. V. Borlongan, T. K. Koutouzis, P. R. Sanberg, *Neuroscience & Biobehavioral Reviews* **1997**, *21*, 3 289.

[110] P. R. Sanberg, S. F. Calderon, M. Giordano, J. M. Tew, A. B. Norman, *Experimental Neurology* **1989**, *105*, 1 45.

[111] L. Mangiarini, K. Sathasivam, M. Seller, B. Cozens, A. Harper, C. Hetherington, M. Lawton, Y. Trottier, H. Lehrach, S. W. Davies, G. P. Bates, *Cell* **1996**, *87*, 3 493.

[112] J. C. Jacobsen, S. Erdin, C. Chiang, C. Hanscom, R. R. Handley, D. D. Barker, A. Stortchevoi, I. Blumenthal, S. J. Reid, R. G. Snell, M. E. MacDonald, A. J. Morton, C. Ernst, J. F. Gusella, M. E. Talkowski, *Scientific Reports* **2017**, *7*, 1 41120.

[113] E. J. Slow, *Human Molecular Genetics* **2003**, *12*, 13 1555.

[114] L. B. Menalled, *NeuroRX* **2005**, *2*, 3 465.

[115] C.-H. Lin, *Human Molecular Genetics* **2001**, *10*, 2 137.

[116] M. A. Johnson, V. Rajan, C. E. Miller, R. M. Wightman, *Journal of Neurochemistry* **2006**, *97*, 3 737.

[117] M. A. Johnson, M. Villanueva, C. L. Haynes, A. T. Seipel, L. A. Buhler, R. M. Wightman, *Journal of Neurochemistry* **2007**, *103*, 5 2102.

[118] G. J. Yohrling, G. C.-T. Jiang, M. M. DeJohn, D. W. Miller, A. B. Young, K. E. Vrana, J.-H. J. Cha, *Molecular Brain Research* **2003**, *119*, 1 28.

[119] E. Etxeberria-Rekalde, S. Alzola-Aldamizetxebarria, S. Flunkert, I. Hable, M. Daurer, J. Neddens, B. Hutter-Paier, *Frontiers in Molecular Neuroscience* **2021**, *13* 617229.

[120] S. Elizarova, A. A. Chouaib, A. Shaib, B. Hill, F. Mann, N. Brose, S. Kruss, J. A. Daniel, *Proceedings of the National Academy of Sciences* **2022**, *119*, 22 e2202842119.

[121] C. Bulumulla, A. T. Krasley, B. Cristofori-Armstrong, W. C. Valinsky, D. Walpita, D. Ackerman, D. E. Clapham, A. G. Beyene, *eLife* **2022**, *11* e78773.

[122] A. G. Beyene, I. R. McFarlane, R. L. Pinals, M. P. Landry, *ACS Chemical Neuroscience* **2017**, *8*, 10 2275.

[123] V. Kung, R. Hassam, A. Morton, S. Jones, *Neuroscience* **2007**, *146*, 4 1571.

[124] E. T. Koch, C. L. Woodard, L. A. Raymond, *Journal of Neurophysiology* **2018**, *120*, 6 3077.

[125] T. Sudhof, *Annual Review of Neuroscience* **2004**, *27*, 1 509.

[126] J. del Castillo, B. Katz, *The Journal of Physiology* **1954**, *124*, 3 560.

[127] F. A. Dodge, R. Rahamimoff, *The Journal of Physiology* **1967**, *193*, 2 419.

[128] M. Yoshihara, J. Littleton, *Neuron* **2002**, *36*, 5 897.

[129] V. Leviel, V. Olivier, B. Guibert, *The Role of Calcium Ions in Dopamine Synthesis and Dopamine Release*, volume 41, Springer US, **1994**, series Title: Advances in Behavioral Biology.

[130] K. R. Brimblecombe, C. J. Gracie, N. J. Platt, S. J. Cragg, *The Journal of Physiology* **2015**, *593*, 4 929.

[131] Y. Cai, C. P. Ford, *Cell Reports* **2018**, *25*, 11 3148.

[132] J. Leitz, E. T. Kavalali, *Journal of Neuroscience* **2011**, *31*, 45 16318.

[133] C. Missale, S. R. Nash, S. W. Robinson, M. Jaber, M. G. Caron, *Physiological Reviews* **1998**, *78*, 1 189.

[134] K. A. Neve, editor, *The dopamine receptors*, The Receptors. Humana Press, 2nd ed edition, **2010**.

[135] J.-M. Beaulieu, R. R. Gainetdinov, *Pharmacological Reviews* **2011**, *63*, 1 182.

[136] B. Westerink, J. de Vries, *Neuroscience Letters* **1989**, *99*, 1 197.

[137] S. Sesack, C. Aoki, V. Pickel, *The Journal of Neuroscience* **1994**, *14*, 1 88.

[138] C. Ford, *Neuroscience* **2014**, *282* 13.

[139] M. Benoit-Marand, E. Borrelli, F. Gonon, *The Journal of Neuroscience* **2001**, *21*, 23 9134.

[140] Y. Schmitz, M. Benoit-Marand, F. Gonon, D. Sulzer, *Journal of Neurochemistry* **2003**, *87*, 2 273.

[141] M. Vashishtha, C. W. Ng, F. Yildirim, T. A. Gipson, I. H. Kratter, L. Bodai, W. Song, A. Lau, A. Labadorf, A. Vogel-Ciernia, J. Troncosco, C. A. Ross, G. P. Bates, D. Krainc, G. Sadri-Vakili, S. Finkbeiner, J. L. Marsh, D. E. Housman, E. Fraenkel, L. M. Thompson, *Proceedings of the National Academy of Sciences* **2013**, *110*, 32 E3027.

[142] M. Achour, S. Le Gras, C. Keime, F. Parmentier, F.-X. Lejeune, A.-L. Boutillier, C. Neri, I. Davidson, K. Merienne, *Human Molecular Genetics* **2015**, *24*, 12 3481.

[143] E. P. Bello, Y. Mateo, D. M. Gelman, D. Noaín, J. H. Shin, M. J. Low, V. A. Alvarez, D. M. Lovinger, M. Rubinstein, *Nature Neuroscience* **2011**, *14*, 8 1033.

[144] A. Anzalone, J. E. Lizardi-Ortiz, M. Ramos, C. De Mei, F. W. Hopf, C. Iaccarino, B. Halbout, J. Jacobsen, C. Kinoshita, M. Welter, M. G. Caron, A. Bonci, D. Sulzer, E. Borrelli, *Journal of Neuroscience* **2012**, *32*, 26 9023.

[145] F. K. Maina, T. A. Mathews, *ACS Chemical Neuroscience* **2010**, *1*, 6 450.

[146] S. O'Connor, R. Brown, *General Pharmacology: The Vascular System* **1982**, *13*, 3 185.

[147] E. G. Pitts, T. A. Stowe, B. A. Christensen, M. J. Ferris, *Neuropharmacology* **2020**, *175* 108163.

[148] T. Branco, K. Staras, *Nature Reviews Neuroscience* **2009**, *10*, 5 373.

[149] T. Branco, K. Staras, K. J. Darcy, Y. Goda, *Neuron* **2008**, *59*, 3 475.

[150] F. L. Urbina, S. M. Gomez, S. L. Gupton, *Journal of Cell Biology* **2018**, *217*, 3 1113.

[151] S. Fulton, D. Thibault, J. A. Mendez, N. Lahaie, E. Tirotta, E. Borrelli, M. Bouvier, B. L. Tempel, L.-E. Trudeau, *Journal of Biological Chemistry* **2011**, *286*, 11 9360.

[152] T. Patriarchi, A. Mohebi, J. Sun, A. Marley, R. Liang, C. Dong, K. Puhger, G. O. Mizuno, C. M. Davis, B. Wiltgen, M. von Zastrow, J. D. Berke, L. Tian, *Nature Methods* **2020**, *17*, 11 1147.

[153] S. Jeong, D. Yang, A. G. Beyene, J. T. Del Bonis-O'Donnell, A. M. M. Gest, N. Navarro, X. Sun, M. P. Landry, *Science Advances* **2019**, *5*, 12 eaay3771.

[154] K. D. Piatkevich, E. E. Jung, C. Straub, C. Linghu, D. Park, H.-J. Suk, D. R. Hochbaum, D. Goodwin, E. Pnevmatikakis, N. Pak, T. Kawashima, C.-T. Yang, J. L. Rhoades, O. Shemesh, S. Asano, Y.-G. Yoon, L. Freifeld, J. L. Saulnier, C. Riegler, F. Engert, T. Hughes, M. Drobizhev, B. Szabo, M. B. Ahrens, S. W. Flavell, B. L. Sabatini, E. S. Boyden, *Nature Chemical Biology* **2018**, *14*, 4 352.

[155] J.-F. Poulin, G. Caronia, C. Hofer, Q. Cui, B. Helm, C. Ramakrishnan, C. S. Chan, D. A. Dombeck, K. Deisseroth, R. Awatramani, *Nature Neuroscience* **2018**, *21*, 9 1260.

[156] O. J. Lieberman, A. F. McGuirt, E. V. Mosharov, I. Pigulevskiy, B. D. Hobson, S. Choi, M. D. Frier, E. Santini, A. Borgkvist, D. Sulzer, *Neuron* **2018**, *99*, 3 540.

[157] A. F. McGuirt, M. R. Post, I. Pigulevskiy, D. Sulzer, O. J. Lieberman, *The Journal of Neuroscience* **2021**, *41*, 16 3597.

[158] A. Yamamoto, J. J. Lucas, R. Hen, *Cell* **2000**, *101*, 1 57.

[159] N. Wang, M. Gray, X.-H. Lu, J. P. Cantle, S. M. Holley, E. Greiner, X. Gu, D. Shirasaki, C. Cepeda, Y. Li, H. Dong, M. S. Levine, X. W. Yang, *Nature Medicine* **2014**, *20*, 5 536.